ANALYTICAL MODELING OF CUTTING PROCESS MECHANICS AND DYNAMICS FOR SIMULATION OF INDUSTRIAL MACHINING OPERATIONS

by

EMRE ÖZLÜ

Submitted to the Graduate School of Engineering and Natural Sciences
in partial fulfillment of the requirements for the degree of
Doctor of Philosophy

Sabancı University

June 2008

ANALYTICAL MODELING OF CUTTING PROCESS MECHANICS AND DYNAMICS FOR SIMULATION OF INDUSTRIAL MACHINING OPERATIONS

APPROVED BY:

Assoc. Prof.Dr. Erhan Budak …….....
(Dissertation Supervisor)

Assoc. Prof.Dr. İsmail Lazoğlu …….....

Assoc. Prof.Dr. Bülent Çatay …….....

Assist. Prof.Dr. Mustafa Bakkal …….....

Assist. Prof.Dr. Güllü Kızıltaş …….....

DATE OF APPROVAL: ……..

ABSTRACT

Machining has been one of the most widely used manufacturing methods since the industrial revolution. Although the technological developments enabled machine tools to be stronger, work faster and produce more precise parts, the process parameters are still selected based on the experience. Selection of the acceptable or optimum parameters can only be possible by conducting extensive amount of experiments or by the help of the process models.

The main aim of this thesis is to develop analytical models in order to represent the true mechanical and dynamical behavior of metals during cutting operations. Analytical models for the orthogonal and oblique cutting processes are proposed. These models are used as a base in order to simulate commonly used industrial operations such as turning and 5 axis milling. Moreover, an initial approach is proposed in order to model cutting behavior when the cutting tool has a hone radius. The proposed models are step ahead from the previous ones as they represent the rake face contact and friction in a more accurate manner, and have the ability to calibrate the material model parameters and friction by few tests. The dynamic behavior during cutting is also a very important aspect. For this, a stability model which includes multi-dimensional nature of the cutting process is proposed. All the proposed models are verified by experiments and overall good agreement is observed. These models can be applied to industrial machining operations yielding shorter machining times, better surface quality, longer tool life, stable operations and less manufacturing costs.

Keywords: Machining, Cutting Process Modeling, Chatter Stability, Simulation of Machining Processes

ÖZET

Talaşlı imalat, sanayi devriminden bu yana en çok kullanılan imalat tekniklerinden biri olmuştur. Teknolojik gelişmeler, dayanımı daha yüksek, daha hızlı işleme yeteneğine sahip ve daha yüksek kaliteli parçaları imal edebilen takım tezgahlarının üretilmesini olanaklı kılarken, süreç parametrelerinin seçimi halen deneyimlere dayanarak yapılmaktadır. Kabul edilebilir ya da en iyi parametrelerin seçimi yalnızca çok sayıda deney yapılarak ya da süreç modelleri ile mümkündür.

Bu çalışmanın ana amacı, kesme işlemleri sırasında metallerin gerçek mekanik ve dinamik davranışlarını temsil eden analitik süreç modellerinin geliştirilmesidir. Dik ve eğik kesme süreçleri için analitik modeller sunulmuştur. Bu modeller, endüstride yaygın şekilde kullanılan tornalama ve 5-eksenli frezeleme operasyonlarının benzetiminde kullanılmıştır. Bununla birlikte, kesici takım ucu yarıçapının dikkate alındığı durumlar için bir ilk yaklaşım modeli önerilmiştir. Önerilen modellerde talaş yüzeyi teması ve sürtünme, literatürdeki diğer çalışmalardan daha doğru bir şekilde temsil edilmektedir. Ayrıca çok az sayıda testle sürtünme ve malzeme modeli katsayıları kalibre edilebilmektedir. Bütün bu özellikler, önerilen modelleri önceki çalışmalardan bir adım öteye taşımıştır. Metal kesme işlemlerindeki diğer önemli bir husus da kesme sırasındaki dinamik davranıştır. Bunun için, dinamik kesme sürecini çok boyutlu bir şekilde ele alan bir kararlılık modeli sunulmuştur. Tüm önerilen modeller deneylerle doğrulanmış ve karşılaştırmalar sonucu hesap edilen değerlerin deney sonuçlarıyla oldukça yakın olduğu görülmüştür. Önerilen modeller, operasyon sürelerinin kısaltılması, parça kalitesinin artması, takım ömrünün uzaması, kararlı işlemler ve böylelikle imalat maliyetinin azaltılması amacıyla endüstriyel operasyonlarına uygulanabilir durumdadırlar.

Anahtar Kelimeler: Talaşlı İmalat, Kesme Süreci Modellenmesi, Tırlama, Talaşlı İmalat Süreç Benzetimi

ACKNOWLEDGEMENTS

First and foremost, I would like to thank to my supervisor Dr. Erhan Budak. This thesis may have not been possible without his support, and his active participations. Not only our valuable technical discussions, but also the encouragements he provided me through my academic and social life help me to find the right way always easier.

I would also like to thank the members of my committee: Dr. İsmail Lazoğlu, Dr. Bülent Çatay, Dr. Mustafa Bakkal, and Dr. Güllü Kızıltaş.

My colleques Lütfi Taner Tunç, Erdem Öztürk, and Burak Aksu were always together with me from the beginning of my PhD study. I would like to thank Taner for the delicious coffees he made, for the "documentary" movies we took in Slovenia and Italy conferences, for the valuable technical and MATLAB discussions, and for his friendship throughout the thesis. I would like to thank to Erdem for the academic discussions, for the experimentation experiences that we discussed to find the best solutions, and for his support during the thesis. Burak on the other hand was very helpful for the verification tests that are presented in this study. Without his help and support for the experiments, the verifications in the thesis may not be finished on time.

One of the most active and important people for the studies in this thesis is Manufacturing Research Lab (MRL) technician Mr. Mehmet Guler. He was always available for helping the preparations of the verification experiments. His great and quick ideas always made me save the day. All his efforts for the last 4 years are appreciated and will always be remembered. Although Mr. Süleyman Tutkun involved in the MRL team last year, his supports on the experiments are also appreciated.

We had successfully created a great office atmosphere in our FENS 1021 lab that brings a great working environment for which I like to present here my appreciation. Special thanks go to the grads, Lale Tunçyürek, Esra Dervişoğlu, Nihan Özşamlı, Tevfik Altınalev, Ahmet Şen, Ayfer Başar, Elvin Çoban, Mahir Umman Yıldırım, Nurşen Aydın, Gamze Belen, İbrahim Muter, Duygu Taş, Tamer Doyuran, Figen Öztoprak, Serkan Çiftlikli, Kerem Osman Akgün, Umut Kirmit, İlter İrdesel and the former Msc graduates.

The former PhD graduates Dr. İstem Özen and Dr. Ahu Gümrah Dumanlı were the two important people that support this thesis in technical and social terms. Dr. Özen was a great friend and supporter who was always there for technical, entertaining, and

educational discussions and chats. Despite of her visits, her absence at the office for the last year was always the missing piece. Dr. Dumanlı was also a great friend. Her great personality and friendship always made me feel that I am not alone when I have a problem. I appreciate her due to her numerous technical helps and great and funny breaks and lunch we had together.

Anna Vanya Uluç and Seren Yüksel were the two people who were there for the last minute aids for this thesis. Although we didn't spend too much time together, their great last minute helps made this thesis ready on time. Special thanks go to Vanya for proofing the "minimum energy principle" once again, which is then related to the "radius of the universe" after several discussions between us, and for her active participations in writing the thesis, at my defense, and presentation preparations. Her great helps and sacrifices will always be remembered and appreciated.

My best friends in this life Onur Ozturk, Vedat Bağışgil and her wife Ayşe Seda Bağışgil, Dr. Tayfun Akoğlu, and Kayhan Dizdaroğlu deserve many great thanks. Without their moral supports and encouragements my social life during this thesis study would have never been that great. I also would like to thank to İpek and Osman Sinan Güven as they have been sister and a brother to me. I appreciate their moral support, invaluable discussions, and encouragements and the great times and meetings we spent together.

Çağla Demirbaş is the one who was with me from the beginning of my academic life. She was the one who helped me to decide in the right choices in my life, and the one who was "once" very much adored. Her existence in my life did not only enlighten my perspective but also encouraged me completing this thesis by giving my best.

At last but not the least, I would like to thank to my family for their great guidance, supports and patience during this study. My father İlhan Özlü's great perspective and invaluable discussions we made throughout my life is one of the factors that made me to decide to continue my education life. My mother Ayşe Özlü on the other hand is one of the most important motivations in completing my studies. Her sacrifices, supports, and delicious foods helped me to survive in my hardest times. Finally, my special thanks go to my grandmother Fehime Özlü; without her prays, motivations, her great life perspective, and lectures, this thesis may have not been possible.

TABLE OF CONTENTS

LIST OF FIGURES

LIST OF TABLES

1. INTRODUCTION

1.1. Introduction and Literature Survey

Shaping raw materials in order to give them functionality, namely manufacturing has always been in the interest of human beings. Manufacturing comes from the combination of two Latin words “manus” meaning “hand” and “factus” meaning “to make”. Although in the very beginning human beings used to manufacture goods by hand, due to the related technological developments, they began to take their “hands off” and used tools instead. There are several ways invented in order to manufacture goods, such as casting, forming, machining, welding etc.

Machining is one of the most important manufacturing techniques. Basically, the desired geometry is generated by removing the unwanted material by a cutting tool from the workpiece material which has a lower hardness. Although machining operations can be used to give the final shape of the product, they can also be used to give the desired tolerances for the semi-final products that are manufactured by using other methods. This property of machining makes it more common among other manufacturing techniques. The machining is commonly used in the industrial areas such as aerospace, defense, die and mold making, automotive, energy, electronics, medical products, micro systems etc.

Machining can be used to manufacture several material types including metals, cast irons, polymers, ceramics, composite materials, woods, rocks etc. Among others, metal cutting is one of the oldest and most common applications of machining which is also the focus of this thesis. Moreover, there are several methods of metal cutting such as turning, milling, broaching, boring, drilling etc. These types of metal cutting operations usually have their own machining tool types such as lathe, milling machine, broaching machine, drill etc. In the conventional manner, these machine tools are used manually and the skills of the technician usually become important in manufacturing

repeatable and high quality products. However, the technological developments in the field of control enabled the use of Computer Numerically Controlled (CNC) machine tools which provide shorter cutting times, higher repeatability, high quality products, and low manufacturing costs. Despite of the technological developments, the dependency on the "experience" based manufacturing instead of "research" based, has usually been the choice of the manufacturers. That is, the selection of cutting parameters usually done by the previous experiences or taken from the tool manufacturer catalogs. This situation can be related to the lack of commonly accepted developed scientific methods, as well as the unrealistic assumptions that cause inaccurate and imprecise predictions from the developed models. Therefore, the true modeling of metal cutting processes is very important since it enables the prediction of optimum process parameters as well as the identification of the problem areas before the operation takes place.

The true representation of the cutting process must involve the modeling of three deformation zones which are responsible for the cutting, Figure 1.1. The primary shear zone is the region which is responsible for the chip formation due to the plastic deformation of the workpiece. The secondary shear zone, known also as the rake contact, on the other hand, is responsible for the chip-tool contact where the complex friction conditions exist. The third deformation zone is responsible for the deformation of the workpiece which doesn't contribute to the chip formation.

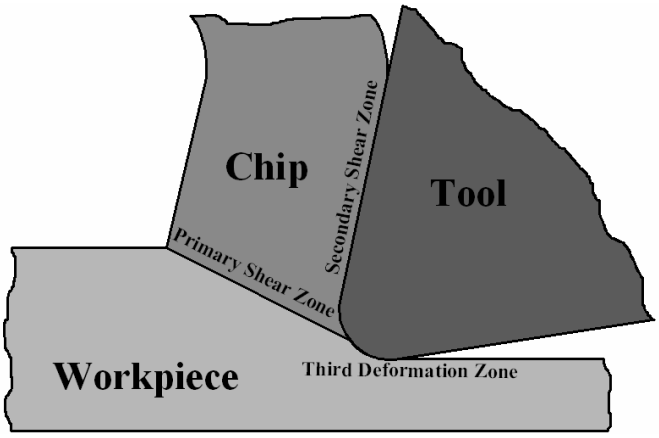

Figure 1.1: The three deformation zones in orthogonal cutting.

The basic aim of this thesis is to develop analytical models that can truly represent the mechanical and dynamical behavior of the metal cutting processes. The developed models are applied to the simulation of the commonly used industrial operations such as turning, boring, and 5 axis milling operations. The developed models are verified by

using experiments on real machine tools. As side observations, by the verified analytical models, the effect of several important parameters on the cutting behavior is also investigated. The developed models can be applied to industrial applications and used for selection of the optimum parameters during manufacturing which brings in shorter machining times, better surface qualities, longer tool lives, more stable operations and thus less manufacturing costs.

Being the fundamental model for all cutting processes, modeling of the orthogonal cutting (see Figure 1.2.a) has been one of the most important problems for machining researchers for decades. Understanding the true mechanics and dynamics of the orthogonal cutting process would result in solution of major problems in machining such as parameter selection, accurate predictions of forces, stresses, and temperature distributions. One of the first successful mathematical attempts for modeling of the mechanics of orthogonal cutting was made by Merchant [1]. Merchant [1] studied the formation of continuous chip by assuming that the chip is formed by shearing along a shear plane whose inclination was obtained from the minimum energy principle. Although his model has several important assumptions, it is still widely used to understand the basics of the cutting process. Later, many models were proposed [2-7] on the modeling of the orthogonal cutting process. After some deceleration in the research on cutting process mechanics due to the developments in CNC and CAD/CAM technologies, the process research regained some momentum in recent years. Many predictive models have been proposed by means of analytical, semi-analytical or completely numerical methods up to now. Semi-analytical models, where some of the parameters are identified from the cutting tests, usually yield high prediction accuracy, however they may not always provide insight about the process [8-10]. In addition, the cutting tests can be time consuming depending on the number of variables and their ranges. Numerical methods such as FEM [11-14] could provide much more detailed information about the process, such as temperature and pressure distribution, however they can be very time consuming. On the other hand, some analytical models may provide sufficient insight about the process. They can be categorized as the slip-line models [15-19], and thin and thick shear zone models [20-24].

It can be deduced from the previous studies that there are several accurate models for the primary shear zone. There are also several studies where the friction in machining is investigated [25-31] which is critical for the secondary shear zone.

However, there are still issues in including a relevant rake contact model in a global thermomechanical approach of cutting processes.

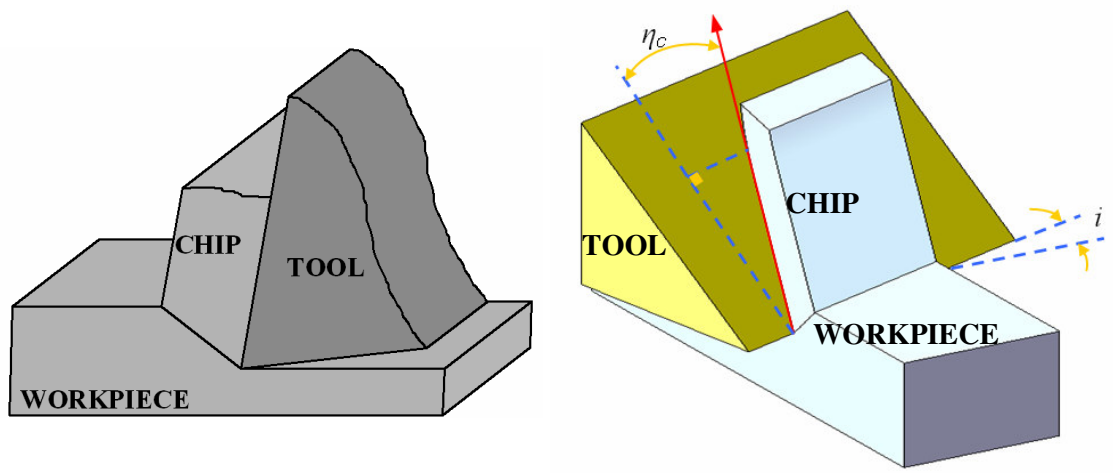

(a) (b)

Figure 1.2: The 3D representation of the (a) orthogonal, and (b) oblique cutting processes.

Although modeling of the orthogonal cutting serves as the base, oblique cutting (see Figure 1.2.b) which involves the chip formation in 3D due to the inclination angle *i*, serves as a more realistic approach in order to simulate common industrial operations. Moreover, once the orthogonal cutting model is developed it can then be applied to the oblique cutting process by several geometrical and kinematical transformations. One of the accurate ways of modeling oblique cutting process is proposed by applying the mechanics of cutting using oblique transformations from the orthogonal data [9, 10, 32]. The orthogonal data is obtained by a large number of orthogonal tube cutting tests and applying the mechanistic model approach. Again, although the predictions of the model are quite precise, there is a lack of information about the insights of the cutting process. In one of the later studies in analytical modeling of oblique cutting, Becze et al. [33] proposed a force prediction model based on the chip morphology of local shearing. Although the model was analytical and good agreement is observed with the experimental results, it lacked providing insight about the process and the friction behavior on the rake face. In a recent study, Moufki et.al [34] proposed an analytical approach for modeling the oblique cutting process with a thin shear band approach. In this model, the friction is modeled as a function of the temperature. However, again the friction behavior on the rake face is assumed to be only sliding which may be a realistic

approach at very high cutting speeds, but an unrealistic assumption even for the moderate cutting speeds.

The foregoing review considered the models where the tool has a sharp cutting tip. However, in practical applications the cutting tools have a hone radius which brings in the third deformation zone. There are several methods proposed in order to model this region. The mechanistic approach [9] identifies edge cutting forces by conducting cutting experiments for different feed rates and then extracting the forces responsible for the chip formation. This approach is a precise one although it helps predicting the cutting forces only. The numerical methods such as the FEM [35, 36], are also used to model the third deformation zone. However, the need for the elasto-plastic material models make the solution times even higher than the cases without considering the hone radius. The results obtained by this approach usually fail to predict the edge cutting forces correctly. Several analytical models using slip-line field analysis have also been proposed [37-41].

The modeling of oblique cutting process enables the simulation of the most common cutting processes such as turning and milling operations. This is because, in most of the practical applications, due to the complex geometries of the cutting tools, the chip formation cannot be represented on a 2D plane but a 3D space.

In turning, the existence of the nose radius makes representation of the cutting behavior more complicated. The existence of the nose changes the geometry of the uncut chip thickness, and affects the direction of the forces, chip flow as well as the local cutting angles. In order to take the effect of the nose radius into account a simple model is proposed by Colwell [42] in an earlier study. In this study, the cutting edge is modeled by a simple line which is referred to as the “Colwell line” and the chip flow angle is assumed to be perpendicular to this line. Later, amore complicated model is proposed [10] where the nose radius is divided into elements, and the mechanistic model is applied in order to calculate the cutting forces. In a more recent study Molinari et al. [43] proposes a novel approach and again used a divided chip thickness. In this study, the interactions between the elements are taken into account by an analytical approach and the chip flow angle is calculated accordingly. However the numerical solution proposed for the model involves several iteration steps and the model is not using the best representation for calculating the shear angle for each element. The common problem in modeling the turning operations is to relate the chip flow, shear flow, and shear angles together with the friction behavior at the rake face.

5-axis milling operations, on the other hand, are used extensively in the manufacturing of free form surfaces such as turbine engine components, dies and molds. The complication in 5-axis milling processes is due to the additional two angles, i.e. lead and tilt angles. Moreover, due to the ball end geometry, the conditions such as the cutting speed vary continuously along the cutting edge. There have been numerous efforts for modeling of the ball-end milling processes. These can be grouped into three categories according to how material data is obtained, varying from completely analytical [44, 45] to completely experimental [46-48]. Budak et al. [9] presented a hybrid method named as mechanics of milling for milling force modeling based on the orthogonal cutting data and the oblique cutting model. The mechanics of milling approach was employed by several authors in 3-axis ball-end milling [49-54].

There are two important inputs for modeling of the cutting process: the constitutive relationship and the friction coefficient between the tool and the workpiece material. These two inputs can be considered to be independent of the cutting mechanics as they are related to the mechanical and physical properties of the materials. Identification of both properties is very critical for accurate modeling of the machining processes.

Being a common topic in mechanics, friction has also been extensively studied in basic sciences. However, machining researchers have also paid special attention to friction due to its importance in cutting processes. The early studies on the subject concluded that there is a direct relationship between the shear angle and the friction. Using minimum energy principle for the continuous type chips, Merchant [1] concluded a similar relationship between the shear angle and the rake face friction. In a later study, Lee and Shaffer [4] obtained a similar relationship by applying slip-line field theory to the orthogonal cutting. The solutions presented in these studies have assumptions which do not accurately represent the friction behaviour of the process. Based on the experimental observations, however, it has been well accepted that the overall friction coefficient on the rake face decreases with the increasing rake angle. On the other hand, the effects of other parameters such as cutting speed or feed rate were not known that well. Eventually, Zorev [3] approached the problem by observing the normal pressure and shear stress distributions on the rake face, and proposed distribution forms for them. Basically, Zorev [3] proposed that the material exiting the primary shear zone reaches the rake face with such a high normal pressure that there is a sticking contact zone close to the tool tip. Due to the drop in the normal pressure, the contact state changes to the

sliding (Coulomb) friction away from the tool tip on the rake face. This behaviour is also verified by numerous researches in later studies [29, 55, 56] mostly by split-tool experiments measuring the normal pressure and shear stress distributions on the rake face.

Friction between two contacting bodies has several dependencies such as the material pair, temperature, pressure and speed depending on the application ranges [23, 27]. For instance, in a recent study, Phippon et al. [26] conducted several experiments in an original test setup in order to investigate the sliding friction behavior at high sliding velocities, and concluded that the sliding coefficient of friction strongly depends on the speed and the pressure. In a different study, Moufki et al. [34] proposed an orthogonal cutting model which relates the sliding friction coefficient to the mean temperature on the rake face. As another approach, the semi-analytical method known as the mechanics of cutting [9, 10] relates the apparent friction coefficient to the rake angle, feed rate and the cutting speed, and uses them in force prediction. However, this approach may take longer tests times since high number of tests must be carried out depending on the ranges. Similarly mechanistic models do not provide much insight about the friction behavior of the workpiece and tool couples.

The material behaviour on the other hand is another important issue during metal cutting. It is well known that the strain rates can go up to 10^6 1/s at high, and 10^5 1/s at moderate cutting speeds. There are several constitutive relationships in order to model the material behavior under high strain loading conditions. Three most widely used relations that account for the strain rate effects are the Johnson-Cook, the Zerilli-Armstrong, and the mechanical threshold stress (MTS) constitutive relations [57-59]. The Johnson-Cook (JC) constitutive relation is relatively simple, one dimensional model that accounts for the effects of strain, strain rate, and thermal softening on flow stress and utilize a von Mises yield criterion. It describes the material hardening behavior based on the well known power-law function. Also it is an empirical relation that is relatively simple to calibrate for a given material. That is, very few stress-strain curves covering the loading conditions are required to determine the parameters. It is relatively easy to implement into computer codes, inexpensive to use and produces reasonably accurate predictions for a range of materials if loading conditions do not exceed those used to determine the material parameters. It is presented in the literature for medium and high strain rates of deformation that Johnson-Cook Model exhibits good correlation between experimental studies, especially with split Hopkinson

Pressure bar [60-63]. Moreover several materials JC parameters can be found in the literature relatively more easily.

The foregoing reviewed studies were only considering the mechanics of the cutting processes. However, the dynamic behavior during cutting is another important issue. Due to the process dynamics the cutting conditions may become unstable. Stability in cutting is an important problem due to resulting high cutting forces, poor surface quality and reduced productivity. Although chatter is a more common problem in milling, it can be a limiting factor in some turning and boring operations where slender and flexible tools and parts are involved. The analytical prediction of stability limits for orthogonal cutting is well established, however only a few attempts have been made for modeling and analysis of turning stability considering the true geometry of the process. This study focuses on the analytical treatment of the process dynamics, and stability predictions in turning operations.

The mechanics of instability in cutting processes was first understood by Tlusty [64] and Tobias [65]. They observed that the modulated chip thickness due to vibrations affects cutting forces dynamically, which in return increases vibration amplitudes yielding a process known as regenerative chatter. They also observed that the depth of cut was the key process parameter in the cutting process stability. Tlusty [64] analytically showed that for the depth of cuts higher than the stability limit, the magnitude of the dynamic forces and oscillations increases yielding instability, thus chatter vibrations. In his orthogonal stability model, Tlusty [64] used an approximate solution resolving cutting forces and structural dynamics into one direction, i.e. the chip thickness direction, reducing the dynamics problem into a 1-dimensional (1D) case. Although this is a valid model for a truly 1D operation such as plunge turning or straight turning without inclination angle and nose radius, it is not an accurate model for many cases where a multi dimensional cutting process and/or dynamics are involved. This is similar to the case of vibration analysis of 2 degree-of-freedom (DOF) system. Lumping or resolving the system parameters in one DOF only would result in a 1D system, and one natural mode which is different from any one of the two actual natural frequencies. Similarly, in dynamic cutting process analysis reducing a 2D or multi-D cutting system, which can only be accurately represented as an eigenvalue problem, into a single algebraic equation would result in inaccurate stability predictions. This has been demonstrated in the analysis of milling stability by Minis and Yanushevsky [66] and Budak and Altintas [67]. In an early study, Marui et al. [68, 69] investigate the

chatter stability in turning operations experimentally where limited theoretical treatment is presented. They concluded that primary chatter vibration is due to the self excited vibrations, and the energy supplied for the vibrations is due to the frictional force on the flank contact, but they failed to model the dynamic mechanism analytically. Later, Kaneko et al. [70] modeled the self excited chatter and chatter marks left on the surface in turning operations. They used a 2D model for chatter mark predictions and the solution is done numerically. However, the conclusions are mostly based on experimental results rather than the modeling. In contrast, Minis et al. [71] used an oriented approach and failed to integrate the 3D turning geometry into the model. Later, Rao et al. [72] used the multi directional approach used by Budak and Altintas [73] to model the stability in turning, and calculated the dynamic chip area with a cross coupling term including the effect of vibrations in one direction on the chip area in the other direction. Clancy et al. [74] added wear and process damping to their model. However, in these studies cross coupling term made the modeling and the solution complicated. Atabey et al. [75] and Lazoglu et al. [76] proposed an analytical model for force prediction in boring, and, using time domain solutions, they predicted workpiece topography as well. Ozdoganlar and Endres [77] presented an analytical chip-area calculation for inserts having a nose radius, which was also used in the 1D stability modeling of turning [78]. They [79] also modeled the stability in a multi dimensional cutting system analytically. Reddy et al. [80] applied the proposed model in [78] to the turning of a wheel-rim and obtained stability maps. In a recent study Chandiramani et al. [81] employed a multi-dimensional approach to model the turning dynamic system the turning geometry was over simplified. The studies summarized above (except [70, 78, 79]) solved the stability equations in the time domain using numerical methods.

1.2. Objective

As discussed earlier, the modeling of cutting operations is needed in the selection of optimum cutting parameters for the industrial applications, and in the investigation of the cutting process for the scientists. As reviewed in the previous section, several process modeling methods are developed. For instance the most widely used one, the mechanistic model, predicts the cutting forces very precisely but fail to provide insight about the cutting process e.g. material flow behavior, friction, and the number of tests needed to obtain the required data can be very high. Numerical methods such as FEM, on the other hand, gives insight about the process, but the solution times are so long that

it may be a better choice to conduct the experiments in many of the cases. There are still problems with the prediction accuracy of FEM methods. Finally, the analytical models such as slip-line field analysis are reasonably flexible in terms of modeling of the cutting region, and thus there are numerous slip-line field analyses proposed in the literature. For this reason, there is no well accepted slip-line field method for modeling the cutting operations. It is obvious that there is a need for process models which are fast, and accurate, and represents the cutting behavior in a more precise way. Consequently, our aim is to propose analytical process models which represent the true material behavior and friction. By the help of these models, we can simulate the industrial operations and investigate the cutting behavior further. As a base approach we begin with the modeling of the orthogonal cutting processes.

In modeling of the orthogonal cutting process, we use the two-zone contact model of Zorev [3] which considers sticking and sliding friction regions on the rake face. Including this contact model into a thermomechanical modeling of orthogonal cutting is the scope of the present study. This constitutes an important improvement of previous approaches which were either assuming complete sticking (Oxley's model [15]) or only sliding Molinari and Dudzinski [21]. Sliding may be realized along most of the contact zone for high cutting speeds. However, for low cutting speeds, sticking cannot be neglected.

The two-zone contact model is combined with the modeling of the primary shear zone proposed by Molinari and Dudzinski [21] and Dudzinski and Molinari [22]. Any thermo-mechanical constitutive relationship for the workpiece material can be used but in this study the Johnson-Cook law is considered due to the advantages discussed above. The primary shear zone is taken as a thin layer with constant thickness. In general, the material exiting from the primary shear zone enters the rake contact with a high normal pressure that creates sticking, i.e. plastic contact, between the tool and the material. After some distance, the contact state changes to sliding, i.e. elastic contact, due to the decreasing normal pressure. The minimum energy approach is used for the shear angle prediction. The workpiece material parameters and sliding friction coefficient at the tool rake face are calibrated directly from orthogonal tube cutting tests. After calibration, the model can be used for different machining operations using the same tool and workpiece material. The outputs of the proposed model are the shear angle, shear stress in the shear plane, cutting forces, the stress distributions on the rake

face, the length of the sticking and sliding zones and the global (or apparent) friction coefficient. The model predictions are shown to be well correlated to experimental data

Accurate representation of contact behavior on the rake face is critical for the through understanding and modeling of the metal cutting operations. In this regard, quantitative analysis of the friction behavior in metal cutting is important for better understanding of the nature of the process. The identification of the sliding friction coefficient between the workpiece-tool couple, and the relation of the sliding friction coefficient to the apparent one are critical for process modeling. The contact lengths which are basically the physical representation of the friction behavior on the rake face, must also be modeled and analyzed. Based on these, another objective of this study is to further investigate the friction behavior in metal cutting operations.

Also an initial approach is proposed for modeling the edge cutting forces in orthogonal cutting operations. The proposed model involves the true representation of the hone radius and its effects on both the chip formation and ploughing.

For the simulation of the two most common processes, i.e. turning and milling the proposed oblique cutting model is applied. Since the material flow behavior and the friction conditions on the rake face are considered realistically, the proposed models are precise in terms of cutting forces, as well as gives more insight about those processes, such as the pressure distribution, contact lengths, etc.

In terms of process dynamics, currently, the most common stability analysis in turning applications is done with an oriented-transfer function stability model which is based on the analytical model proposed by Tlusty [64]. The oriented transfer function model cannot include the effect of the multi-dimensional dynamics, the oblique cutting conditions, and the insert nose radius. The model proposed in this study is an analytical model for the prediction of stability limit for multi-dimensional dynamic turning systems. This model is then merged with an insert nose radius model in order to extend it to the stability limit predictions for turning and boring operations with real cutting inserts. The stability model includes all important parameters of the process geometry, i.e. cutting angles and tool nose radius, in addition to the tool and workpiece dynamics. The model proposed is a step ahead of the previous studies as it includes the dynamics of cutter and workpiece in a multi directional form (not oriented in one direction), an accurate but practical modeling of tool nose radius and dynamic chip thickness, and a stability limit solution in the frequency domain rather than time domain simulations.

1.3. Layout of the Thesis

The thesis is organized as follows:

In Chapter 2 the proposed models for the simulation of orthogonal and oblique cutting are presented. The detailed formulation regarding the derivation of the equations is shown. The solution procedures are also provided.

In Chapter 3, the verifications for the proposed orthogonal and oblique cutting processes are presented in terms of cutting forces, shear angle, and contact length predictions with several material-tool couples. Also the friction behavior in metal cutting is investigated as well as the effect of the material model parameters on the cutting force predictions.

In Chapter 4, an initial new model for the prediction of the edge forces in orthogonal cutting operations is presented. The proposed model is compared with the experimental results.

In Chapter 5, the process simulation models for the most two common industrial operations are presented, turning and 5 axis milling operations. The proposed model is verified by the cutting experiments in terms of cutting force predictions.

In Chapter 6, a stability model of the turning and boring processes including the multi-dimensional effects are proposed. The detailed formulation is also presented along with some simulation results.

In Chapter 7, the proposed stability model in Chapter 6 is verified by several chatter tests for turning and boring operations. Also the comparison between the widely used one dimensional oriented transfer function stability model and proposed multi-dimensional stability model is presented.

In Chapter 8, the suggestions for the further research are presented.

In Chapter 9, the contributions of the thesis to the literature and discussions are provided.

2. MODELING OF CUTTING PROCESS BY A THERMOMECHANICAL MATERIAL MODEL

The modeling of cutting processes is one of the basic aims of this thesis. The true representation of the chip formation must involve the true modeling of the material flow during cutting. Basically, due to the plastic deformation and the contact between the chip and the tool there exists a rise in the temperature which totally affects the material behavior. The modeling of this type of deformation behavior can only be done by using a thermomechanical type of constitutive relationship. Also, due to the initially very high but decreasing normal pressure distribution on the chip-tool contact, sticking (plastic) and sliding (elastic) friction regions exist. This behavior is also modeled by using a dual-zone approach.

In this chapter the mathematical formulation of the proposed model for orthogonal cutting operations are presented in detail. Then, the application of the proposed model to the oblique cutting operations is demonstrated.

2.1. Modeling of Orthogonal Cutting

In this chapter, the orthogonal cutting model is presented. Firstly, the basic formulations regarding the primary shear zone and the two-zone contact model are given. Then, the working of the model is presented.

In general, the material exiting from the primary shear zone enters the rake contact with a high normal pressure that creates sticking, i.e. plastic contact, between the tool and the material. After some distance, the contact state changes to sliding, i.e. elastic contact, due to the decreasing normal pressure. The minimum energy approach is used for the shear angle prediction. The workpiece material parameters and sliding friction coefficient at the tool rake face are calibrated directly from orthogonal tube cutting tests. After calibration, the model can be used for different machining operations

using the same tool and workpiece material. The outputs of the proposed model are the shear angle, shear stress in the shear plane, cutting forces, the stress distributions on the rake face, the length of the sticking and sliding zones and the global (or apparent) friction coefficient.

2.1.1. Modeling of the Primary Shear Zone

The primary shear zone model is taken from Molinari and Dudzinski [21] and Dudzinski and Molinari [22], but additionally the contact at the rake face is modeled by the two-zone approach of Zorev [3]. As the details of the primary shear zone model can be found in [21-23], just a brief presentation is given here. The main assumption is that the primary shear zone has a constant thickness h, and that no plastic deformation occurs before and after the primary shear zone up to the sticking region on the rake face. The material behavior is represented with the Johnson-Cook constitutive model in this study due to the reasons discussed in Chapter 1, in the form:

$$\tau = \frac{1}{\sqrt{3}}\left[A + B\left(\frac{\gamma}{\sqrt{3}}\right)^{n}\right]\left[1 + \ln\left(\frac{\dot{\gamma}}{\dot{\gamma}_0}\right)^{m}\right]\left[1 - \left(\overline{T}\right)^{v}\right] \qquad (2.1)$$

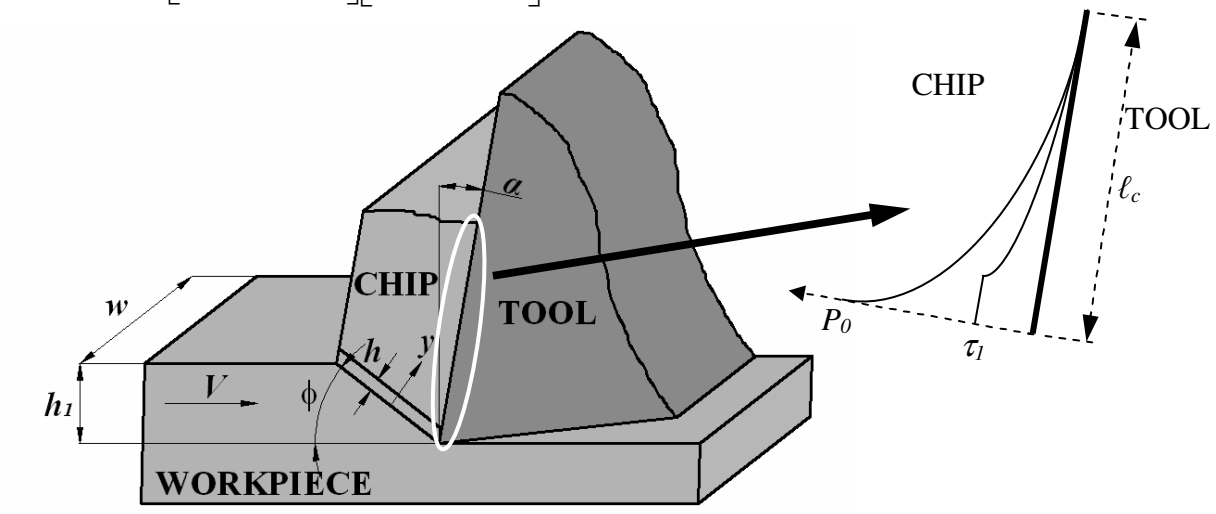

Figure 2.1: The schematic representation of the orthogonal cutting process.

where γ is the shear strain, $\dot{\gamma}$ is the shear strain rate, $\dot{\gamma}_0$ is the reference shear strain rate, A, B, n, m, and v are material constants. The reduced temperature is defined by $\overline{T} = (T-T_r)/(T_m-T_r)$, where T is the absolute temperature, T_r is the reference temperature, and T_m is the melting temperature. The material entering the primary shear zone sustains a shear stress of τ_0. The shear stress at the exit of the shear plane, τ_1, is different from τ_0

when inertia effects are important. Assuming a uniform pressure distribution along the shear plane (exit of the primary shear zone), τ_0 can be iteratively calculated as proposed in [23]. From the conversation of momentum we obtain [23]:

$$\tau_1 = \rho(V \sin\phi)^2 \gamma_1 + \tau_0 \tag{2.2}$$

where ρ is the density of the workpiece material γ_1 is the plastic shear strain at the exit of the primary shear zone, V is the cutting speed and ϕ is the shear angle (see Figure 2.1Figure 2.1: The schematic representation of the orthogonal cutting process.). Also from the conservation of energy (assuming adiabatic conditions) we obtain the following relation [23]:

$$T = T_w + \frac{\beta}{\rho c}\left(\rho V^2 \sin^2\phi \frac{\gamma^2}{2} + \tau_0 \gamma\right) \tag{2.3}$$

where c and β is the heat capacity and the fraction of the work converted into heat, and T_w is the absolute temperature of the workpiece. For the metals, it is empirically seen from the previous studies that β can be taken as 0.9. Moreover there is a compatibility condition [23]:

$$\frac{d\gamma}{dy} = \frac{d\gamma}{dt}\frac{dt}{dy} = \frac{d\gamma/dt}{dt/dy} = \frac{\dot{\gamma}}{V\sin\phi} \tag{2.4}$$

The boundary conditions are:

$$T = T_w \quad \text{at} \quad y = 0 \tag{2.5}$$

$$\gamma = 0 \quad \text{at} \quad y = 0 \tag{2.6}$$

$$\gamma = \gamma_1 = \tan(\phi - \alpha) + \frac{1}{\tan\phi} \quad \text{at} \quad y = h \tag{2.7}$$

The shear stress τ_0 at the entry of the shear band can be calculated iteratively by solving the differential equation (2.4) with the boundary conditions above. When τ_0 is calculated the shear stress τ_1 at the exit of the shear band can be calculated by the equation (2.2), which is then used in the rake face contact analysis.

2.1.2. Two-Zone Contact Model and Orthogonal Cutting Approach

In this section, the dual zone contact model of Zorev [3] is formulated and introduced into the global modeling of orthogonal cutting. In this model the rake face contact is divided in two regions. In the first region, the contact condition is assumed to be sticking due to the high normal pressure exerted on the tool, whereas in the second region the contact is considered to be sliding and is governed by the Coulomb friction

law. Zorev [3] and some other later studies [82-84] describe the shear stress and the normal stress distributions on the rake face as shown in Figure 2.2.a However, it is well known, and also proved by friction tests [85], that the Coulomb friction coefficient cannot exceed 1.0 between metallic materials unless some kind of oxide formation or chemical reaction occurs [27, 29, 86]. Therefore, as shown by split tool cutting tests [18, 29, 55, 56, 85, 87] the distribution of the shear and normal stress on the rake face are obtained as shown in Figure 2.2.

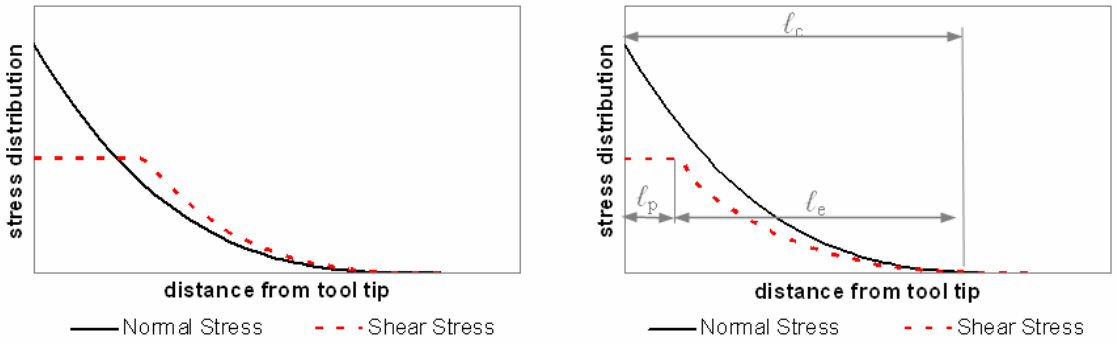

Figure 2.2: Stress distributions on the rake face according to the Zorev's [3] model, with sliding friction coefficient (a) larger than 1, and (b) smaller than 1.

It is assumed that the normal stress P decreases with the distance from the tool tip, (Figure 2.2Figure 2.2: Stress distributions on the rake face according to the Zorev's [3] model, with sliding friction coefficient (a) larger than 1, and (b) smaller than 1.). According to the Coulomb friction law, the sliding shear stress τ is proportional to the normal stress represented by $\tau = \mu\sigma$, where μ is the friction coefficient (dashed line in Figure 2.2). The shear stress is increases towards the tool tip. However, according to the plastic flow criterion (assumed here that it is not dependent on the pressure P) the shear stress cannot exceed the flow stress τ_1 of the work-material on the rake face. In a first approximation, τ_1 will be taken equal to the shear stress at the exit of the primary shear zone. This stress is calculated with equation (2.2), and finally the shear stress distribution on the rake face can be defined as follows:

$$\begin{aligned} \tau &= \tau_1 && x \le \ell_p \\ \tau &= \mu P && \ell_p \le x \le \ell_c \end{aligned} \qquad (2.8)$$

where ℓ_c is the contact length, and x is the distance on the rake face from the tool tip. Also, for the normal stress on the rake face the following distribution is selected, which is validated by various researchers and experiments for the metallic materials [23, 29, 55]:

$$P(x) = P_0\left(1-\frac{x}{\ell_c}\right)^{\zeta} \tag{2.9}$$

where P_0 is the normal stress on the rake face at the tool tip, and ζ is the distribution exponent. From the application of the coulomb friction law along the sliding zone we have:

$$\tau(x) = \mu P_0\left(1-\frac{x}{\ell_c}\right)^{\zeta} \tag{2.10}$$

At the end of the sticking zone (beginning of the sliding zone) the tangential stress τ is equal to the shear yield stress τ_1 :

$$\tau_1 = \mu P_0\left(1-\frac{\ell_p}{\ell_c}\right)^{\zeta} \tag{2.11}$$

From equation (2.11), the length of the sticking zone can be obtained as follows:

$$\ell_p = \ell_c\left(-\left(\frac{\tau_1}{P_0\mu}\right)^{1/\zeta}+1\right) \tag{2.12}$$

For a given μ , there are three unknowns P_0, ℓ_p, and ℓ_c in equation (2.12). P_0 can be related to the normal force acting on the rake face by considering the pressure distribution along the contact length ℓ_c (see Figure 2):

$$N = \int_0^{\ell_c} P(x)dx = \int_0^{\ell_c} P_0\left(1-\frac{x}{\ell_c}\right)^{\zeta} w dx = P_0\frac{w\ell_c}{\zeta+1} \tag{2.13}$$

where w is the width of cut. The normal force N can also be calculated in terms of the shear force on the shear plane is:

$$N = F_s\frac{\cos\lambda_a}{\cos(\phi+\lambda_a-\alpha)} \tag{2.14}$$

where λ_a is the friction angle defined by $\lambda_a = \tan^{-1}\mu_a$. The apparent (global) friction coefficient μ_a is defined later, see (2.23). Also the shear force F_s in equation

(2.14) is obtained by assuming that the shear stress distribution on the shear plane AB at the exit of the primary shear zone (Figure 2.3) is uniform:

$$F_s = \tau_1 \frac{wh_1}{\sin\phi} \tag{2.15}$$

where h_1 is the uncut chip thickness. Combining equations (2.13-2.15) P_0 can be calculated as follows [23]:

$$P_0 = \tau_1 \frac{h_1(\zeta+1)}{\ell_c \sin\phi} \frac{\cos\lambda_a}{\cos(\phi+\lambda_a-\alpha)} \tag{2.16}$$

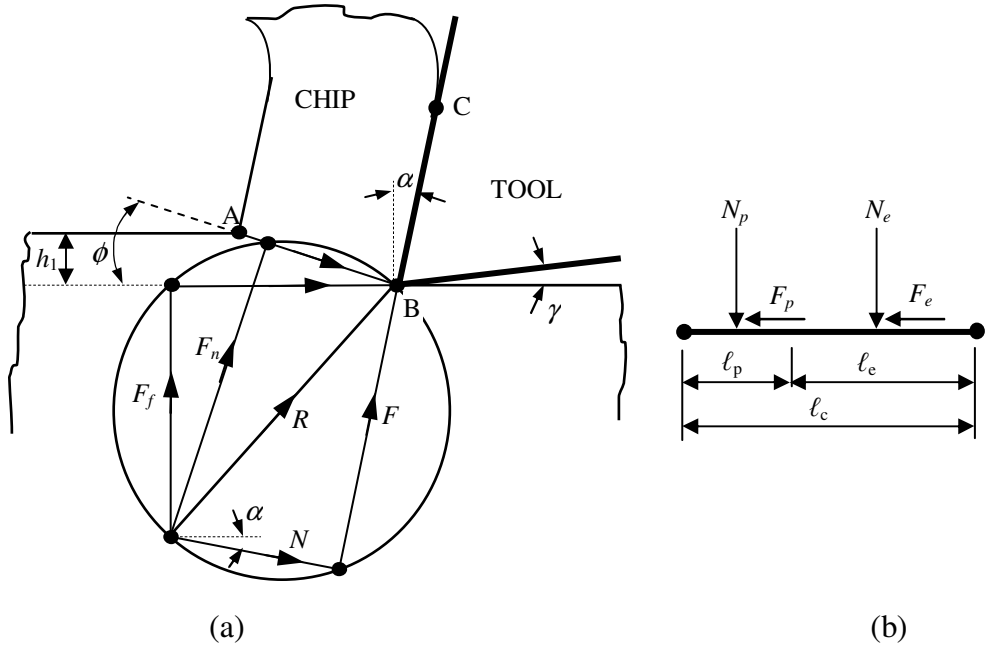

(a) (b)

Figure 2.3: (a) The Merchant's Circle and (b) the schematic representation of the forces acting on the rake face.

The next step is to calculate the contact length ℓ_c. Assuming that the normal stress is distributed uniformly along the shear plane AB, and considering the momentum equilibrium at the tool tip, we get: $M_{AB} = M_{BC}$

$$M_{AB} = F_n \frac{AB}{2} = F_s h_1 \frac{\tan(\phi+\lambda_a-\alpha)}{2\sin\phi} \tag{2.17}$$

$$M_{BC} = \int_0^{\ell_c} xP_0\left(1-\frac{x}{\ell_c}\right)^{\zeta} wdx = F_s \frac{\ell_c}{\zeta+2} \frac{\cos\lambda_a}{\cos(\phi+\lambda_a-\alpha)} \tag{2.18}$$

From equations (2.17) and (2.18), the contact length ℓ_c is obtained as follows [23]:

$$\ell_c = h_1 \frac{\zeta + 2}{2} \frac{\sin(\phi + \lambda_a - \alpha)}{\sin\phi \cos\lambda_a} \tag{2.19}$$

Considering the additional equations (2.16) and (2.19), ℓ_p can be calculated by equation (2.12), for a given value of the shear angle ϕ.

It can be shown that along the sliding zone the equation (2.10) takes the form

$$\tau(x) = \tau_1 \left(1 - \frac{x - \ell_p}{\ell_e}\right)^{\zeta} \qquad \ell_p \le x \le \ell_c \tag{2.20}$$

where ℓ_e is the length of the sliding region, Figure 2.3.b.

In some cases, i.e. high cutting speeds, the friction state at the rake contact can only be sliding. Mathematically this condition occurs when ℓ_p=0 or $\tau_1 > \mu P_0$. Therefore the condition for having sliding all along the rake face can be written, according to equations (2.16) and (2.19), as:

$$A > 1 \tag{2.21}$$

where:

$$A = \frac{\varsigma + 2}{4\mu(\varsigma + 1)} \frac{\sin(2(\phi + \lambda_a - \alpha))}{\sin^2 \lambda_a} \tag{2.22}$$

The only parameter left to be defined is the apparent friction coefficient, μ_a. The apparent friction coefficient is defined as follows:

$$\mu_a = F / N \tag{2.23}$$

The normal force N acting on the rake face can be obtained from equation (2.13) and the friction force F on the rake face can be calculated as follows:

$$F = \int_0^{\ell_p} \tau_1 w dx + \int_{\ell_p}^{\ell_c} \tau_1 \left(1 - \frac{x - \ell_p}{\ell_e}\right)^{\zeta} w dx = \tau_1 w \left(\ell_p + \frac{\ell_e}{\zeta + 1}\right) \tag{2.24}$$

Substituting equations (2.13) and (2.24) into equation (2.23), μ_a is obtained as follows:

$$\mu_a = \frac{\tau_1}{P_0} \frac{\ell_p(\zeta + 1) + \ell_e}{\ell_c} \tag{2.25}$$

It should be noted here that the expression (2.24) is not correct in the case of pure sliding ($A > 1$). Then, the distribution of the shear stress along the rake face is given by (2.10) for $0 \le x \le l_c$ and,

$$F = \int_0^{\ell_c} \tau(x) w dx = \int_0^{\ell_c} \mu P_0 \left(1 - \frac{x}{\ell_c}\right)^{\varsigma} w dx = \mu P_0 \frac{w l_c}{\varsigma + 1} \tag{2.26}$$

By combining (2.13), (2.23) and (2.26) we have: $\mu_a = \mu$.

When sticking occurs, the relationship (2.25) between the apparent (or global) and the local friction coefficients, respectively μ_a and μ can be written, by using (2.12), as:

$$\mu_a = \tan(\lambda_a) = \frac{\tau_1}{P_0}\left(1 + \varsigma\left(1 - \left(\frac{\tau_1}{P_0\,\mu}\right)^{1/\varsigma}\right)\right) \tag{2.27}$$

where:

$$\frac{\tau_1}{P_0} = \frac{\varsigma + 2}{4(\varsigma + 1)} \frac{\sin(2(\phi + \lambda_a - \alpha))}{(\cos\lambda_a)^2} \tag{2.28}$$

which is obtained from equations (2.16) and (2.19).

Substitution of (2.28) into (2.27) provides the relationship between the apparent friction angle λ_a and the local friction coefficient μ, for a given value of ϕ. Finally, the cutting forces F_f and F_c in the feed and tangential directions, respectively, are calculated from the Merchant circle as follows, Figure 2.3.

$$\begin{aligned} F_c &= \tau_1 \frac{w h_1}{\sin\phi} \frac{\cos(\lambda_a - \alpha)}{\cos(\phi + \lambda_a - \alpha)} \\ F_f &= \tau_1 \frac{w h_1}{\sin\phi} \frac{\sin(\lambda_a - \alpha)}{\cos(\phi + \lambda_a - \alpha)} \end{aligned} \tag{2.29}$$

Note that, μ_a can be characterized experimentally by F and N and thus μ_a can be measured by orthogonal tube cutting tests as discussed in the following section.

2.1.3. Material Parameters and Friction Characteristics

The inputs to the proposed model can be divided into three main groups. The first one involves the cutting conditions such as the cutting speed, feed rate and cutting angles used in the process. The second input is the material model coefficients, i.e.

Johnson-Cook parameters in our case, and the third is the sliding friction coefficient μ between the tool and the workpiece material. It should also be mentioned here that both sliding and apparent friction coefficients are unknown in the proposed model. However, one of those can be derived if the other one is given as an input.

In mechanistic approaches, orthogonal tube cutting tests are conducted for different rake angles, cutting speeds, and feed rates to characterize the cutting coefficients [9, 10]. The three major outputs of the orthogonal tube cutting tests are the apparent friction coefficient, the shear stress in the shear plane and the shear angle In the mechanistic approach a large quantity of tests has to be done (in the order of 50). One of the objectives of the present model is to provide the possibility of characterizing the process parameters by doing just a few cutting tests.

For given cutting conditions, the apparent friction coefficient μ_a is characterized from cutting force measurements. The dependence of μ_a upon cutting conditions is obtained by varying the rake angle, the cutting speed and the feed rate. These results are used to determine the sliding friction coefficient μ.

From the measurements of the shear stress on the shear plane, the Johnson-Cook parameters are calibrated by non-linear regression analysis. Determining these parameters from non-cutting tests such as Split Hopkinson Pressure Bar Tests (SHPB) usually provide inaccurate results [88-90]. The strain rates in metal cutting may reach the order of $10^5 s^{-1}$, whereas they are usually restricted to values in the order of $10^3 s^{-1}$ in SHPB tests [91], which is the main reason for the erroneous model predictions.

Once the material model parameters and sliding friction coefficient μ are calibrated the model is able to provide predictions for different cutting conditions for that tool and workpiece couple. Therefore, the proposed model has both calibration and prediction abilities.

Although the relationship between the apparent and sliding friction coefficient is given by equations (2.27) and (2.28) analytically, we would like to provide a simple illustration of this relationship. In Figure 2.4, the stress distributions are shown in order to compare the sliding and apparent friction coefficients. The solid line represents the distribution of the normal stress. The decreasing dashed line is the shear stress distribution, assuming sliding all along the contact zone. In the stick and slip contact problem the shear stress distribution is shown by the dashed line with a plateau in the

stick zone and a continuous decrease in the sliding zone. Observing Figure 2.4, the following characterizations of the friction coefficients can be deduced:

$$\mu = (A+B)/(A+B+C) \tag{2.30}$$

$$\mu_a = A/(A+B+C) \tag{2.31}$$

where A, B, and C are the areas indicated in the Figure 2.4. Clearly from (2.30) and (2.31) the value of μ_a must always be smaller than μ.

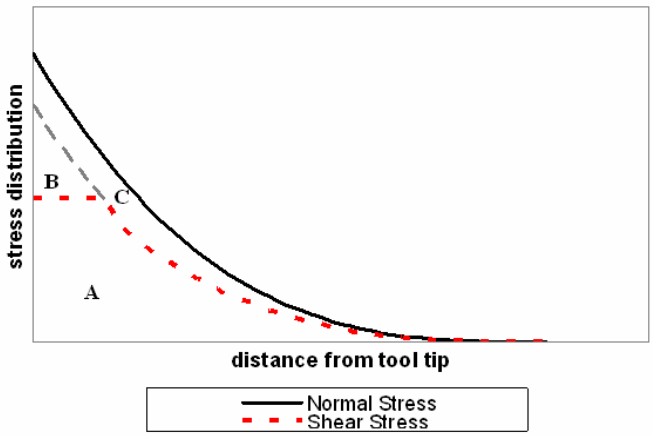

Figure 2.4: The distribution of the stresses on the rake face.

2.1.4. Solution Procedure

In this section, the working of the model is discussed. It is assumed that the primary shear zone has a given thickness of h. The average strain rate $\dot{\gamma}_{av}$ within the shear zone is defined as the shear strain at the exit of the primary shear zone divided by the time for a material particle to cross the shear zone:

$$\dot{\gamma}_{av} = \frac{V\cos\alpha}{h\cos(\phi-\alpha)} \tag{2.32}$$

The effective response of the primary shear zone is defined as the relationship providing the shear stress τ_1 at the exit of the primary shear zone in terms of the shear strain γ_1 and the temperature T_1 at the exit of the primary shear zone and the average strain rate $\dot{\gamma}_{av}$ within the shear zone. It is assumed that this relationship can be described by the Johnson-Cook law, equation (2.1). The coefficients of the material law given in (2.1) are identified so as to get the best fit with the values of τ_1 obtained from the orthogonal tube cutting experiments. Note that the shear force F_s along the shear plane

at the exit of the primary shear zone can be easily obtained by measuring the components of the cutting forces parallel and normal to the cutting direction and by measuring the shear angle ϕ.

After calibration of the Johnson-Cook parameters, the friction law has to be identified. Orthogonal tube cutting tests are used to characterize the local sliding friction coefficient. For given cutting conditions α, h_1 and V, the apparent (or global) friction coefficient μ_a and the shear angle ϕ are measured. If $A > 1$, where A is given by (2.22), no sticking occurs between the chip and the tool. Then the local and global friction coefficients are equal, $\mu=\mu_a$. If $A \leq 1$, there exist a sticking and a sliding zone. From equations (2.27) and (2.28), the local friction coefficient μ is given in terms of the global friction coefficient by:

$$\mu = \frac{\tau_1}{P_0}\left[1+\frac{1}{\varsigma}\left(1-\mu_a\frac{P_0}{\tau_1}\right)\right]^{-\varsigma} \tag{2.33}$$

where τ_1/P_0 is related to $\lambda_a=tan^{-1}(\mu_a)$ by (2.28). The dependence of the sliding friction coefficient μ upon the sliding velocity (chip velocity, V_{chip}) is characterized experimentally by varying the value of the cutting velocity V. The normal pressure P may affect the friction coefficient (to a lower extend than the sliding velocity), as observed for example by Philippon et al. [26]. However, the experimental data generated in this study show that the friction coefficient can be defined accurately using a velocity dependent function only. Then, by fitting the experimental data, a function,

$$\mu = \mu(V_{chip}) \tag{2.34}$$

will be identified in chapter 3 for a given workpiece and a given tool. The chip velocity along the sliding contact length is assumed to be uniform and is calculated as:

$$V_{chip} = V\frac{\sin\phi}{\cos(\phi-\alpha)} \tag{2.35}$$

The second step is the prediction phase. Once the material model parameters and the sliding friction coefficient are calibrated, the proposed model can be used to predict the cutting forces, shear angle, shear stress at the shear plane, normal pressure and shear stress distribution on the rake face, and the length of the sticking and sliding contact zones.

For a given value of the shear angle ϕ, the chip velocity is determined and the value of the local friction coefficient μ is obtained from the law (2.34). The apparent friction coefficient μ_a is then uniquely determined in terms μ by solving the equations (2.27) and (2.28). As soon as μ_a is known, the cutting model provides τ_1, P_0, and ℓ_c and the components of the cutting force. The length ℓ_p of the stick zone is determined by equation (2.12). The pressure distribution along the contact length ℓ_c is given by (2.9). The shear stress distribution is given by (2.10) along the sliding zone and by (2.11) along the sticking zone. Finally, ϕ can be determined by minimizing the cutting energy or by using the empirical Zvorykin law, see Moufki et al. [23]. The cutting forces are given by (2.29).

In this study, ϕ is calculated by minimization of the cutting energy. An example is presented in Figure 2.5 where the cutting power is shown in terms of the shear angle in the range 20º-40º. The shear angle that corresponds to the minimum cutting power (26º) is selected as the predicted value of the shear angle. Note that a coupling does exist between the primary shear zone and the contact zones though the shear angle.

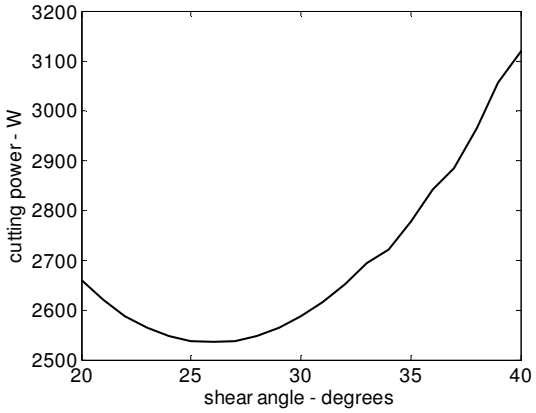

Figure 2.5: The cutting power variation with the shear angle.

2.2. Modeling of Oblique Cutting

The proposed model for oblique cutting involves the primary and the secondary shear zones. Firstly, the shear stress at the exit of the shear band is calculated, and then used to determine the stress distributions on the rake face. The calculation of the basic cutting parameters such as shear angle, chip flow angle etc. is also presented.

2.2.1. Primary Shear Zone Model and JC Parameters

The model for the primary shear zone is adapted from Dudzinski et al. [22]. Similar to the orthogonal cutting model, the material behavior is again represented by a JC constitutive relationship of the form as given in equation (2.1):

The governing equations of the material behaviour at the primary shear zone are obtained by the conservation of momentum, and energy, and the constitutive relationship. τ_0, being the shear stress at the entry of the shear band is calculated by applying the boundary conditions on the strain rate and the temperature at the entry and exit of the shear band. The shear stress at the exit of the shear plane τ_1 is different from τ_0 when inertia effects are important. From the equations of motion for a steady state solution (continuous chip) the shear stress at the exit of the shear zone can be calculated as follows:

$$\tau_1 = \rho(V \sin \phi_n \cos \lambda_s)^2 \gamma_1 + \tau_0 \qquad (2.36)$$

where, λ_s is the inclination angle, ϕ_n is the shear angle in the normal plane, and γ_1 is the shear strain at the exit of the shear band. The JC parameters that are identified using non-cutting tests such as the Split Hopkinson Bar (SHPB) usually provide inaccurate results. The strain rates in metal cutting may reach the order of $10^5 s^{-1}$, whereas they are usually restricted to values in the order of $10^4 s^{-1}$ in SHPB tests. In the previous section it is proposed to calibrate the material model coefficients from orthogonal tube cutting tests. The difference of this approach from the mechanistic method is that the number of calibration tests is much lower. Since the proposed model can handle the effects of the rake angle and the feed rate on the cutting process, only a few cutting tests are needed for calibration.

2.2.2. Dual Zone and Stress Distributions on the Rake

When the material leaves the shear band, it is exerted with a high normal pressure on the rake contact which yields sticking friction conditions at the regions close to the

tool tip. With the decreasing normal pressure the contact conditions return to the sliding (Coulomb) friction. This phenomenon was first proposed by Zorev [3] and was represented in equation 2.8. However, in oblique cutting geometry the normal plane of the tool is different than the chip flow direction. In this case the pressure and shear stress distribution is selected parallel to the chip flow direction (see Figure 2.6). Also the normal pressure *P(x)* distribution is modelled, as given in equation 2.8.

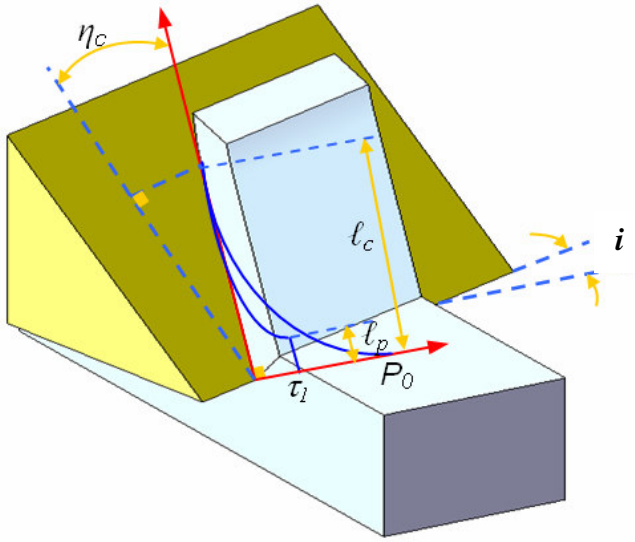

Figure 2.6: The oblique cutting process.

P_0 can be related to the normal force acting on the rake face in the normal direction by considering the pressure distribution along the contact length ℓ_c as follows:

$$N = \int_0^{\ell_c} P_0 \left(1 - \frac{x}{\ell_c}\right)^{\zeta} w_c dx = P_0 \frac{w_c \ell_c}{\zeta + 1} = P_0 \frac{w \ell_c}{\zeta + 1} \frac{\cos \eta_c}{\cos i} \tag{2.37}$$

The normal force is also defined in terms of the shear force on the shear plane as:

$$N = F_s' \frac{\cos \beta_n}{\cos(\phi_n + \beta_n - \alpha_n)} \tag{2.38}$$

where by assuming that the shear force and velocity is in the same direction:

$$F_s' = F_s \cos \eta_s' \tag{2.39}$$

and

$$F_s = \tau_1 A_s = \tau_1 \frac{w h_1}{\sin \phi_n \cos i} \tag{2.40}$$

By equating equations (2.37 and (2.38), P_0 can be obtained as:

$$P_0 = \tau_1 \frac{h_1 (\zeta + 1)}{\ell_c} \frac{\cos \eta_s \cos \beta_n}{\sin \phi_n \cos \eta_c \cos(\phi_n + \beta_n - \alpha_n)} \tag{2.41}$$

where η_s is the shear flow angle, η_c is the chip flow angle, α_n is the normal rake angle, and β_n is the normal friction angle which is defined by:

$$\beta_n = \tan\lambda_a \cos\eta_c \tag{2.42}$$

where λ_a is the friction angle which is related to the apparent friction coefficient μ_a by $\lambda_a = \tan^{-1}\mu_a$..

2.2.3. Contact Lengths

Once the distributions are obtained, similar to the orthogonal cutting case, the sticking contact length can be calculated from equations (2.11) as follows:

$$\ell_p = \ell_c - \ell_c\left(\frac{\tau_1}{P_0\mu}\right)^{1/\zeta} \tag{2.43}$$

Assuming that the normal stress is distributed uniformly on the shear plane, the moment due to the normal shear force acting on the shear plane at the tool tip can be calculated as follows:

$$M_s = \tau_1 \frac{wh_1^2}{2}\frac{\cos\eta_s' \tan(\phi_n + \beta_n - \alpha_n)}{\sin^2\phi_n \cos i} \tag{2.44}$$

Also the moment at the tool tip due to the normal pressure on the rake can be calculated as:

$$M_r = \int_0^{\ell_c} xP_0\left(1 - \frac{x}{\ell_c}\right)^{\zeta} \cos\eta_c w_c dx \tag{2.45}$$

Using equation (2.41) we get:

$$M_r = \tau_1 w \frac{\ell_c h_1}{(\zeta+2)}\frac{\cos\eta_s' \cos\beta_n \cos\eta_c}{\sin\phi_n \cos(\phi_n + \beta_n - \alpha_n)\cos i} \tag{2.46}$$

Due to the moment equilibrium at the tool tip, by equating equations (2.44) and (2.46) the total contact length is obtained as follows:

$$\ell_c = \frac{h_1(\zeta+2)}{2}\frac{\sin(\phi_n + \beta_n - \alpha_n)}{\sin\phi_n \cos\beta_n \cos\eta_c} \tag{2.47}$$

2.2.4. Shear and Chip Flow Angles

Two characteristic parameters of oblique model are the shear and chip flow angles. Assuming that the chip velocity and the friction are collinear and the shear velocity and the shear force are coincident the following relationship can be found as earlier obtained by [32, 92]:

$$\tan(\phi_n + \beta_n) = \frac{\tan i \cos \alpha_n}{\tan \eta_c - \sin \alpha_n \tan i} \tag{2.48}$$

Arranging the equation above we get the following parabolic equation for the chip flow angle η_c:

$$\begin{aligned}&\left(A_1^2 + B_1^2\right)\sin^4 \eta_c - (2A_1 C)\sin^3 \eta_c + 2(A_1 C + CD)\sin \eta_c \\ &+ \left(C^2 - B_1^2 - 2A_1^2 - 2A_1 D\right)\sin^2 \eta_c + \left(A_1^2 + D^2 + 2A_1 D\right) = 0\end{aligned} \tag{2.49}$$

where,

$$A_1 = \tan i(-\tan \phi_n \sin \alpha_n - \cos \alpha_n) \qquad B_1 = \tan \phi_n$$

$$D = \tan i \tan \beta(\cos \alpha_n \tan \phi_n - \sin \alpha_n) \qquad C = \tan \lambda_a \tag{2.50}$$

The shear flow angle η_s can be calculated by the velocity relationships as proposed earlier by Merchant [1] as follows:

$$\tan \eta_s = (\tan i \cos(\phi_n - \alpha_n) - \tan \eta_c \sin \phi_n) / \cos \alpha_n \tag{2.51}$$

2.2.5. Sliding and Apparent Coefficients of Friction

As discussed in Chapter 2.2.4, the rake contact is represented in terms of two friction coefficients, apparent and the sliding. These coefficients are related to each other by the definition of the apparent friction coefficient which is the ratio between the total friction and normal forces acting on the rake face. The total friction force acting on the rake face can be calculated as follows:

$$F = \int_0^{\ell_p} \tau_1 w_c dx + \int_{\ell_p}^{\ell_c} \tau_1 \left(1 - \frac{x - \ell_p}{\ell_e}\right)^{\zeta} w dx = \tau_1 w_c \left(\ell_p + \frac{\ell_e}{\zeta + 1}\right) \tag{2.52}$$

The normal force acting on the rake is represented by the equation (2.38). By the definition of the apparent friction coefficient:

$$\mu_a = \frac{F}{N} \tag{2.53}$$

the relationship between the apparent and sliding friction coefficient is obtained as follows:

$$\mu_a = \frac{\tau_1}{P_0}\left[1 + \zeta\left(1 - \left(\frac{\tau_1}{P_0 \mu}\right)^{1/\zeta}\right)\right] \tag{2.54}$$

where τ_1/P_0 ratio can be calculated from equation (2.41) as follows:

$$\frac{\tau_1}{P_0} = \frac{\ell_c}{h_1(\zeta + 1)} \frac{\sin \phi_n \cos \eta_c \cos(\phi_n + \beta_n - \alpha_n)}{\cos \eta_s \cos \beta_n} \tag{2.55}$$

Note that if one of the friction coefficients is known the other can be calculated from equation (2.54). The sliding friction coefficient as a function of chip velocity v_c is obtained from orthogonal tube cutting tests where the apparent friction coefficient can be measured and used in the prediction of the sliding friction coefficient.

2.2.6. Shear Angle and Cutting Forces

The normal shear angle ϕ_n is calculated by minimization of the cutting energy. It is determined by running a simulation program based on the proposed model for a given range of shear angles, and the one that corresponds to the minimum cutting power is selected as the shear angle. Although the primary and secondary shear zones are modeled separately, they are coupled through the shear angle. Finally, the cutting forces can be calculated by the force equilibrium on the chip as [92]:

$$\begin{aligned} F_t &= \tau_1 w h_1 \left(\cos(\beta_n - \alpha_n) + \tan\lambda_s \tan\eta_c \sin\beta_n\right)/C_1 \\ F_f &= \tau_1 w h_1 \left(\sin(\beta_n - \alpha_n)\right)/\left(C_1 \cos\lambda_s\right) \\ F_r &= \tau_1 w h_1 \left(\cos(\beta_n - \alpha_n)\tan\lambda_s - \tan\eta_c \sin\beta_n\right)/C_1 \end{aligned} \tag{2.56}$$

where,

$$C_1 = \sin\phi_n \sqrt{\cos^2(\phi_n + \beta_n - \alpha_n) + \tan^2\eta_c \sin^2\beta_n} \tag{2.57}$$

The model has also the capability to provide insight on the cutting process. For instance, the normal distribution on the rake face can be calculated. In addition, the proposed model can also predict the temperature distribution along the chip, as shown in Figure 2.7, which is calculated by numerical solution of the two dimensional heat conduction equation. Therefore, in addition to the fast and accurate force predictions, the model may predict the stress and temperature distributions -similar to numerical solutions - but much faster.

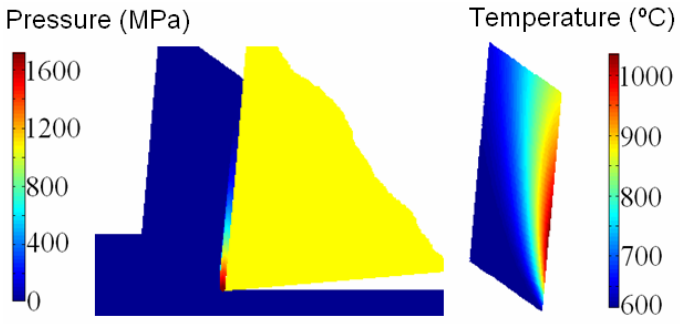

Figure 2.7: Demonstration of the normal pressure on the rake contact and temperature distribution along the chip.

3. EXPERIMENTAL VERIFICATION OF THE PROPOSED MODELS AND INVESTIGATION OF THE FRICTION BEHAVIOR

In this chapter the proposed models in Chapter 2 are verified by several cutting experiments. The comparisons are made in terms of shear angle, friction coefficient, contact length and cutting force predictions.

In the foregoing analysis in Chapter 2, there are two important inputs for the model: the material model parameters and the friction coefficient. It was discussed that the dual zone model can also be used to calibrate the material model coefficients which will be presented in the following section. As for the friction, it should be noted that two friction coefficients are defined: the apparent and the sliding. If one of them is known the other can be calculated by using equation (2.27). The orthogonal tube cutting tests are used for calibration purposes. In addition, non-cutting friction tests were also conducted to compare with the sliding friction coefficients identified from the cutting tests, which are presented and discussed in the next section.

Moreover, the effect of the friction coefficient and contact length on the cutting mechanics and prediction performance is also discussed. At the end of this chapter the effect of the JC material model parameters on the cutting force predictions is presented.

It should be noted here that the thickness of the shear plane is not calculated, but it is a given value. During the analysis, the value of h is taken as 0.025 mm which is a typical value for the steels [22]. Also, the stress distribution exponent ζ is selected as 3, based on the analysis of the split-tool test results [55, 56]. This is also verified by the comparison of the predicted contact lengths with experimental data in Chapter 3.4.

3.1. Calibration of Material Model Parameters

The orthogonal tube cutting tests for calibration are conducted at the cutting speeds of 152 m/min, 216 m/min, and 304 m/min, and at feed rates of 0.05 mm/rev, 007 mm/rev, 0.08 mm/rev, 0.12 mm/rev and 0.16 mm/rev. The cutting insert was P20 grade uncoated carbide tool having 5º rake angle. The Johnson-Cook parameters for AISI 1050 steel are calibrated with the experimental values of the shear stress in the shear plane obtained from the measurements of the cutting forces and of the shear angle as given in Chapter 2.1.4. The calibrated material parameters are listed in Table 3.1.

Table 3.1: JC parameters calibrated by the proposed model for AISI 1050 steel.

A(MPa)	B(MPa)	n	m	ν
880	500	0.234	0.0134	1

Similarly orthogonal tube cutting tests with feed rates of 0.05, 0.1, 0.15, 0.2, 0.25 and 0.3 mm/rev and cutting speeds of 80, 150, 225, 300 and 400 m/min are conducted with AISI 4340 steel and P20 grade uncoated carbide tool having 5º rake angle . The JC parameters are calibrated by using the results of these tests. The calibrated parameters can be found in Table 3.2.

Table 3.2: JC parameters calibrated by the proposed model for AISI 4340 steel.

A(MPa)	B(MPa)	n	m	ν
945	500	0.26	0.015	1

Finally, orthogonal tube cutting tests with feed rates of 0.06, 0.12, and 0.18 mm/rev and cutting speeds of 3, 6, and 10 m/min are conducted with Ti6Al4V alloy and HSS tools. In this case tools with different rake angles are used for comparison purposes with mechanistic model: The calibrated JC parameters are listed in Table 3.3.

Table 3.3: JC parameters calibrated by the proposed model for Ti6Al4V alloy.

A(MPa)	B(MPa)	n	m	ν
649	490	0.28	0.028	1

The JC parameters calibration and effects on the prediction of cutting forces are discussed later in Chapter 3.9 in detail.

3.2. Friction Coefficient Calibration and Comparison with Non Cutting Friction Test Results

3.2.1. Non-Cutting Friction Test Setup

Firstly it should be mentioned that the non-cutting friction tests are performed in order to compare the results with the identified friction coefficients from the cutting model, and they are not needed in regular identification procedure. In order to obtain the sliding coefficient of friction between the workpiece and the cutting tool materials a non-cutting friction test setup is prepared. The setup is built on a manual lathe. As can be seen in Figure 3.1, the setup involves a dynamometer in order to measure the normal and the friction forces, a fine slider in order to make the initial contact between tool and workpiece smoother, and a DAQ setup in order to collect the data. Uncoated and coated carbide rods are used in the experiments as the tool material. The contact between the tool and workpiece is realized by moving the tool with a fine slider in order to make the initial contact smoother. The sliding friction speed is controlled by the rotational speed of the work material and the radial position of the carbide rod with respect to the center of rotation. The sliding coefficient of friction is calculated using the mean values as shown in Figure 3.2 for an example case:

$$\mu = F_{friction} / F_{normal} \tag{3.1}$$

Figure 3.1: The non-cutting test setup.

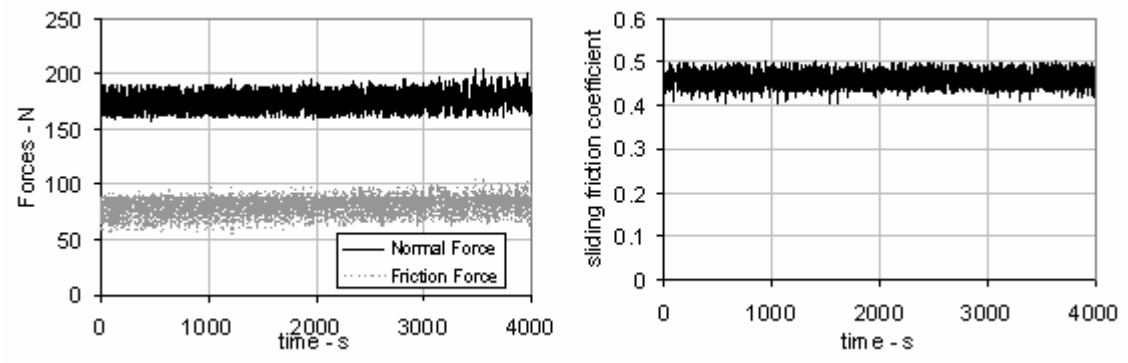

Figure 3.2: An example case of calculating the mean Coulomb friction coefficient by measured force data at 420 m/min friction speed.

3.2.2. Friction Test Results

In this section, the sliding friction coefficients that are identified by the proposed model from the orthogonal tube cutting tests are presented, and discussed for two cases. In the first case, AISI 1050 steel with different cutting tools is presented where in the second case AISI 4340 steel and Ti6Al4V alloy are investigated. All the cutting tests are conducted in orthogonal conditions with TPGN type tools having 5º of rake angle except HSS cutting tool used in Ti6Al4V tests. Uncoated and coated carbide rods are used for non-cutting friction tests and the results are compared with the sliding friction coefficients obtained from the model using cutting tests data. Note that the non-cutting friction tests are not conducted for all the workpiece-tool couples.

In the first case, the sliding friction coefficients between AISI 1050 steel and four different cutting tools were identified. The orthogonal cutting test parameters for those cases are presented in Table 3.4. Using the apparent friction coefficients identified from the tests, the sliding friction coefficients are determined by the model discussed in Chapter 2.1. The results can be found in Figure 3.3.

Table 3.4: The materials and cutting parameters used during the orthogonal tests.

Cutting Tool Material	Workpiece Material	Feed Ranges (mm/rev)	Cutting Speed Ranges (m/min)
Uncoated Carbide (P20)	AISI 1050	0.05-0.16	150-300
Coated Carbide (TT1500)			150-600
Ceramic (AB30)			215-1225
CBN (TB650)			150-1225
Uncoated Carbide (P20)	AISI 4340	0.05-0.3	80-500
HSS (T100)	Ti4Al6V	0.06-0.18	3-10

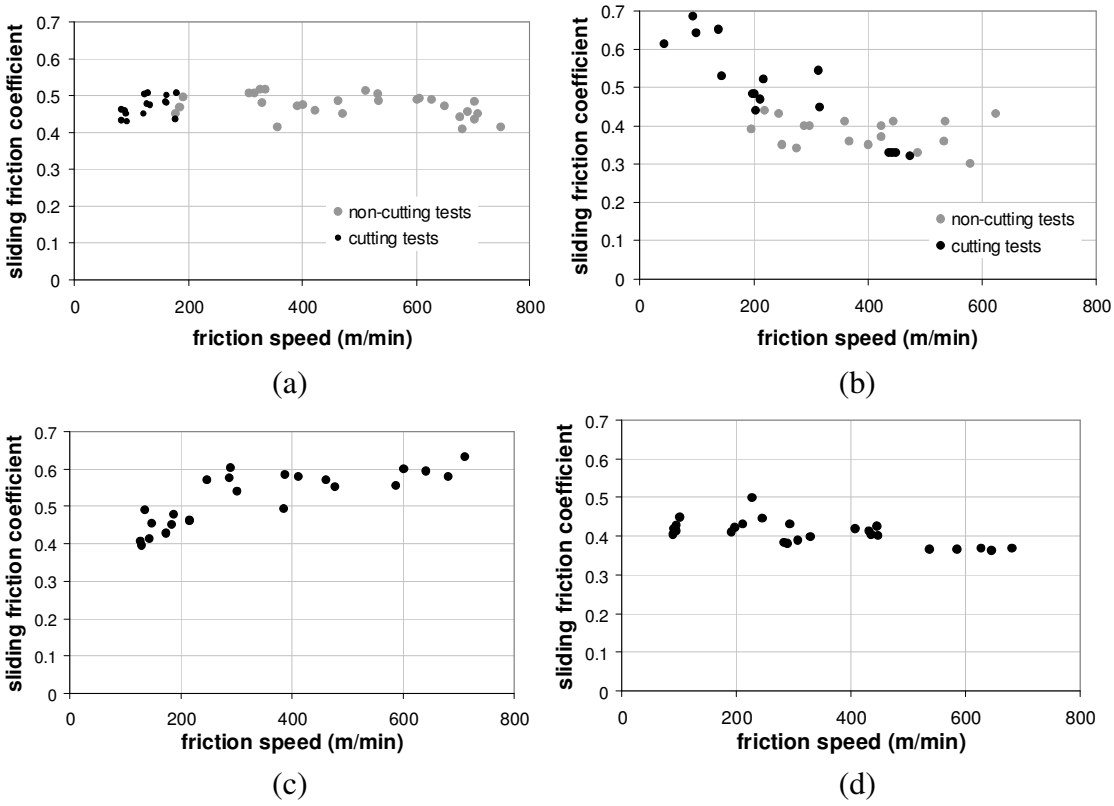

Figure 3.3: Sliding friction coefficients between AISI 1050 steel and (a) uncoated carbide, (b) coated carbide, (c) ceramic, and (d) CBN tools with varying friction speeds.

Observing the results given in Figure 3.3, it can be deduced that the friction characteristics are different for all the cutting tools. As can be seen in Figure 3.3.a, the sliding friction coefficient between the uncoated carbide tool and AISI 1050 steel does not depend on the friction speed strongly. But, there is a slight decrease in the sliding coefficient of friction at moderate speeds. However, for the ceramic (Figure 3.3.c) and CBN (Figure 3.3.d) tools, the sliding friction coefficient has almost a linear relationship with the friction speed where its value increases with the speed for the ceramic tool and decreases for the CBN tool. For the last cutting tool, the coated carbide, the sliding friction coefficient has a non-linear decreasing relationship with the friction speed. For this tool, the sliding friction coefficient drastically decreases from 0.7 (at slow cutting speeds) to 0.3 (at high cutting speeds).

Another interesting conclusion is that the sliding friction coefficients obtained from non-cutting friction tests have a very close agreement with the ones obtained from the cutting model and the tests. It should be noted that the average pressure on the rake

face during cutting (200-600 MPa) is higher than the pressure applied during non-cutting tests (50-150 MPa). This observation suggests that the pressure may not affect the sliding friction strongly for these material-tool couples.

A final observation from the data presented in Figure 3.3 is that the sliding friction decreases with the friction speed for all the tools except the ceramic insert. The reduction of the sliding friction coefficient with the speed can be attributed to the increased temperature at the contact. However, there is a need for further investigation in order to explain the different friction behavior of ceramic tools.

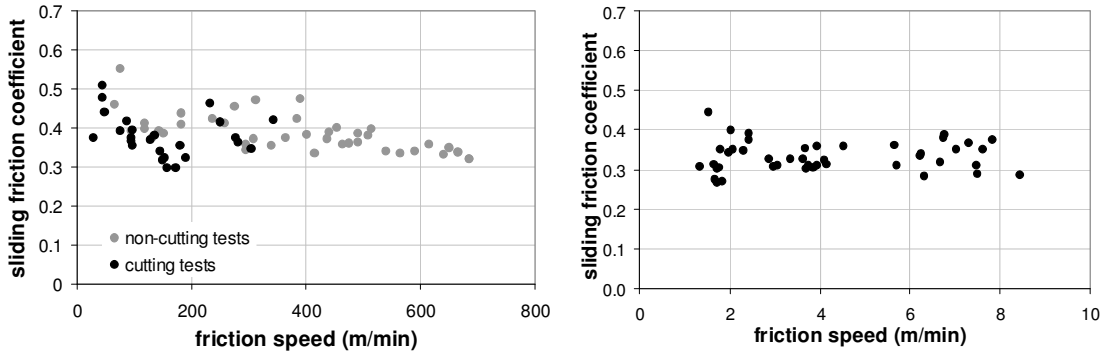

(a) (b)

Figure 3.4: Sliding friction coefficients between (a) AISI 4340 steel and uncoated carbide tool and (b) Ti6Al4V alloy with HSS cutting tool with varying friction speeds.

In the second case, two different workpiece material types are investigated: AISI 4340 steel with uncoated carbide tool and Ti6Al4V alloy with HSS cutting tool. The orthogonal cutting conditions can be found in Table 3.4, and the results can be seen in Figure 3.4. The sliding friction coefficient between AISI 4340 steel and uncoated carbide tool (Figure 3.4.a) has a decreasing trend with the friction speed from 0.55 to 0.3. However, at higher speeds it takes almost a constant value of 0.35. On the other hand, the sliding friction coefficient between Ti6Al4V alloy with HSS cutting tool has a linear relationship with the speed and the average value is 0.35. Comparing the results of AISI 1050 (Figure 3.3.a) and AISI 4340 steel (Figure 3.4.a) with uncoated carbide tool, it can be concluded that AISI 4340 steel has a lower sliding friction coefficient. This can be attributed to the fact that the test materials had different hardness values. AISI 1050 steel had an average surface hardness of 190 BHN whereas it was 240 BHN for AISI 4340 steel.

Finally the calibrated sliding friction coefficients with respect to the friction speed which corresponds to the chip velocity in cutting can be found in Table 3.5.

Table 3.5: Calibrated sliding coefficients of friction.

Material – Tool	μ_s (V in m/min)
AISI 1050 – Uncoated Carbide	$0.398 + 6.120\times10^{-4}V$
AISI 1050 – Coated Carbide	$0.8932 + 1\times10^{-6}V^2 - 0.0016V$
AISI 1050 – CBN	$0.431 - 7\times10^{-5}V$
AISI 1050 – Ceramic	$0.4311 + 2\times10^{-4}V$
AISI 4340 – Uncoated Carbide	$0.513 + 4.734\times10^{-6}V^2 - 1.872\times10^{-3}V$
Ti6Al4V – HSS	$0.326 + 1.1\times10^{-3}V$

3.3. Shear Angle Predictions

As discussed earlier the shear angle is determined based on the minimum cutting power calculations. The total cutting energy is calculated by the energy spent for the chip formation and the contact on the rake face. The model is run for a selected range of shear angles, and the shear angle corresponding to the minimum cutting energy is selected. The minimum energy method has been commonly used for the analysis of shear angle in cutting since Merchant [1], and thus it is applied in this study as well. The shear angle is also experimentally identified from the tube cutting tests through chip thickness measurements [10]. The prediction results along with the model predictions can be seen in Figure 3.5.a for the AISI 1050 steel and tool with 5º rake angle, in Figure 3.5.b for the tool with the rake angle of -5º, and in Figure 3.5.c for AISI 4340 steel with tool having 5º rake angle. The maximum difference between the proposed model predictions and the experimental results is around 30% for both ranges, whereas the average error is around 11%. The discrepancy could be attributed to many factors such as measurement errors. However, recently Molinari and Moufki [93] have shown that the stability analysis of the chip formation combined with the minimum energy approach may yield different shear angle values than the ones predicted by the simple minimum energy approach. This could be another source of the discrepancy in the predictions.

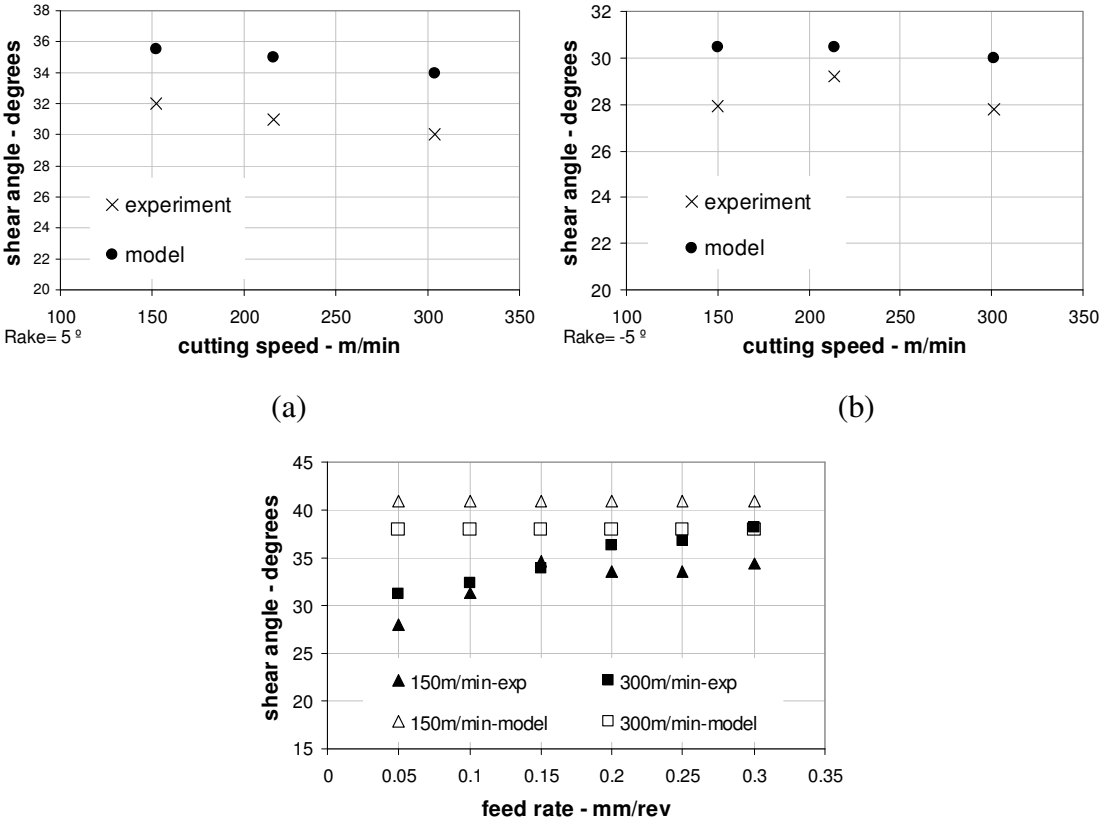

Figure 3.5: Shear angle predictions by the model along with the experimental results for the AISI 1050 steel and the cutting tool having rake angle of (a) 5º and (b) -5º and (c) for the AISI 4340 steel with the cutting tool having rake angle of 5º.

3.4. Contact Length Predictions

Although the primary output of the proposed model is the cutting forces, the lengths of the sticking and sliding zones are also predicted. Accurate prediction of the contact lengths is necessary for force modeling, and is very critical for the calculation of the temperature distribution which will be studied in a later research. Therefore, in order to verify the calculated contact lengths, several measurements are done on the rake face using a microscope. Using optical methods is a simple and efficient way to characterize the contact length. The orthogonal tube cutting tests were conducted again with the cutting conditions that are listed in Table 3.6. It should be noted here that although the experimental results are mainly on the uncoated carbide inserts, coated carbide inserts

are also used in this section as the contact lengths can be more clearly seen on these inserts.

Table 3.6: The cutting tests conducted to verify the contact lengths.

Test No	1	2	3	4	5	6	7	8	9	10	11	12	13	14
Rake Angle	5 °												-5°	
Insert type	U*						C*						U*	
Cutting Speed m/min	306	306	217	217	153	153	613	613	306	306	153	153	306	217
Feed Rate mm/rev	0.08	0.24	0.08	0.24	0.08	0.24	0.08	0.24	0.08	0.24	0.08	0.24	0.24	0.24

*Uncoated carbide insert (P20 Grade) **Coated carbide insert(TT1500 grade)

The comparisons of the total contact and the sticking zone lengths with the experimental results can be seen in Figure 3.6.a and Figure 3.6.b, respectively. During the microscope measurements, the sliding marks can be seen very clearly (see Figure 3.7). The regions close to the tool tip where the sliding marks couldn't be observed is defined to be the sticking region, and corresponding length is measured. However, as can be observed from Figure 3.7.a and Figure 3.7.b we didn't observe sharp borders for the total contact and the sticking zone lengths, where mostly a transition range is observed. The beginning and the final distances of these transition ranges to the cutting tip are represented by the bold vertical bars in Figure 3.6 which corresponds to the minimum and maximum length of the related regions, respectively.

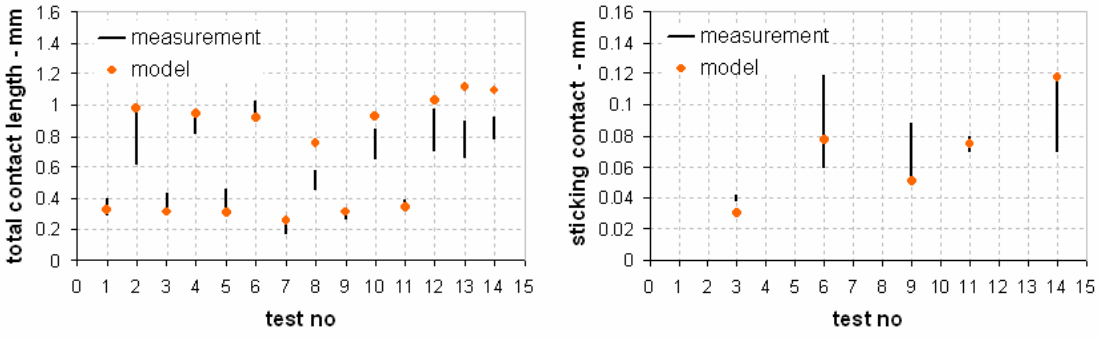

(a) (b)

Figure 3.6: (a) Total contact length and (b) Sticking contact length.

A good agreement is observed for the total contact length predictions. However, there were some difficulties measuring the sticking contact length especially for uncoated carbide tools. The sticking contact region was more apparent for the coated carbide tools due to the clear mark left by the chip on the coating face. Another important point is that most of the calculated sticking zone lengths are comparable to the hone radius of the insert which is around 35-45 μm. In those cases we couldn't observe a noticeable sticking region during the microscope measurements as one would expect. However for a successful case, e.g. case 11, the sticking contact region was observed clearly during the microscope inspections which can be seen in Figure 3.7.b. The total contact length for this case can be seen in Figure 3.7.a.

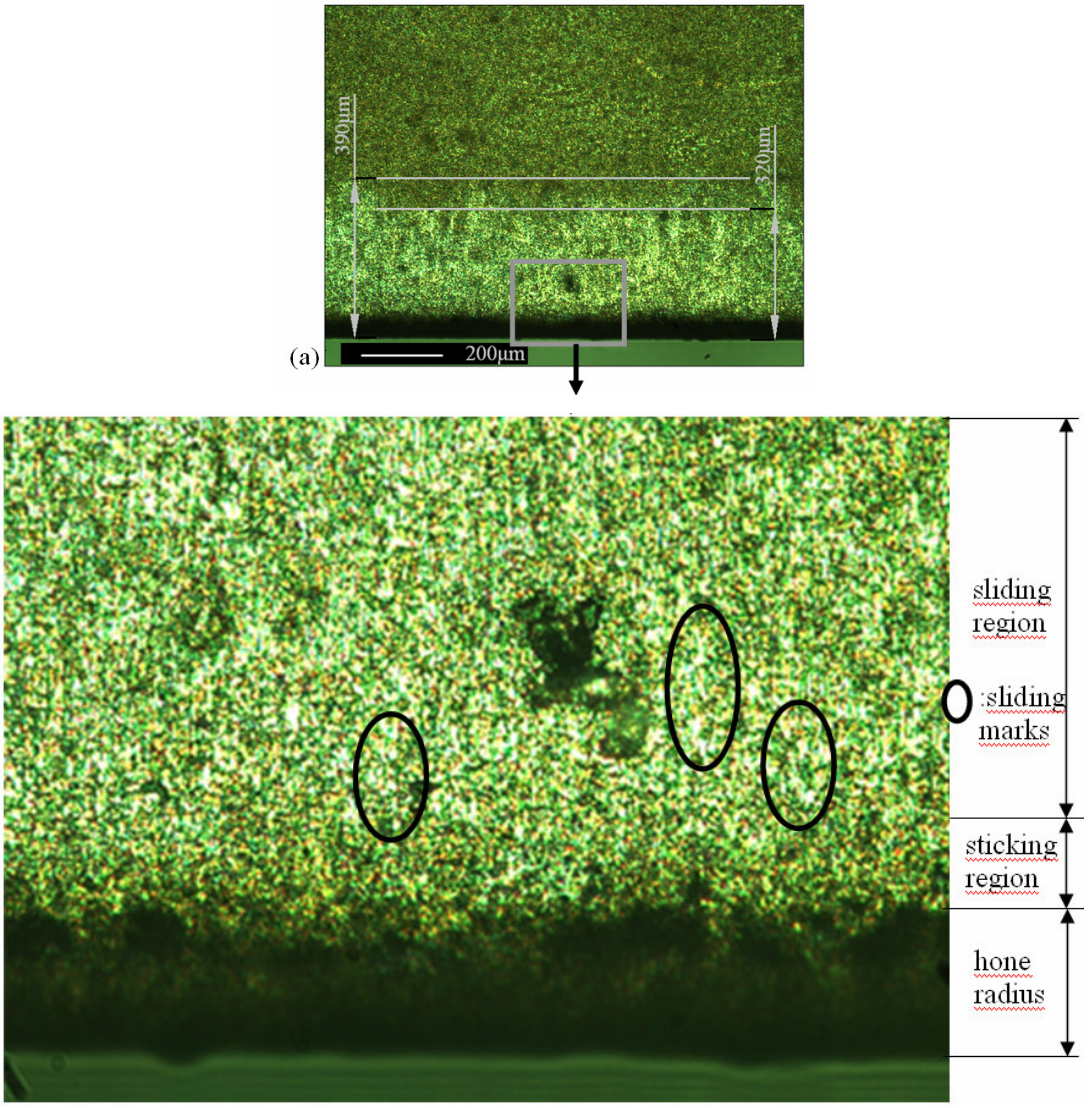

(b)

Figure 3.7: The microscope measurements for the test case 11 (a) 50X magnification for the total contact length and (b) magnified region for the sticking length.

3.5. Cutting Force Predictions

In this section, the cutting forces that are predicted by the proposed model are compared with the experimental results for various feed rates and cutting speeds. The verification experiments for orthogonal cutting model are conducted for AISI 1050 steel with uncoated carbide tool, AISI 4340 steel with uncoated carbide tool and Ti6Al4V alloy with HSS cutting tool. Also additional comparison is between the proposed model and the mechanistic model for Ti6Al4V alloy experiments. Also verification experiments for the oblique model are conducted with Ti6Al4V alloy and HSS cutting tools having inclination angles of 7º and 11º. It should be noted here that the edge cutting forces are not taken into account in the comparisons as the proposed models cannot predict them.

3.5.1. Cutting Force Predictions for AISI 1050 Steel and Uncoated Carbide Tool

Firstly it should be noted that all the calibrations for AISI 1050 steel are done with the tool having 5º rake angle. In the comparisons results with the tool having -5º rake

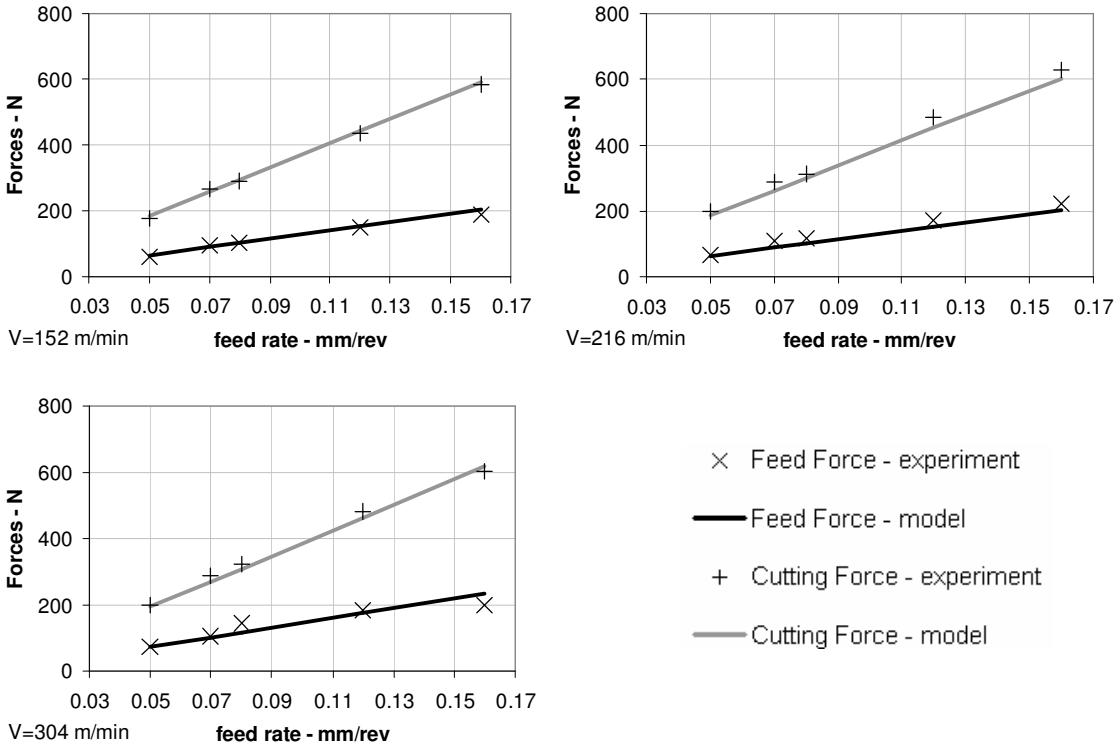

Figure 3.8: The comparison between the predicted and measured cutting forces for AISI 1050 steel with the tool having 5º rake angle at cutting speeds of (a) 152 m/min, (b) 216 m/min and (c) 304 m/min.

angle is also presented in order to show the predictions which are out of the calibration range. The results for the cutting tool with rake angle 5º and -5º can be found respectively in Figure 3.8 and Figure 3.9 for three different cutting speeds. As can be observed, a very good agreement is found between the model predictions and the experimental data. The maximum and the average discrepancies are 15% and 3%, respectively, which is mainly due to the inaccuracy in the material model.

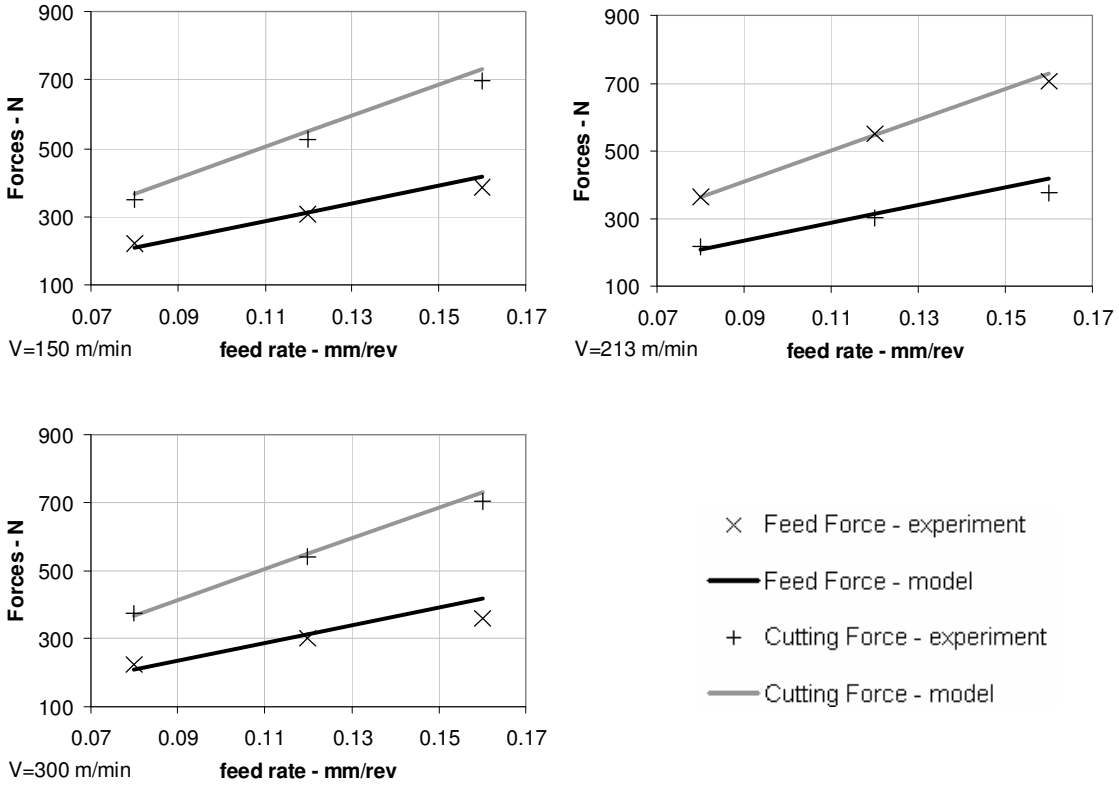

Figure 3.9: The comparison between the predicted and measured cutting forces for AISI 1050 steel with the tool having -5º rake angle at cutting speeds of (a) 150 m/min, (b)213 m/min, and (c) 300 m/min.

3.5.2. Cutting Force Predictions for AISI 1050 Steel and Coated Carbide Tool

The cutting force predictions of AISI 1050 steel with coated carbide tool with the proposed model are given in Figure 3.10 for different cutting speeds and varying feed rates along with the experimental results. As can be observed, a good agreement is found between the model predictions and the experimental data. The maximum and the average discrepancies are 27% and 10%, respectively which is mainly due to the inaccuracy in the material model and from measurement errors.

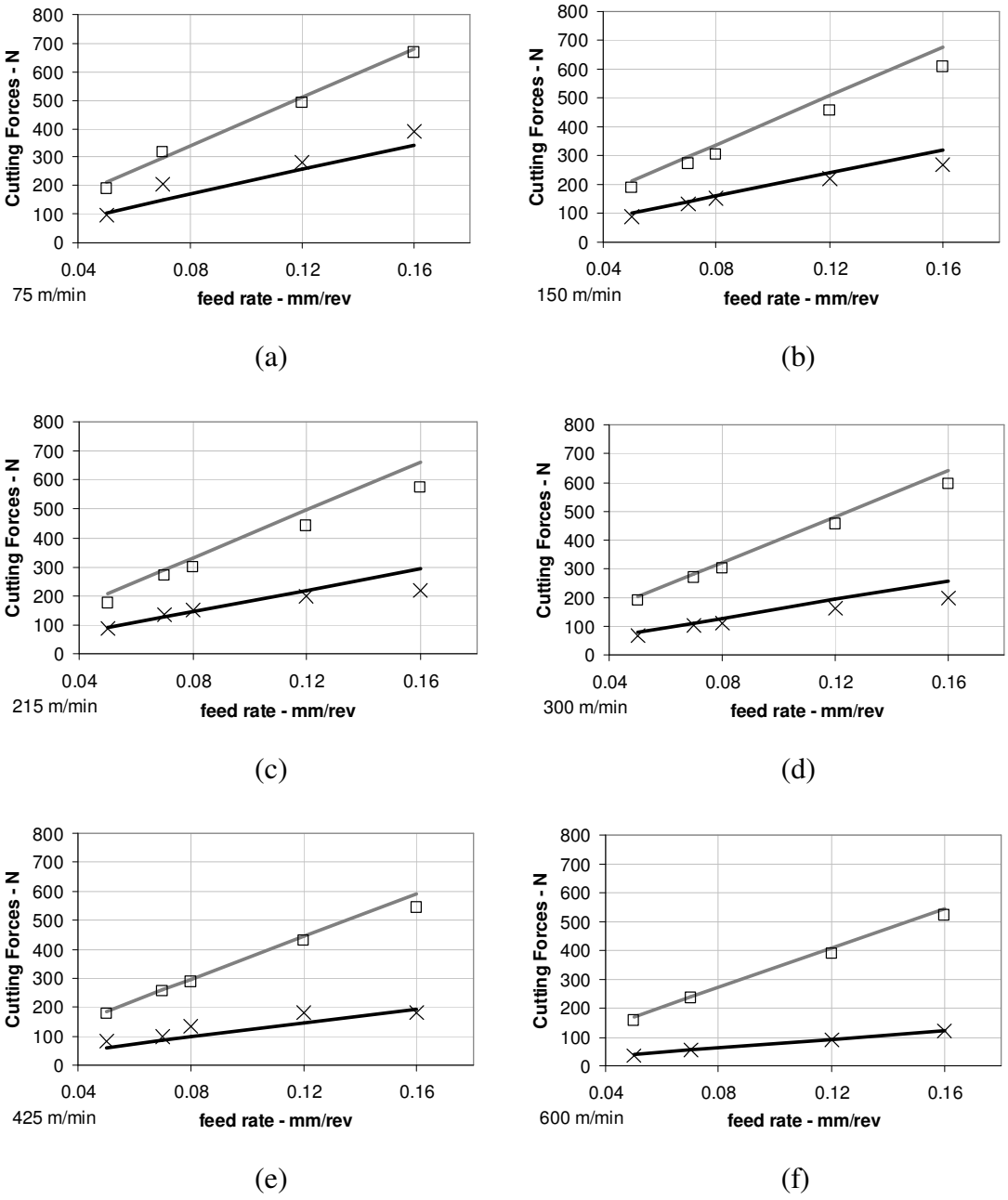

Figure 3.10: The comparison between the predicted and measured cutting forces for AISI 1050 steel with coated carbide tool at cutting speeds of (a) 75 m/min, (b)150 m/min, (c) 215 m/min, (d) 300 m/min, (e) 425 m/min, and (f) 600 m/min.

3.5.3. Cutting Force Predictions for AISI 4340 Steel and Uncoated Carbide Tool

The cutting force predictions of AISI 4340 steel with uncoated carbide tool are given in Figure 3.11 for different cutting speeds and varying feed rates along with the experimental results. As can be observed, a good agreement is found between the model predictions and the experimental data. The maximum and the average discrepancies are

35% and 10%, respectively. The error is higher at cutting speed of 80 m/min due to the built-up edge conditions at those cutting speeds [10].

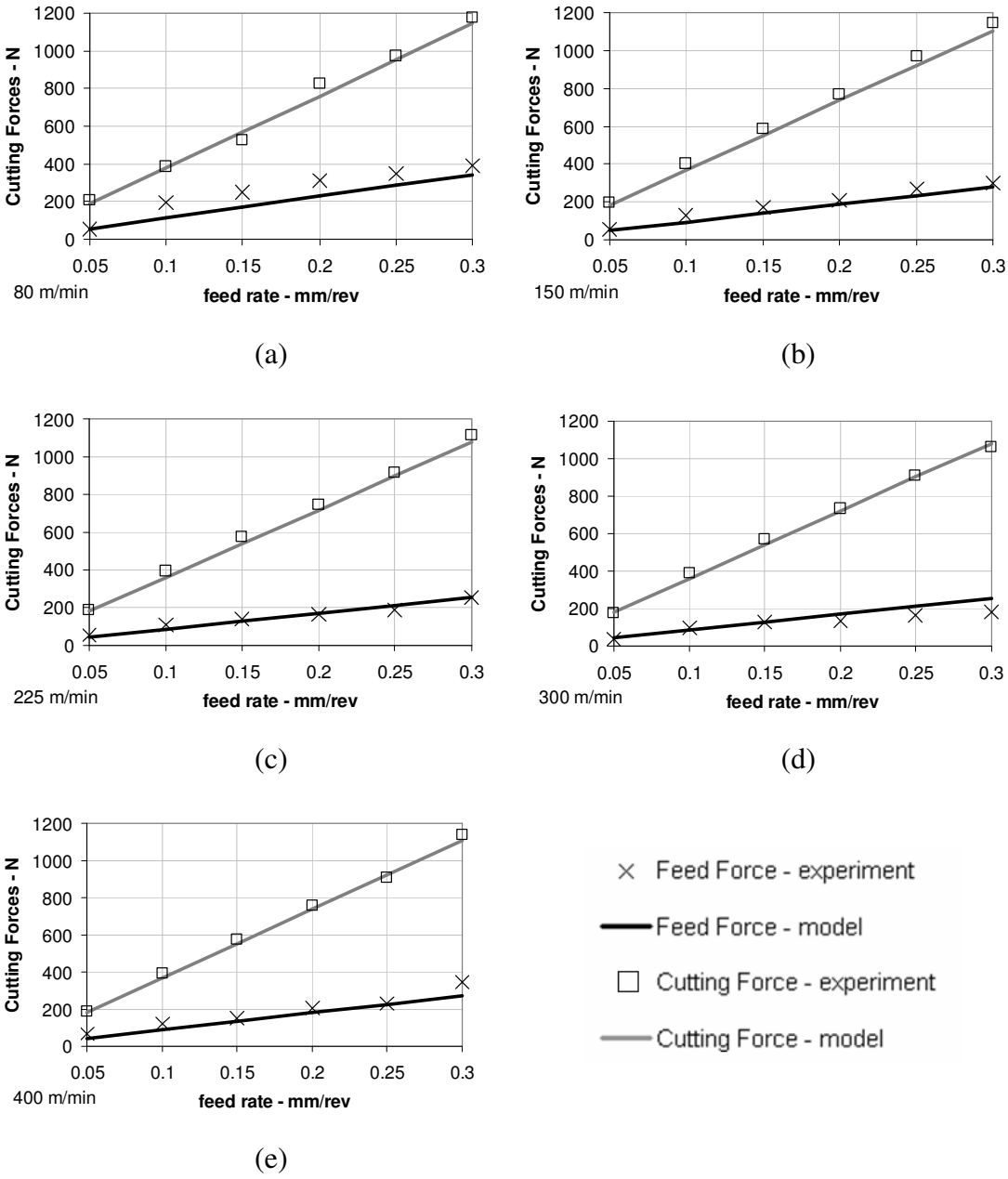

Figure 3.11: The comparison between the predicted and measured cutting forces for AISI 4340 steel at cutting speeds of (a) 80 m/min, (b)150 m/min, (c) 225 m/min, (d) 300 m/min, and (e) 400 m/min.

3.5.4. Cutting Force Predictions for Ti6Al4V Alloy and HSS Tool and Comparison with Mechanistic Model

The cutting force predictions of Ti6Al4V alloy with HSS cutting tool with the proposed model in Chapter 2.1 are given below for different cutting speeds and varying feed rates and rake angles along with the experimental results. Below (Figure 3.12) is the general error comparison for the total of 36 cutting tests with tool having rake angles of 0º, 3º, 6º, and 12º and a clearance angle of 3º. The *x* axis represents the prediction error by the dual zone and the mechanistic models; *y* axis on the other hand represents the percentage of the tests which corresponds to that error range. For example the dual zone model predictions for the feed forces showed that 40% of the predictions give lower than 10% error. The agreement between the experiments and proposed model is found to be good. Also observing Figure 3.12 it can be deduced that mechanistic model was less successful in terms of modeling the feed force compared with the proposed model.

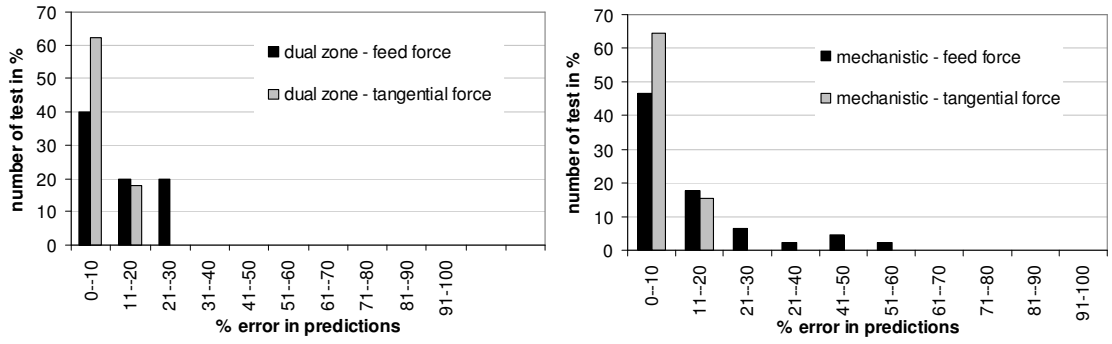

(a) (b)

Figure 3.12: Overall comparison of the errors from the experimental cutting forces between proposed model and the mechanistic model.

The specific comparisons for each test with the tools having rake angles of 0º, 3º, 6º, and 12º can be seen in Figure 3.13, Figure 3.14, Figure 3.15, and Figure 3.16, respectively for different cutting speeds and varying feed rates.

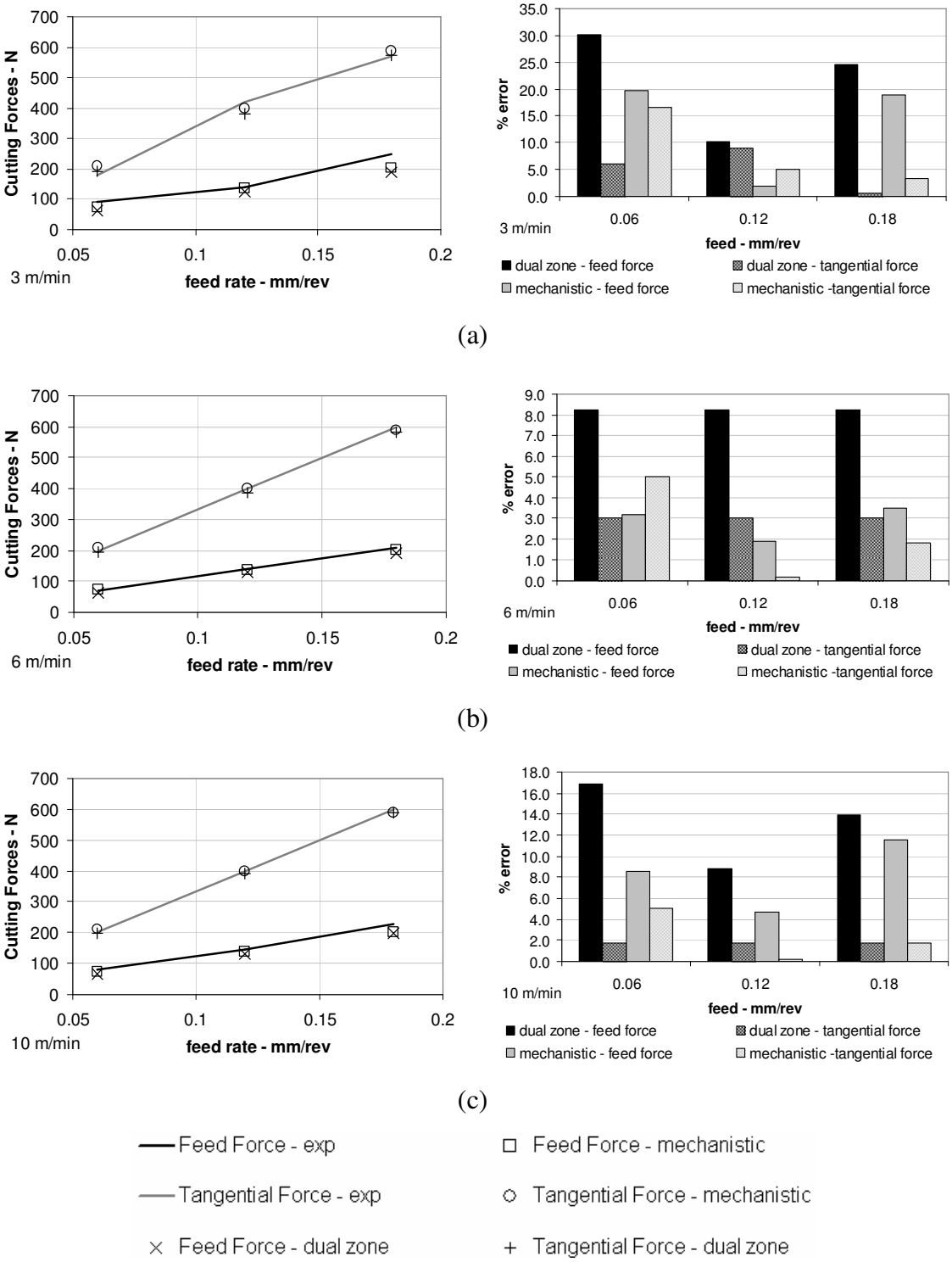

Figure 3.13: The comparison of cutting forces for Ti6Al4V alloy with HSS tool having 0º rake angle at cutting speeds of (a) 3m/min, (b) 6 m/min, and (c) 10 m/min.

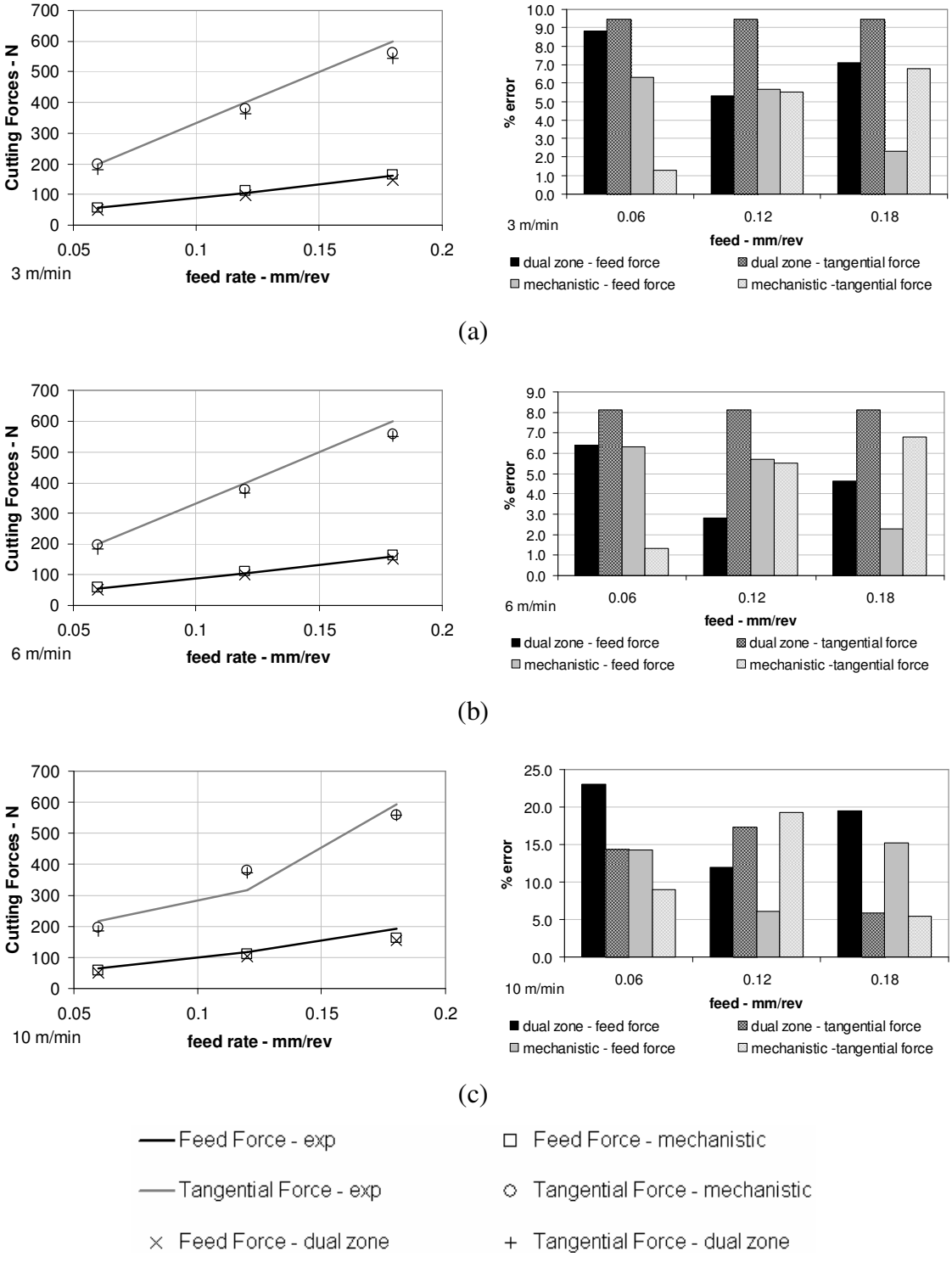

Figure 3.14: The comparison of cutting forces for Ti6Al4V alloy with HSS tool having 3º rake angle at cutting speeds of (a) 3m/min, (b) 6 m/min, and (c) 10 m/min..

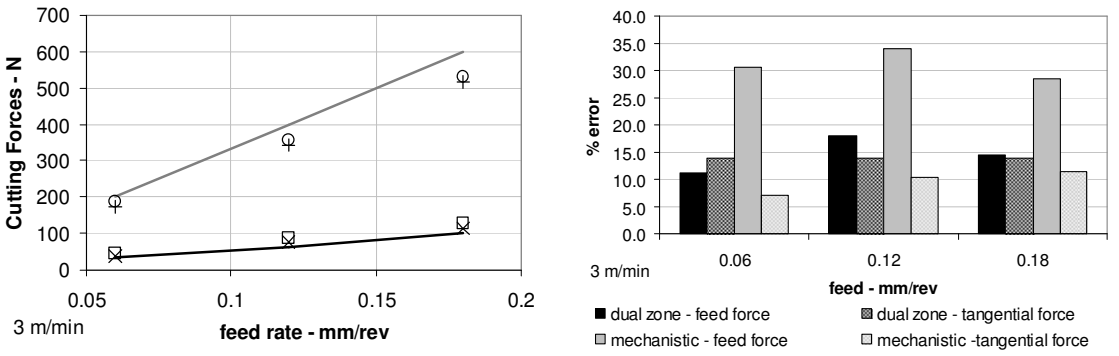

(a)

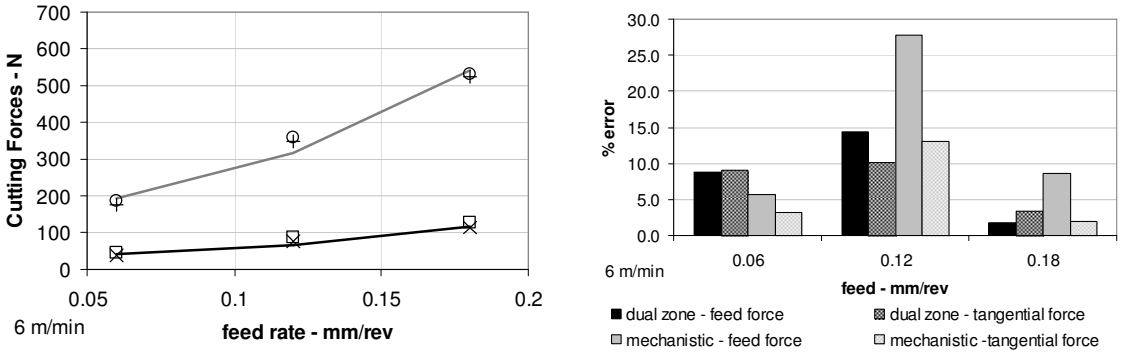

(b)

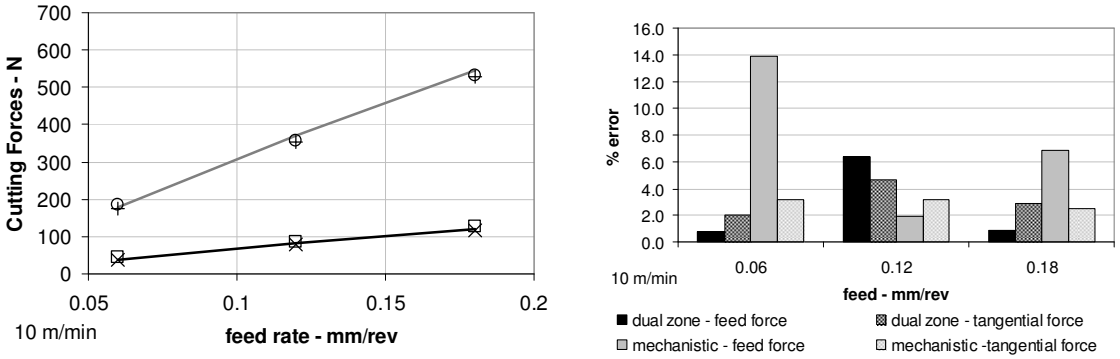

(c)

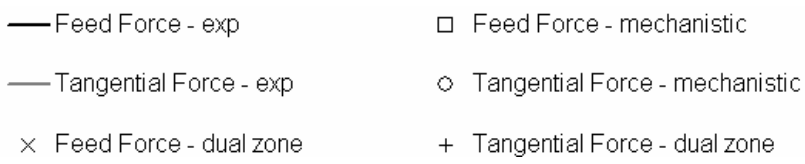

Figure 3.15: The comparison of cutting forces for Ti6Al4V alloy with HSS tool having 6º rake angle at cutting speeds of (a) 3m/min, (b) 6 m/min, and (c) 10 m/min.

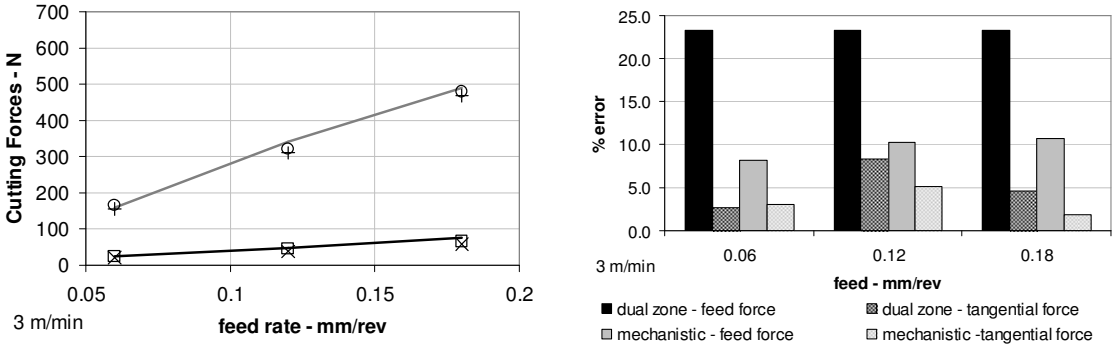

(a)

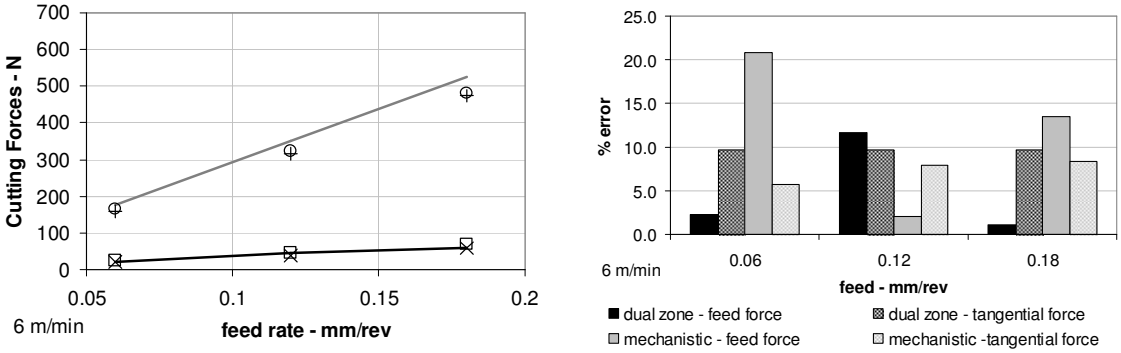

(b)

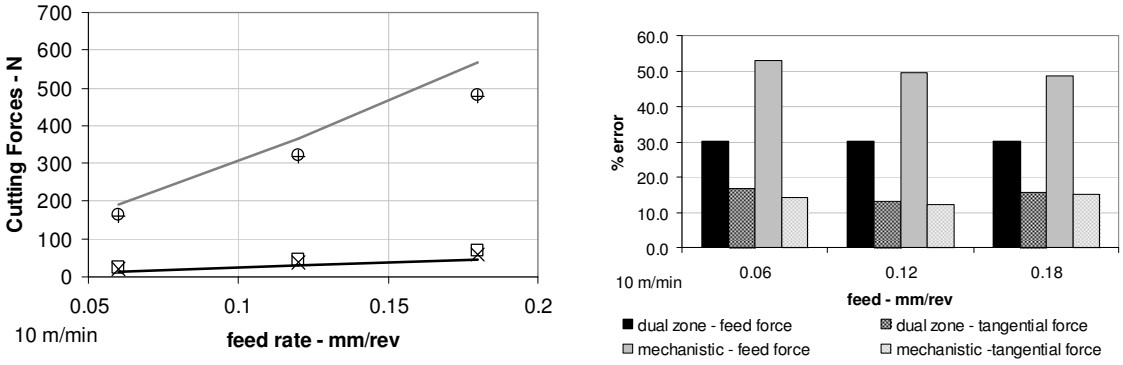

(c)

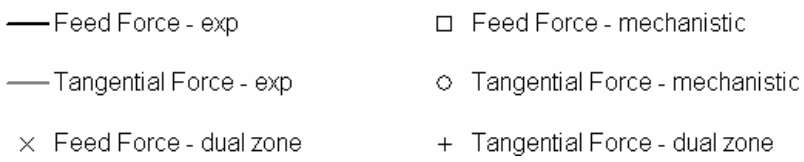

Figure 3.16: The comparison of cutting forces for Ti6Al4V alloy with HSS tool having 12º rake angle at cutting speeds of (a) 3m/min, (b) 6 m/min, and (c) 10 m/min.

The calibrations for the material model parameters and friction coefficients for Ti6Al4V alloy were done by the test results conducted with positive rake angles. In order to compare the model for the out of calibration range, tests with tools having negative rake angles of -5º and -10º were conducted. The prediction results along with the experiments and comparison with the mechanistic model can be found in Figure 3.17, and Figure 3.18.

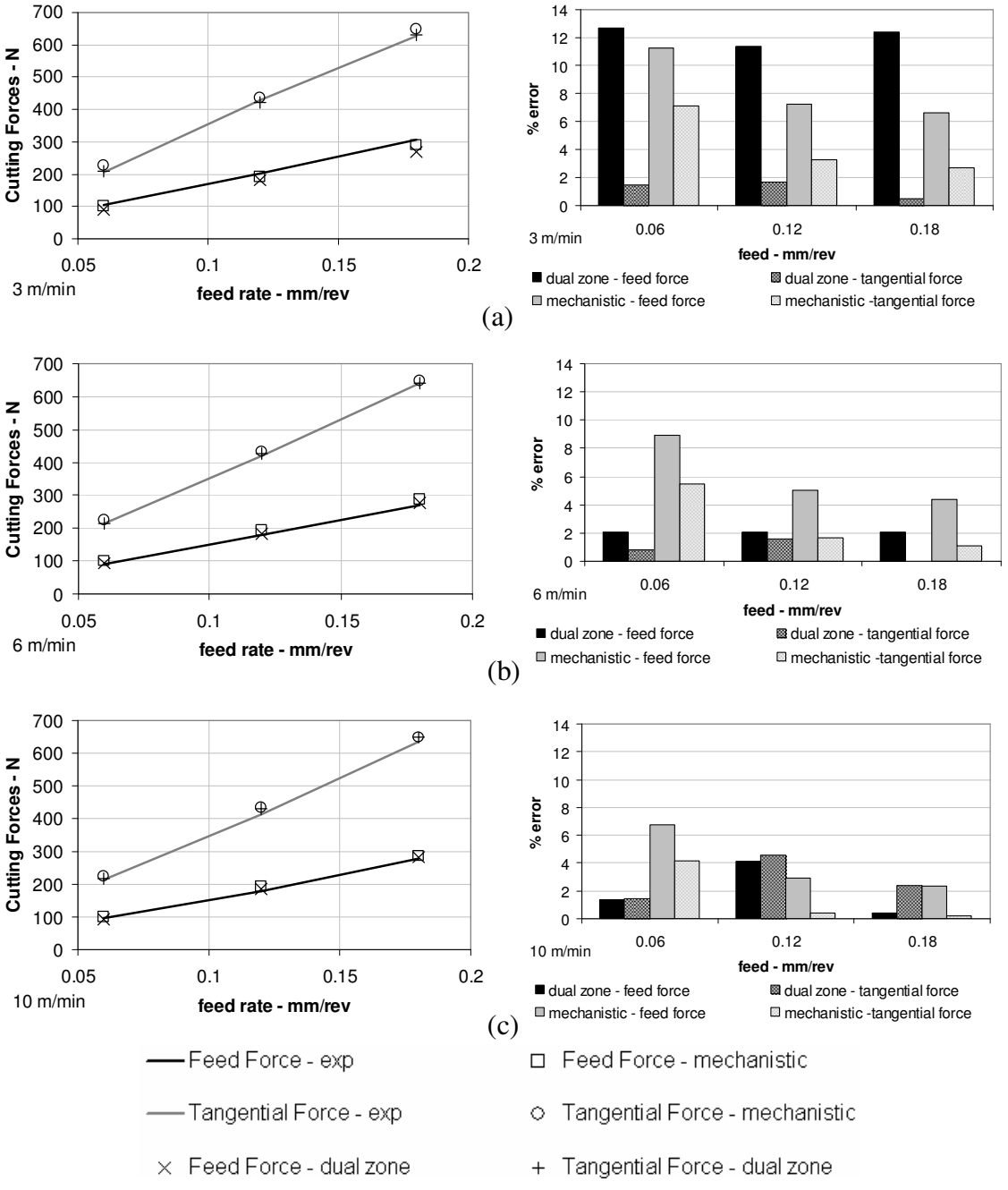

Figure 3.17: The comparison of cutting forces for Ti6Al4V alloy with HSS tool having -5º rake angle at cutting speeds of (a) 3m/min, (b) 6 m/min, and (c) 10 m/min.

Again, especially in feed force predictions, it can be deduced that proposed model is superior to the mechanistic model. And overall good agreement is observed between the proposed model predictions and experimental results.

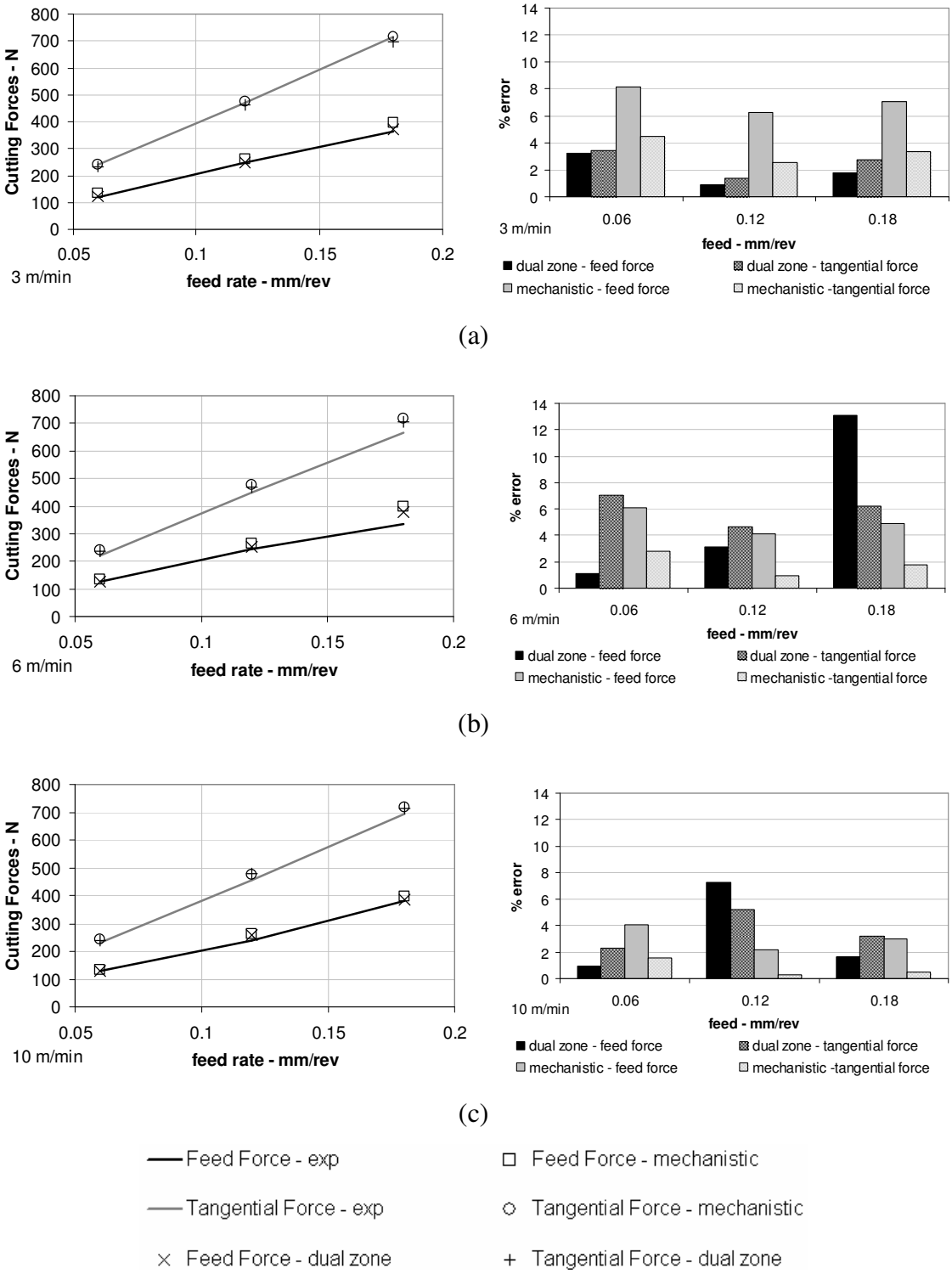

Figure 3.18: The comparison of cutting forces for Ti6Al4V alloy with HSS tool having -10º rake angle at cutting speeds of (a) 3m/min, (b) 6 m/min, and (c) 10 m/min.

3.5.5. Cutting Force Predictions for Oblique Cutting

Oblique cutting tests were conducted in order to verify the proposed cutting model in Chapter 2.2. The workpiece material was Ti6Al4V alloy, and HSS cutting tools were ground with inclination angles of 7º and 11º and rake angles of 0º. The cutting tests were performed at 10 m/min cutting speed and 0.06, 0.12, and 0.18 mm/rev feed rates. The predictions were done by the calibrated material parameters and friction coefficients as previously presented in Chapters 3.1 and 3.2. The comparisons with the experimental values can be found in Figure 3.19. As can be seen from the results satisfactory agreement is observed. The maximum and average discrepancies are 29% and 12%.

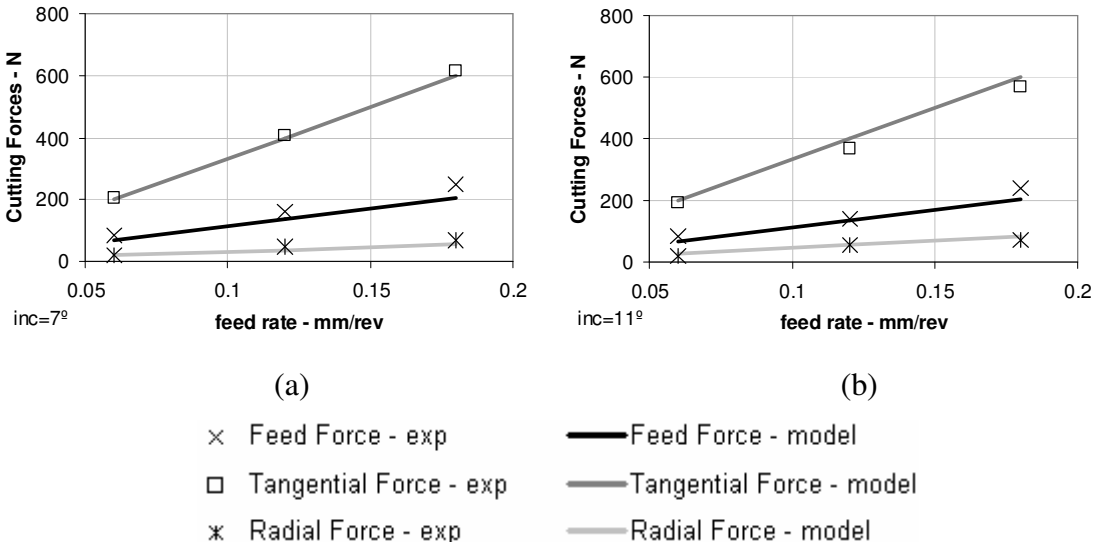

Figure 3.19: Comparison of the oblique cutting forces predicted by the model and the experimental values for Ti6Al4V alloy with HSS cutting tool with inclination angles of (a) 7º, and (b) 11º.

3.6. Chip Flow Angle Predictions

The tests conducted for oblique cutting model verifications are also used to measure the chip flow angles. For the measurement video shot is taken during the cutting experiments with a camera which is placed parallel to the rake face. Then the chip flow angle is measured from the screenshots captured from the camera. The chip flow angles are also predicted by the proposed model in Chapter 2.2.4. The results can be seen in

Figure 3.20. Over all the agreement is found to be satisfactory. The maximum and average discrepancies are 25% and 9% respectively.

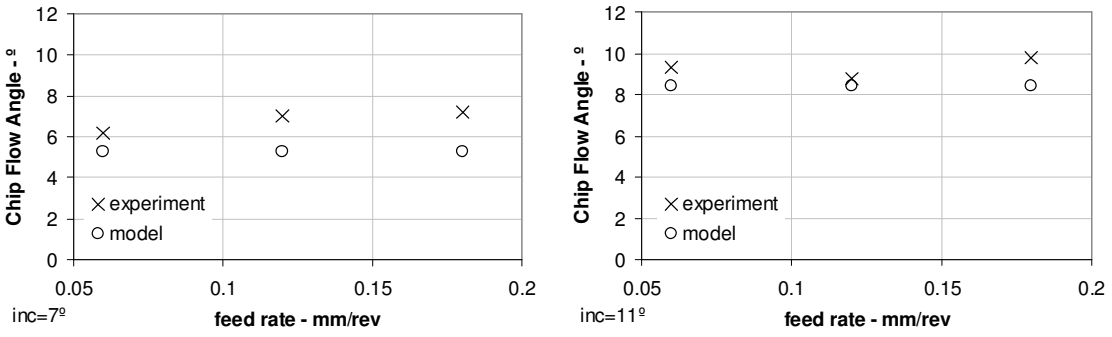

(a) (b)

Figure 3.20: Comparison of chip flow angle by the proposed model and experiments for Ti6Al4V alloy with HSS cutting tools having inclination angles of (a) 7º, and (b) 11º.

3.7. Further Discussions on the Contact Lengths and Friction Coefficient

The identification of sliding friction provides an important input for the analysis of the cutting process as discussed in the previous section. However, for the through analysis of the cutting process, one needs to analyze the apparent friction coefficient as well. The length of the sticking contact region on the rake face is one of the key parameters that determine the value of the apparent friction coefficient. Observing equations (2.12) and (2.19), it can be deduced that the sticking contact length is a function of the feed rate (uncut chip thickness), shear stress at the exit of the primary shear band, the pressure distribution on the rake face, the rake and shear angles, and the apparent and sliding friction coefficients. As the relationship between the sticking length and the feed rate is linear, the increase in the feed rate directly affects the length of the contact. This was also verified experimentally in Chapter 3.4. The effect of the cutting velocity, on the other hand, is indirect, but can be predicted using the process model, and can also be observed experimentally. Equation (2.12) shows that the sticking length depends on the sliding friction coefficient and the ratio τ_1 / P_0 which are both affected by the cutting speed. In general, higher cutting speeds result in reduced sliding friction coefficients, and thus shorter sticking lengths. For instance, the sliding friction coefficient values of AISI 1050 steel with coated carbide tool (see Figure 3.3.b) decreases with the increasing friction speeds. Therefore, one should expect shorter sticking contact lengths at high cutting speeds.

Another observation on the friction behavior in metal cutting is the relationship between the sticking and sliding friction coefficients. As discussed in Chapter 2.1.4 the apparent friction coefficient is always smaller than the sliding friction coefficient. For instance for a constant total contact length and sliding friction coefficient (0.4 in this case), the variation of the ratio of the apparent and the sliding friction coefficient with the increasing sticking contact length can be obtained by equations (2.27) and (2.28) in which is also shown in Figure 3.21. As expected, when there is only sliding friction region present, i.e. at high cutting speeds (ℓ_p / ℓ_c=0), the value of the sliding and apparent friction coefficients are equal to each other. On the other hand as the length of the sticking region increases, it results in lower apparent friction values than the sliding friction coefficient.

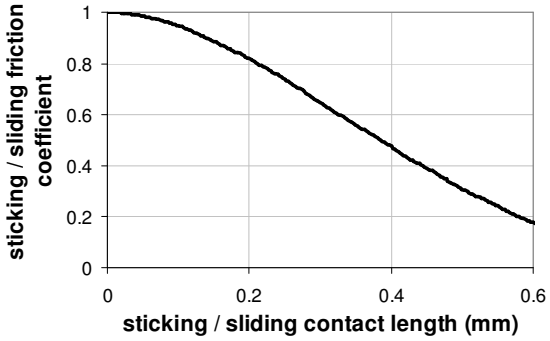

Figure 3.21: The variation of the apparent friction coefficient with the sticking contact length for a constant total contact length.

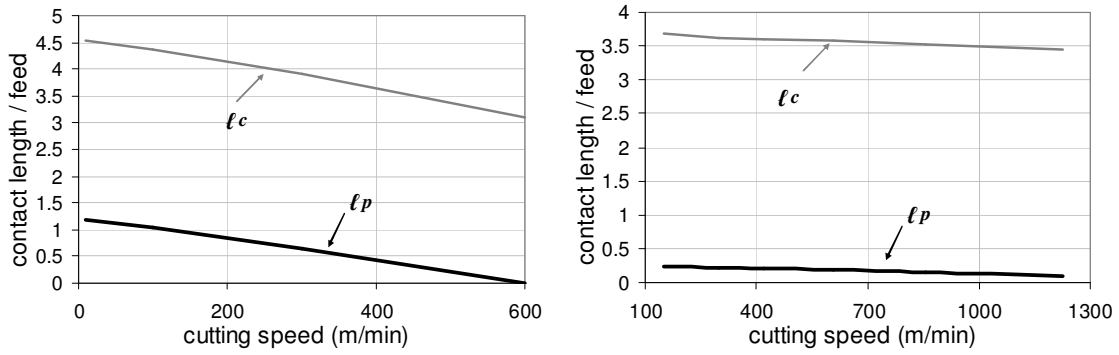

(a) (b)

Figure 3.22: The predicted variation of the ratio of the contact length and feed for AISI 1050 steel with (a) coated carbide and (b) CBN cutting tools.

For further analysis of contact lengths, cutting experiments and simulations are conducted on the AISI 1050 steel with coated carbide and CBN cutting tools. The

simulation results can be seen in Figure 3.22. The length of the sticking region decreases by increasing cutting speed for each cutting tool as shown in Figure 3.22. Especially for the coated carbide tool, the sticking zone vanishes, i.e. fully sliding contact, at the cutting speed of 600 m/min. For the CBN tool on the other hand, fully sliding conditions are found to be present at cutting speeds higher than 1250 m/min as shown in Figure 3.22.b. In order to verify this behavior, the contact lengths for coated

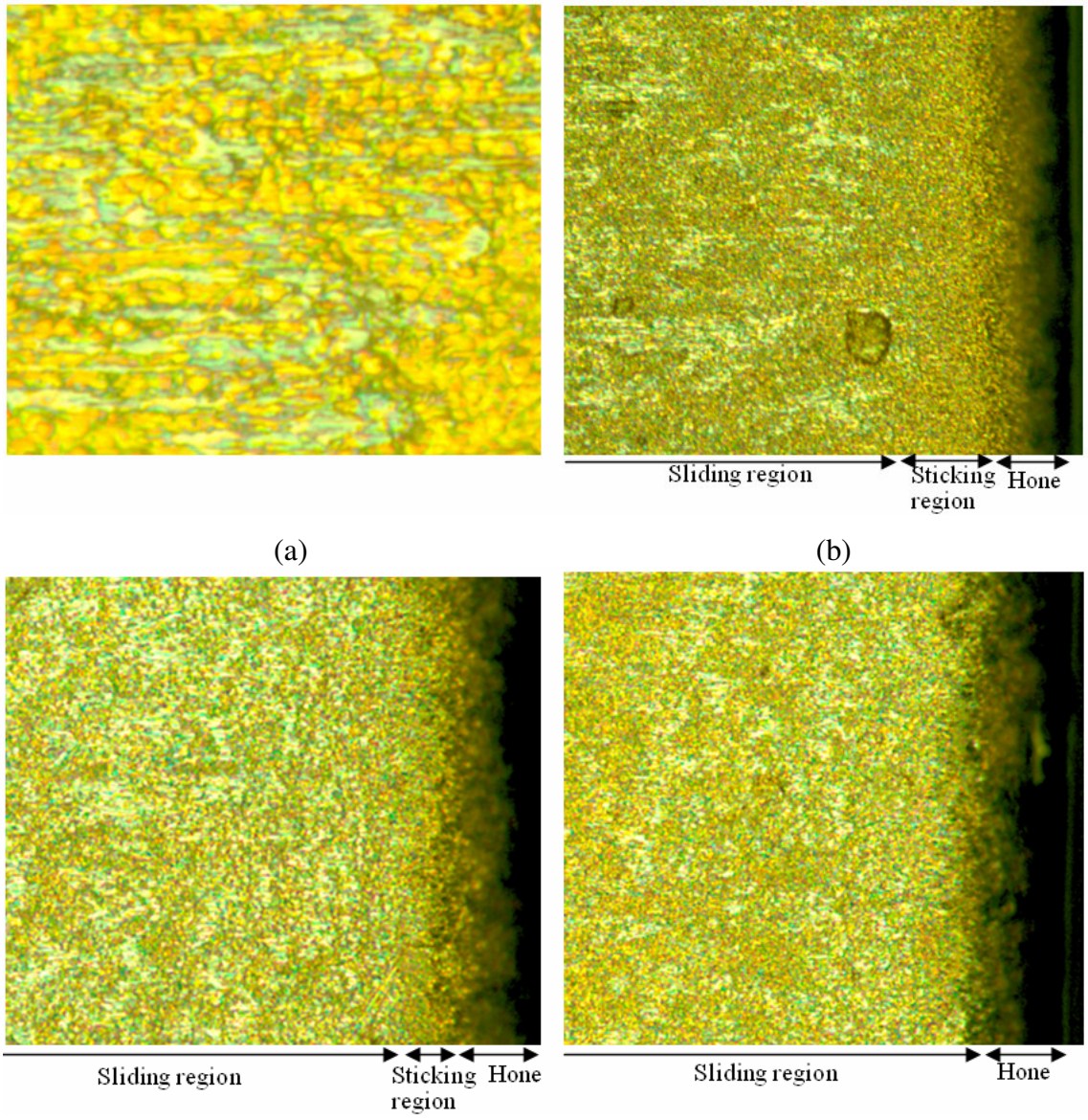

(a) (b)

(c) (d)

Figure 3.23: (a) The sliding marks at 500 magnification, and rake face view of the tests at 200 magnification with feed rate of 0.3 mm/rev and cutting speeds of (b) 100 m/min, (c) 300 m/min, and (d) 600 m/min.

carbide tool were measured by using a microscope. Using optical methods is a simple and efficient way to characterize the contact length. In the microscope measurements,

the sliding marks can be seen very clearly as shown in Figure 3.23.a. The regions close to the tool tip where the sliding marks do not exist are the sticking region. The images taken from the microscope measurements at cutting speeds of 10 m/min, 300 m/min and 600 m/min can be seen in Figure 3.23. As can be observed from the Figure 3.23.b and Figure 3.23.c, the length of the sticking zone at 100 m/min is longer than the sticking zone length at cutting speed of 300 m/min. Figure 3.23.d. indicates no evidence of sticking region at cutting speed of 600 m/min. Therefore, the measurements verify the contact length predictions of the model.

3.8. The effect of the Friction Model on Cutting Force Predictions

In this section, the effect of the friction modeling on the prediction of the cutting forces is discussed. Three different friction models, of which two are listed in Table 3.7, are selected for comparative analysis. The first friction model involves the sticking and sliding contact regions on the rake face as defined by equation (2.8), which is used in all of the analysis throughout the study. The second model assumes that the friction on the rake face only consists of sliding friction. The last model, on the contrary, assumes that the friction state on the rake face is in sticking conditions.

Table 3.7: The friction models that are used in the comparative analysis for the prediction of the cutting forces.

Model	Shear Stress distribution on the rake face
Only sliding	$\tau = \mu P \qquad 0 \le x \le \ell_c$
Only sticking	$\tau = \tau_1 \qquad 0 \le x \le \ell_c$

In order to compare the cutting force predictions orthogonal cutting tests are conducted using AISI 1050 steel and coated carbide cutting tool. The proposed model which is discussed in Chapter 2.1, is applied. The cutting force predictions are done by using the three different friction models of which two are listed in Table 3.7, and the results are given in Figure 3.24 in terms of the error between the model predictions and the experiment results.

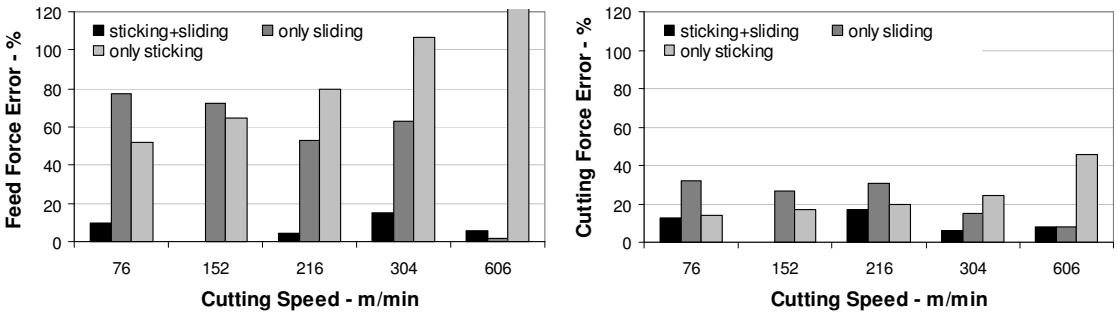

Figure 3.24: The (a) feed force and (b) cutting force errors between the predictions using the different friction models and experimental results for AISI 1050 steel and coated carbide tool.

As can be observed from Figure 3.24.a, the prediction error in complete sliding friction assumption case, decreases drastically with the increasing cutting speed. As also discussed in Chapter 3.7, at 600 m/min cutting speed the friction state is found to be fully sliding considering the length of the sticking region length (see Figure 3.22.a. and Figure 3.23.d). Supporting this observation, at cutting speed of 606 m/min, the predictions are very close to the experimental measurements. Therefore, it is an expected result that the model which assumes only sliding friction on the rake face yields better predictions at high cutting speeds. On the contrary, when complete sticking on the rake face is assumed the prediction error becomes higher as the cutting speed increases. The error at slow cutting speeds is lower (Figure 3.24.a.) indicating longer sticking zone at those speeds as shown in Figure 3.22 and Figure 3.23 as well. However, even at slow speeds the prediction error is quite high which suggests that the rake contact cannot be modeled accurately using sticking only. This can also be seen clearly in Figure 3.22 that the sliding zone always exists even at slow cutting speeds. On the other hand, the friction model which considers both sticking and sliding regions provides very close predictions to the experimental measurements since it represents the true friction behavior in cutting operations. As can be seen from Figure 3.24, the prediction error for the cutting (tangential) force is drastically lower than that for the feed force when fully sliding or fully sticking conditions are assumed in friction modeling. Similar results are also observed in the FE cutting process simulations [82]. This is due to the fact that the cutting force mainly depends on the material behavior in the primary shear zone whereas the feed force depends more on the friction behavior on the rake face. Thus, unrealistic modeling of the friction behavior affects the accuracy of feed force predictions strongly.

3.9. Further Discussions on the JC Material Model

As mentioned in Chapter 3.2, the two critical inputs required by the model are the material parameters and the friction coefficient. An approach to obtain the friction coefficient is proposed and verified by the experiments in the aforementioned analysis. The selection of JC parameters is another important issue. Although the calibrated JC parameters are shown to yield accurate results, we would still like to discuss on the calibration procedure. The JC parameters to be used in the cutting force modeling are obtained using a non-linear regression analysis. Due to the high sensitivity of the non-linear regression analysis to the initial and the tolerance values used in the iterations, the number of parameters to be determined should be reduced. If all the parameters of the Johnson Cook model are to be determined, the final values may turn out to be impractical. For instance, B may become a negative number which is impossible. In order to solve this problem, we set the parameters B, n, m and ν as in Table 3.1, and solve for the parameter A which minimizes the error between the predicted and measured shear stresses. These results are called as set 1. On the other hand, widely used JC parameters for AISI 1045 steel from Jaspers et al. [90] obtained from Split Hopkinson Bar Tests are used for comparison which is called as set 2. Also, in order to update the Johnson-Cook parameters that Jaspers et al. [90] obtained, we again conduct non-linear regression analysis but this time by setting the A, B, n, and ν from Jaspers et al. [90], and solve for the value of m which is called as set 3. The purpose in this update is to eliminate the error due to the strain rate difference between the non-cutting and cutting tests, because the maximum strain rate that Jaspers et al. [90] used was 7.5×10^3 s^{-1}. These set of parameters can be seen in Table 3.8. The comparison of different material model parameters is made in terms of the cutting forces. The results can be found in Figure 3.25 for the tests conducted at 216 m/min cutting speed for different feed rates and two different rake angles.

Table 3.8: The different Johnson-Cook parameters for AISI 1050 steel used for the comparison analysis.

Set	A(MPa)	B(MPa)	n	m	ν
1	880	500	0.234	0.0134	1
2	553	600	0.234	0.0134	1
3	553	600	0.234	0.0448	1

As can be observed from the comparisons, the Johnson-Cook parameters that are obtained from Split Hopkinson Pressure Bar tests (set 2) gives very inaccurate results compared with the calibrated ones, i.e. set 1 and 3. This is a clear indication of using preset values of JC model may sometimes yield inaccurate predictions. Thus, it is important to check the material parameters for different ranges of cutting conditions than the calibration range. Accurate results can be obtained by calibrating the material model using the cutting data. On the other hand, comparing the results obtained from set 1 and set 3 which are calibrated by the proposed model, one can deduce that they both provide good results although set 3 gives worse results for the out of calibration range test, i.e. for -5º rake angle. This is an important outcome as it shows that different Johnson Cook parameter values may yield similar results. The results presented in this section may also be an indication of the fact that the Johnson-Cook constitutive law may not be the best representation of the material behavior for metal cutting operations.

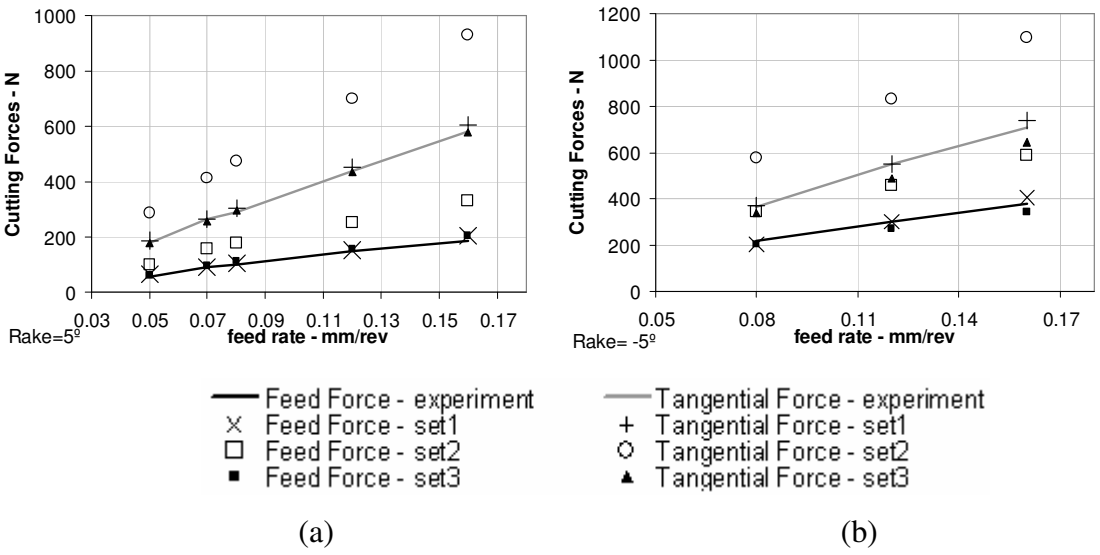

(a) (b)

Figure 3.25: Comparison of cutting forces with different Johnson-Cook Parameters for the cutting tests conducted at 216 m/min with the tools having (a) 5º rake angle and (b) -5º rake angle.

4. INTRODUCTION OF AN APPROACH FOR THE MODELING OF THE EDGE FORCES IN ORTHOGONAL CUTTING

The proposed models in Chapter 2 only consider the primary and the secondary deformation zones which are responsible for the chip formation with the assumption that the cutting tool has no hone radius. The hone radius (see Figure 4.1) on cutting tools affects the deformation in two ways. Firstly the contact at the rake face is no longer a straight path aligned with the rake face, but a curved path. Secondly, it results in another deformation zone which is due to the ploughing and the clearance contact due to the clearance angle γ, Figure 4.1.

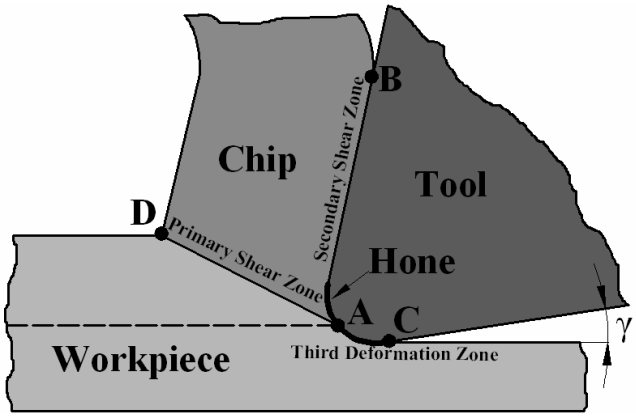

Figure 4.1: The hone and the deformation zones in orthogonal cutting.

4.1. The Modeling Approach

In Figure 4.1, the deformation zones in orthogonal cutting are presented. The primary shear zone (AD), and the secondary shear zone (AB) are responsible for the chip formation where, hone radius below point A (AC) is responsible for the ploughing and the clearance contact. In the model it is assumed that point A is a stagnation point where the material just above it moves upwards contributing to the chip formation. The material just below point A moves downwards and continues contact with the path AC.

Although the model proposed here can be used with any primary shear zone model, again the approach used by Molinari et.al [21] is selected. The contact zones, on the other hand, are divided into several regions as can be seen in Figure 4.2. The division is made so that the minimum number of regions is used. This is due to the simplification in the derivation and faster solution times.

The region (AB) (see Figure 4.1) which is responsible for the contact between the chip and the tool is divided into three regions, Figure 4.2. It should be noted here that, due to the hone radius, the rake contact is not a straight line anymore but a straight line plus a curved path. Because of this, the direction of the normal and friction forces on the rake contact is varying along each region but not region 1 as it is a straight path. That's why, the straight rake contact is defined as region 1. Although region 2 and 3 can be merged and acted as one region, for the simplification in the mathematical representation they are taken as two different regions.

The path (AC) (see Figure 4.1), on the other hand, divided into two regions, Figure 4.2. Region 4 is the region responsible for the material having plastic deformation before entering the region 5 which is responsible for the flank contact.

The detailed formulations regarding Regions 1, 2, 3, and 4 will be given in the next sections. Basically, the proposed approach does not model the material deformation in front of the hone radius directly, but it assumes the pressure and shear stress distributions at the contact between the tool and the workpiece on path AC. On the other hand, the true analysis of Region 5 needs the knowledge of deformation zone in front the hone radius. That's why, Region 5, which is due to the clearance contact, will be discussed separately from the others.

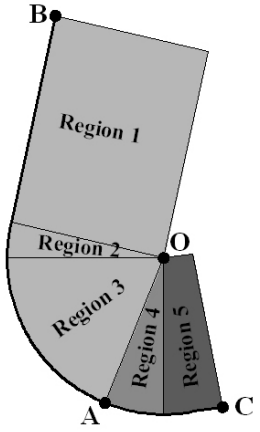

Figure 4.2: The divided regions used in edge force modeling.

4.2. The Stagnation Point, Normal Pressure and Shear Stress Distributions

The stagnation point position is one of the key parameters in defining the regions. The stagnation is assumed to occur at point A where the line connecting it to the center of the hone has θ_s degrees with the vertical axis (see Figure 4.3). From the previous studies [40, 41] it is shown that θ_s for metals is around 25º-30º. However, for the cases where shear angle is bigger than θ_s, there is geometrical conflict between the hone radius and shear band. For instance, observing Figure 4.3, one can see that a line beginning from point A (the shear band) will always have a conflict with the hone if its angle with the horizontal axis is greater than θ_s. In order to avoid the conflict, the minimum value of the θ_s must be equal to the shear angle. For this reason, θ_s is assumed to be equal to the shear angle in this study i.e. $\phi = \theta_s$.

In order to present the normal pressure and shear stress distributions more clearly the lengths that are defined Figure 4.3 are used. First of all it should be mentioned that, the real length of the total contact is defined in equation (4.4). However during microscopic measurements the visible total contact length ℓ'_c (Figure 4.3) is different which is defined in equation (4.5).

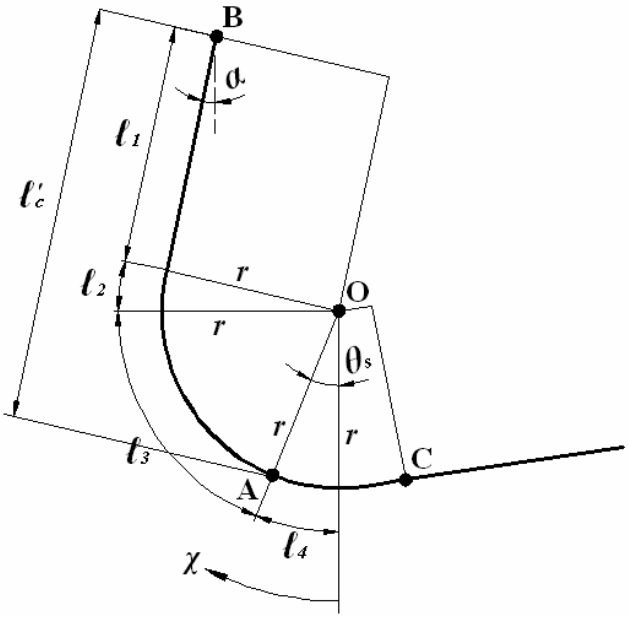

Figure 4.3: The location of the stagnation point and the contact lengths, on the rake and hone

$$\ell_4 = r\theta_s \tag{4.1}$$

$$\ell_3 = r\left(\frac{\pi}{2} - \theta_s\right) \tag{4.2}$$

$$\ell_2 = r\alpha \tag{4.3}$$

$$\ell_c = \ell_3 + \ell_2 + \ell_1 \tag{4.4}$$

$$\ell_c' = \ell_1 + r\cos(\theta_s - \alpha) \tag{4.5}$$

Similar to the model proposed in Chapter 2, the contact at the rake (regions 1,2 and 3) is divided into two zones, namely, sticking and sliding friction regions. Also the normal pressure distribution on these regions (1, 2, and 3) is selected in the form of a function as in equation (4.6). As for the 4th region, since there is no presented study in the literature, and no known way of measuring it we assumed that due to the normal high pressure at that region the friction conditions is sticking. Also the normal pressure selected as a constant value equal to the P_0, in order to maintain the continuity of the distribution. Therefore, normal pressure distribution on the regions are selected as in Figure 4.4 and defined as follows:

$$\begin{aligned} P(\chi) &= P_0 && 0 \le \chi \le \ell_4 \\ P(\chi) &= P_0\left(1 - \frac{\chi}{\ell_c}\right)^{\zeta} && \ell_4 \le \chi \le \ell_c \end{aligned} \tag{4.6}$$

It should be mentioned here that the stress distribution exponent ζ is selected as 3 as it is verified by contact length measurements in Chapter 3.4. Due to the discussions above, the shear stress distribution is defined as follows:

$$\begin{aligned} \tau &= \tau_1 && 0 \le \chi \le \ell_p \\ \tau &= \mu P && \ell_p \le \chi \le \ell_c \end{aligned} \tag{4.7}$$

where, ℓ_p is the sticking contact length.

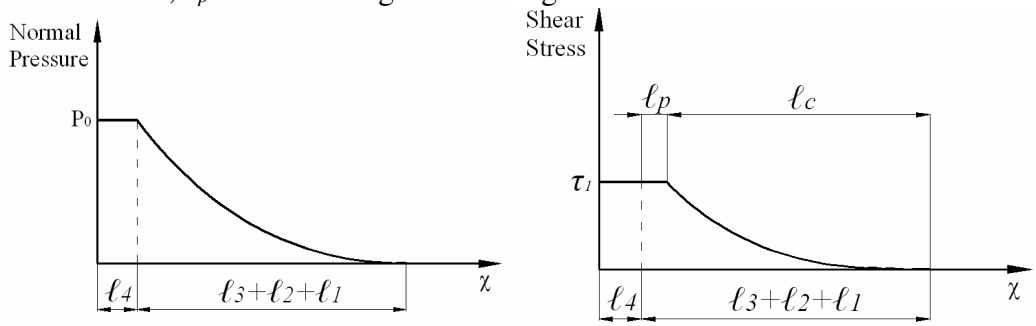

(a) (b)

Figure 4.4: (a) The normal pressure and (b) the shear stress distributions on the contact faces.

4.3. The Forces Acting on the Regions

In this section, the forces acting on each region is derived mathematically in detail. These forces are needed for the calculation of the normal pressure and the contact length as is presented in the next section.

4.3.1. Forces Acting on Region 1

The region 1 is the straight path at the rake face and it is responsible for the chip-tool contact. Since the path in this region is in the form of a line, it is rather simpler, in terms of mathematics, to calculate the normal and friction forces acting on this region.

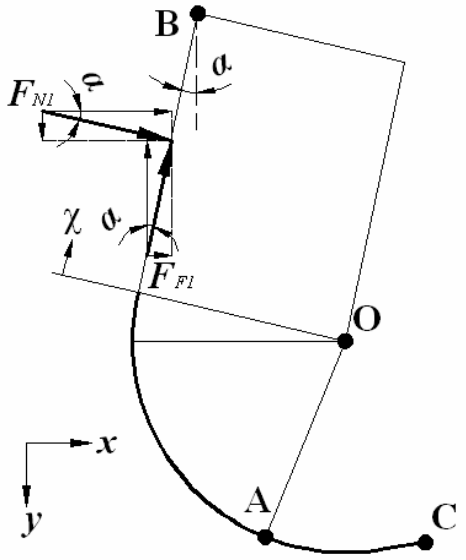

Figure 4.5: Normal and friction forces acting on Region 1.

The normal force acting on Region 1 can be defined as follows:

$$F_{N1} = \int_{\ell_2+\ell_3}^{\ell_c} P_0 w \left(1-\frac{\chi}{\ell_c}\right)^{\zeta} d\chi = \frac{P_0 w \ell_c}{\zeta+1}\left(1-\frac{\ell_2+\ell_3}{\ell_c}\right)^{\zeta+1} \tag{4.8}$$

where, w is the depth of cut. The components of the normal force on the x and y axis can be obtained as follows:

$$F_{N1x} = \frac{P_0 w \ell_c}{\zeta+1}\left(1-\frac{\ell_2+\ell_3}{\ell_c}\right)^{\zeta+1} \cos\alpha \tag{4.9}$$

$$F_{N1y} = \frac{P_0 w \ell_c}{\zeta+1}\left(1-\frac{\ell_2+\ell_3}{\ell_c}\right)^{\zeta+1} \sin\alpha \tag{4.10}$$

For the friction force acting on region 1, there may be two different cases. In the first case the sticking contact length can be calculated to be lower than $\ell_2+\ell_3$, and the friction conditions in this region can only be sliding. Therefore we get,

$$F_{F1}=\int_{\ell_2+\ell_3}^{\ell_c}\mu P_0 w\left(1-\frac{\chi}{\ell_c}\right)^{\zeta}d\chi=\frac{\mu P_0 w\ell_c}{\zeta+1}\left(1-\frac{\ell_2+\ell_3}{\ell_c}\right)^{\zeta+1} \tag{4.11}$$

and the components of the friction force on the *x* and *y* axis are:

$$F_{F1x}=\frac{\mu P_0 w\ell_c}{\zeta+1}\left(1-\frac{\ell_2+\ell_3}{\ell_c}\right)^{\zeta+1}\sin\alpha \tag{4.12}$$

$$F_{F1y}=-\frac{\mu P_0 w\ell_c}{\zeta+1}\left(1-\frac{\ell_2+\ell_3}{\ell_c}\right)^{\zeta+1}\cos\alpha \tag{4.13}$$

In the second case, i.e. if the calculated sticking contact length is higher than $\ell_2+\ell_3$, Region 1 involves a sticking friction region. In this case we get,

$$F_{F1}=\int_{\ell_2+\ell_3}^{\ell_p}\tau_1 w d\chi+\int_{\ell_p}^{\ell_c}\mu P_0 w\left(1-\frac{\chi}{\ell_c}\right)^{\zeta}d\chi=\tau_1 w\left(\ell_p-\ell_2-\ell_3\right)+\frac{\mu P_0 w\ell_c}{\zeta+1}\left(1-\frac{\ell_p}{\ell_c}\right)^{\zeta+1} \tag{4.14}$$

and the components:

$$F_{F1x}=\left[\tau_1 w\left(\ell_c-\ell_2-\ell_3\right)+\frac{\mu P_0 w\ell_c}{\zeta+1}\left(1-\frac{\ell_p}{\ell_c}\right)^{\zeta+1}\right]\sin\alpha \tag{4.15}$$

$$F_{F1y}=-\left[\tau_1 w\left(\ell_c-\ell_2-\ell_3\right)+\frac{\mu P_0 w\ell_c}{\zeta+1}\left(1-\frac{\ell_p}{\ell_c}\right)^{\zeta+1}\right]\cos\alpha \tag{4.16}$$

It should be mentioned here that, the normal force (equations (4.9) and (4.10)) acting on region 1 always contribute to the total forces in the positive direction for the selected base coordinate system, Figure 4.5. However, the *y* component of the friction force (equations (4.13) and (4.16) is always reducing the total forces due to the inverse movement of the chip flow according to the selected coordinate system.

4.3.2. Forces Acting on Region 2

Region 2 is on the hone radius and responsible for the chip-tool contact such as region 1. However, the geometric form of this region is in the form of an arc. That is the

direction of the normal and friction forces changes at each point on this arc, which results in more complicated integral equations to solve.

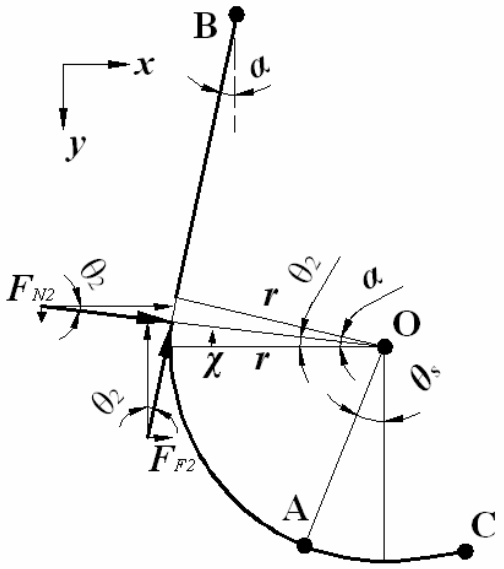

Figure 4.6: Normal and friction forces acting on Region 2.

The angle θ_2 which is varying along the region can be written in terms of χ as follows:

$$\theta_2 = \frac{\chi}{r} - 90 + \theta_s \tag{4.17}$$

Now the component of the normal force acting on Region 2 in the x direction can be obtained by the following integral:

$$F_{N2x} = \int_{\ell_3}^{\ell_2+\ell_3} P_0 w \left(1 - \frac{\chi}{\ell_c}\right)^{\zeta} \cos\left(\frac{\chi}{r} - 90 + \theta_s\right) d\chi \tag{4.18}$$

By using integration by parts for $\zeta=3$, the analytical solution of (4.18) can be calculated as follows:

$$F_{N2x} = P_0 w \left[r\left(1 - \frac{\chi}{\ell_c}\right)^{\zeta} \sin\left(\frac{\chi}{r} - 90 + \theta_s\right) - \frac{\zeta}{\ell_c} r^2 \left(1 - \frac{\chi}{\ell_c}\right)^{\zeta-1} \cos\left(\frac{\chi}{r} - 90 + \theta_s\right) \right.$$

$$\left. - \frac{\zeta(\zeta-1)}{\ell_c^2} r^3 \left(1 - \frac{\chi}{\ell_c}\right)^{\zeta-2} \sin\left(\frac{\chi}{r} - 90 + \theta_s\right) + \frac{\zeta!}{\ell_c^3} r^4 \cos\left(\frac{\chi}{r} - 90 + \theta_s\right) \right]_{\ell_3}^{\ell_2+\ell_3} \tag{4.19}$$

Similarly, the *y* component of the normal force is defined as:

$$F_{N2y} = \int_{\ell_3}^{\ell_2+\ell_3} P_0 w\left(1-\frac{\chi}{\ell_c}\right)^{\zeta} \sin\left(\frac{\chi}{r}-90+\theta_s\right)d\chi \tag{4.20}$$

By using integration by parts (for $\zeta=3$), we obtain:

$$F_{N2y} = P_0 w\left[-r\left(1-\frac{\chi}{\ell_c}\right)^{\zeta}\cos\left(\frac{\chi}{r}-90+\theta_s\right)-\frac{\zeta}{\ell_c}r^2\left(1-\frac{\chi}{\ell_c}\right)^{\zeta-1}\sin\left(\frac{\chi}{r}-90+\theta_s\right)\right.$$
$$\left.+\frac{\zeta(\zeta-1)}{\ell_c^2}r^3\left(1-\frac{\chi}{\ell_c}\right)^{\zeta-2}\cos\left(\frac{\chi}{r}-90+\theta_s\right)+\frac{\zeta!}{\ell_c^3}r^4\sin\left(\frac{\chi}{r}-90+\theta_s\right)\right]_{\ell_3}^{\ell_2+\ell_3} \tag{4.21}$$

For the friction force acting on Region 2, there may be three different cases. In this first case, the friction condition in Region 2 may only be sliding i.e. $\ell_p < \ell_3$. In this case we have:

$$F_{F2x} = \int_{\ell_3}^{\ell_2+\ell_3} \mu P_0 w\left(1-\frac{\chi}{\ell_c}\right)^{\zeta} \sin\left(\frac{\chi}{r}-90+\theta_s\right)d\chi \tag{4.22}$$

$$F_{F2y} = -\int_{\ell_3}^{\ell_2+\ell_3} \mu P_0 w\left(1-\frac{\chi}{\ell_c}\right)^{\zeta} \cos\left(\frac{\chi}{r}-90+\theta_s\right)d\chi \tag{4.23}$$

If the contact condition in Region 2 involves both sliding and sticking friction, i.e $\ell_3 < \ell_p < \ell_2+\ell_3$:

$$F_{F2x} = \int_{\ell_3}^{\ell_p} \tau_1 w \sin\left(\frac{\chi}{r}-90+\theta_s\right)d\chi + \int_{\ell_p}^{\ell_2+\ell_3} \mu P_0\left(1-\frac{\chi}{\ell_c}\right)^{\zeta} \sin\left(\frac{\chi}{r}-90+\theta_s\right)d\chi \tag{4.24}$$

$$F_{F2y} = -\int_{\ell_3}^{\ell_p} \tau_1 w \cos\left(\frac{\chi}{r}-90+\theta_s\right)d\chi - \int_{\ell_p}^{\ell_2+\ell_3} \mu P_0\left(1-\frac{\chi}{\ell_c}\right)^{\zeta} \cos\left(\frac{\chi}{r}-90+\theta_s\right)d\chi \tag{4.25}$$

If the contact conditions in Region#2 involves only sticking friction, i.e. $\ell_2+\ell_3 < \ell_p$:

$$F_{F2x} = \int_{\ell_3}^{\ell_2+\ell_3} \tau_1 w \sin\left(\frac{\chi}{r}-90+\theta_s\right)d\chi = \tau_1 wr(1-\cos\alpha) \tag{4.26}$$

$$F_{F2y} = -\int_{\ell_3}^{\ell_2+\ell_3} \tau_1 w \cos\left(\frac{\chi}{r} - 90 + \theta_s\right) d\chi = -\tau_1 w r \sin\alpha \tag{4.27}$$

Similar to the region 1, the normal force (equations (4.19) and (4.21)) acting on region 2 always contribute to the total forces in the positive direction for the selected base coordinate system, Figure 4.6. However, the *y* component of the friction force (equations (4.23), (4.25) and (4.27)) is always reducing the total forces due to the inverse movement of the chip flow according to the selected coordinate system.

4.3.3. Forces Acting on Region 3

Region 3 is also responsible for the chip-tool contact like the regions 1 and 2. Also, similar to the region 2, this region is on the hone and is formed by an arc. The forces acting on each point on this region has different directions such as in region 2. Although this region can be merged with region 2, it is behaved separately in order to represent the model clearly.

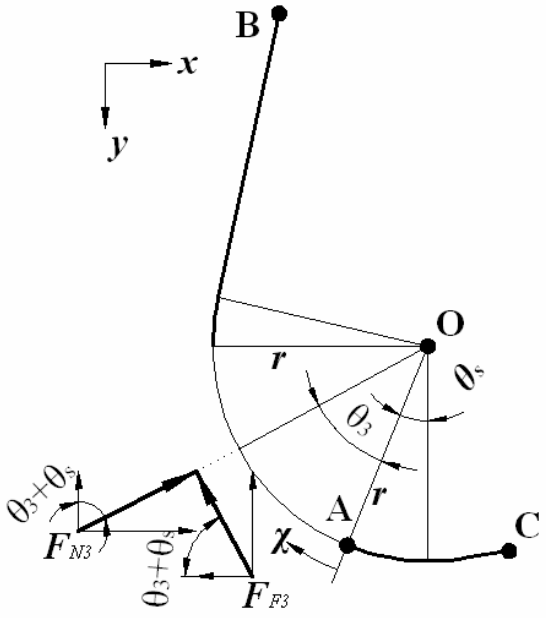

Figure 4.7: Normal and friction forces acting on Region 3.

The positioning angle θ_3 which is varying along Region 3 can be defined in terms of χ as follows:

$$\theta_3 = \frac{\chi}{r} + \theta_s \tag{4.28}$$

The component of the normal force in the x direction can be calculated as:

$$F_{N3x} = \int_0^{\ell_3} P_0 w \left(1 - \frac{\chi}{\ell_c}\right)^{\zeta} \sin\left(\frac{\chi}{r} + \theta_s\right) d\chi \tag{4.29}$$

and in the *y* direction:

$$F_{N3y} = -\int_0^{\ell_3} P_0 w \left(1 - \frac{\chi}{\ell_c}\right)^{\zeta} \cos\left(\frac{\chi}{r} + \theta_s\right) d\chi \tag{4.30}$$

For the friction force, there may be three cases similar to the region 2. If the friction condition in region 3 is only sliding i.e. ℓ_p=0:

$$F_{F3x} = -\int_0^{\ell_3} \mu P_0 w \left(1 - \frac{\chi}{\ell_c}\right)^{\zeta} \cos\left(\frac{\chi}{r} + \theta_s\right) d\chi \tag{4.31}$$

$$F_{F3y} = -\int_0^{\ell_3} \mu P_0 w \left(1 - \frac{\chi}{\ell_c}\right)^{\zeta} \sin\left(\frac{\chi}{r} + \theta_s\right) d\chi \tag{4.32}$$

If the contact conditions in region 3 involve both sliding and sticking friction i.e $\ell_p < \ell_3$:

$$F_{F3x} = -\int_0^{\ell_p} \tau_1 w \cos\left(\frac{\chi}{r} + \theta_s\right) d\chi - \int_{\ell_p}^{\ell_3} \mu P_0 \left(1 - \frac{\chi}{\ell_c}\right)^{\zeta} \cos\left(\frac{\chi}{r} + \theta_s\right) d\chi \tag{4.33}$$

$$F_{F3y} = -\int_0^{\ell_p} \tau_1 w \sin\left(\frac{\chi}{r} + \theta_s\right) d\chi - \int_{\ell_p}^{\ell_3} \mu P_0 \left(1 - \frac{\chi}{\ell_c}\right)^{\zeta} \sin\left(\frac{\chi}{r} + \theta_s\right) d\chi \tag{4.34}$$

If the contact conditions in region 3 involve only sticking friction, i.e. $\ell_3 < \ell_p$:

$$F_{F3x} = -\int_0^{\ell_3} \tau_1 w \cos\left(\frac{\chi}{r} + \theta_s\right) d\chi = -\tau_1 w r \left(1 - \sin\theta_s\right) \tag{4.35}$$

$$F_{F3y} = -\int_0^{\ell_3} \tau_1 w \sin\left(\frac{\chi}{r} + \theta_s\right) d\chi = -\tau_1 w r \cos\theta_s \tag{4.36}$$

As a different behavior than the previous regions, the *y* component of the normal force (equation (4.30) acting on region 3 reduces the total force, Figure 4.7. Similarly, the friction force is always reducing the total forces due to the inverse movement of the chip flow according to the selected coordinate system.

4.3.4. Forces Acting on Region 4

Region 4 has a different condition than the previous regions. The material which doesn't contribute to the chip formation has the first contact with this region. The region has a form of an arc, and again the direction of the normal and friction forces acting on this region is changing along the region.

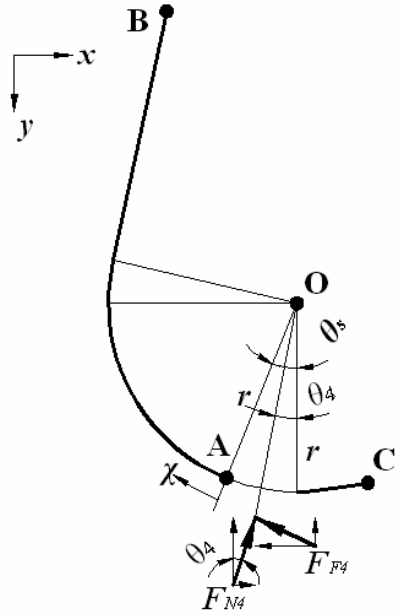

Figure 4.8: Normal and friction forces acting on Region 4

Firstly it should be noted again that region 4 does not contribute to the chip formation but only to the ploughing. Therefore it doesn't have a place in the rake contact analysis. The positioning angle θ_4 can be defined in terms of χ as follows:

$$\theta_4 = \frac{\chi}{r} \tag{4.37}$$

The component of the normal force in the x direction can be calculated as:

$$F_{N4x} = \int_0^{\ell_4} P_0 w \sin\left(\frac{\chi}{r}\right) d\chi = P_0 wr\left(1-\cos\theta_s\right) \tag{4.38}$$

And in the *y* direction:

$$F_{N4y} = -\int_0^{\ell_4} P_0 w \cos\left(\frac{\chi}{r}\right) d\chi = -P_0 wr \sin\theta_s \tag{4.39}$$

The component of the friction force in the x direction can be calculated as:

$$F_{F4x} = -\int_0^{\ell_4} \tau_1 w \cos\left(\frac{\chi}{r}\right) d\chi = -\tau_1 wr \sin\theta_s \tag{4.40}$$

And in the *y* direction:

$$F_{F4y} = -\int_0^{\ell_4} \tau_1 w \sin\left(\frac{\chi}{r}\right) d\chi = -\tau_1 wr\left(1-\cos\theta_s\right) \tag{4.41}$$

4.3.5. The Centroid of the Equivalent Normal Force

For the analysis in the next section, the moment acting around point A from the rake contact will be needed. However, as can be seen from the force analysis, deriving each section's moment around Point A will make the formulation more complex. Therefore, it is proposed here to calculate the centroid of the equivalent normal force, and then to use it in the moment calculations.

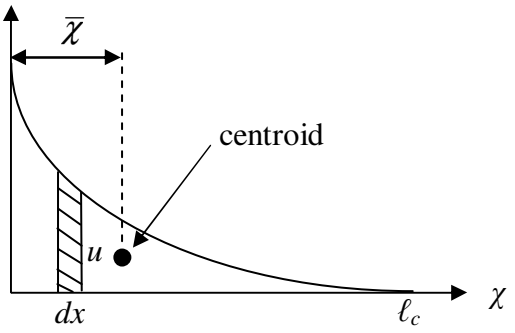

Figure 4.9: Representative the pressure distribution plot for the centroid calculation.

From Figure 4.9, the χ axis component of the centroid can be calculated as follows

$$Q_y = \int_0^{\ell_c} \chi u d\chi = \int_0^{\ell_c} \chi\left(1-\frac{\chi}{\ell_c}\right)^{\zeta} d\chi = \frac{\ell_c^2}{(\zeta+1)(\zeta+2)} \tag{4.42}$$

$$Area = \int_0^{\ell_c}\left(1-\frac{\chi}{\ell_c}\right)^{\zeta} d\chi = \frac{\ell_c}{\zeta+1} \tag{4.43}$$

$$\bar{\chi} = \frac{Q_y}{Area} = \frac{\ell_c}{\zeta+2} \tag{4.44}$$

4.4. The Equivalent Rake Face and the Modified Merchant Circle

When there is no hone radius on the tool, the total normal force acting on the rake face is normal to the rake, and the angle between the total normal force and the horizontal axis equals to the rake angle α (see Figure 2.3.a). Although α is physically an angle on the tool, it also defines the angle between the total normal force N, and the horizontal axis (see Figure 2.3.a). However, it is clear that when there is a hone radius, the direction of the normal force is no more normal to the rake face. In this case there is a need for an equivalent rake face definition.

The component of the total normal force N acting on the face in the x direction N_x can be obtained by equations (4.9), (4.19), and (4.29) as follows:

$$N_x = F_{Nx1} + F_{Nx2} + F_{Nx3} \tag{4.45}$$

And the component of the total normal force N acting on the face in the y direction N_y can be obtained by equations (4.10), (4.21), and (4.30) as follows:

$$N_y = F_{Ny1} + F_{Ny2} + F_{Ny3} \tag{4.46}$$

It is possible to find the angle between the total normal force and the horizontal axis from equations (4.45) and (4.46):

$$c = \tan^{-1}\left(\frac{N_y}{N_x}\right) \tag{4.47}$$

Therefore, it can be stated that the equivalent rake face makes angle with the vertical axis not with rake angle but with angle c (see Figure 4.10). The modified Merchant circle is given in Figure 4.10. As can be seen, the equivalent rake face is represented by the line AB'.

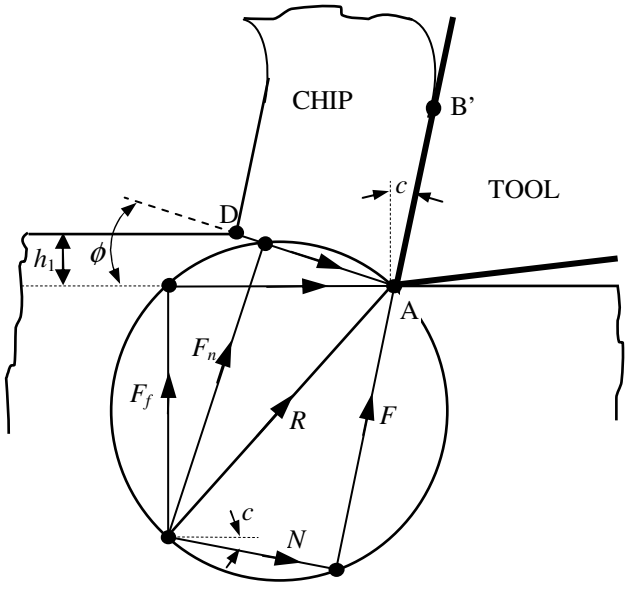

Figure 4.10: The modified Merchant circle and the equivalent rake face AB'.

4.5. Calculation of P_0 and Contact Lengths

As discussed earlier, the shear stress at the exit of the shear band τ_1 is calculated by the primary shear zone model. Therefore, there are three more unknowns in the foregoing analysis, which are P_0, the contact lengths and the sliding and the apparent friction coefficients. In this section, the calculation of P_0 and the contact length is presented.

In equations (4.45) and (4.46) P_0 can be taken into common parenthesis as follows:

$$\begin{aligned} N'_x &= P_0 N_x \\ N'_y &= P_0 N_y \end{aligned} \tag{4.48}$$

The normal force acting on the equivalent rake face can be calculated from equation (4.48) as follows:

$$N = P_0 \sqrt{N'^2_x + N'^2_y} \tag{4.49}$$

On the other hand, the normal force acting on the equivalent rake face can also be written in terms of the shear stress acting on the shear plane as follows (Figure 4.10):

$$N = F_s \frac{\cos \lambda_a}{\cos\left(\phi + \lambda_a - c\right)} \tag{4.50}$$

where λ_a is the friction angle defined by $\lambda_a = \tan^{-1} \mu_a$, where μ_a is the apparent friction coefficient.

Equating equations (4.49) and (4.50), P_0 can be calculated as follows:

$$P_0 = \frac{F_s}{\sqrt{N'^2_x + N'^2_y}} \frac{\cos \lambda_a}{\cos\left(\phi + \lambda_a - c\right)} \tag{4.51}$$

The next step is to calculate the contact length ℓ_c. Assuming that the normal stress is distributed uniformly along the shear plane AD, and considering the momentum equilibrium at the tool tip, we get: $M_{AD} = M_{AB'}$

$$M_{AD} = F_n \frac{AD}{2} = F_s h_1 \frac{\tan\left(\phi + \lambda_a - c\right)}{2 \sin \phi} \tag{4.52}$$

In order to calculate the moment due to normal force acting on the equivalent rake face we have the total normal force from equation (4.49) and the location from equation (4.44), but we need the moment arm M_L. Depending on the calculated value of $\bar{\chi}$ the location of the total normal force can be on the regions 2 and 3, or on the Region 1. The representative sketches of these situations can be seen in Figure 4.11.a, and Figure 4.11.b, respectively. The moment arm can be calculated as follows:

$$M_L = 2r\sin\frac{\bar{\chi}}{2r}\sin\left(\theta_s + \frac{\bar{\chi}}{2r} - c\right) \qquad \bar{\chi} \le \ell_3 + \ell_4 \text{ (Figure 4.11.a)} \qquad (4.53)$$

$$M_L = M_L'\sin\left(\tan^{-1}\left(\frac{\bar{\chi} - \ell_3 - \ell_4}{r}\right) + \alpha - c\right) \qquad \ell_3 + \ell_4 \le \bar{\chi} \text{ (Figure 4.11.b)} \qquad (4.54)$$

where,

$$M_L' = \sqrt{(\bar{\chi} - \ell_3 - \ell_4)^2 + (L)^2 - 2L(\bar{\chi} - \ell_3 - \ell_4)\cos\left(135 + \frac{\theta_s - \alpha}{2}\right)} \qquad (4.55)$$

and

$$L = 2r\sin\left(\frac{90 - \theta_s + \alpha}{2}\right) \qquad (4.56)$$

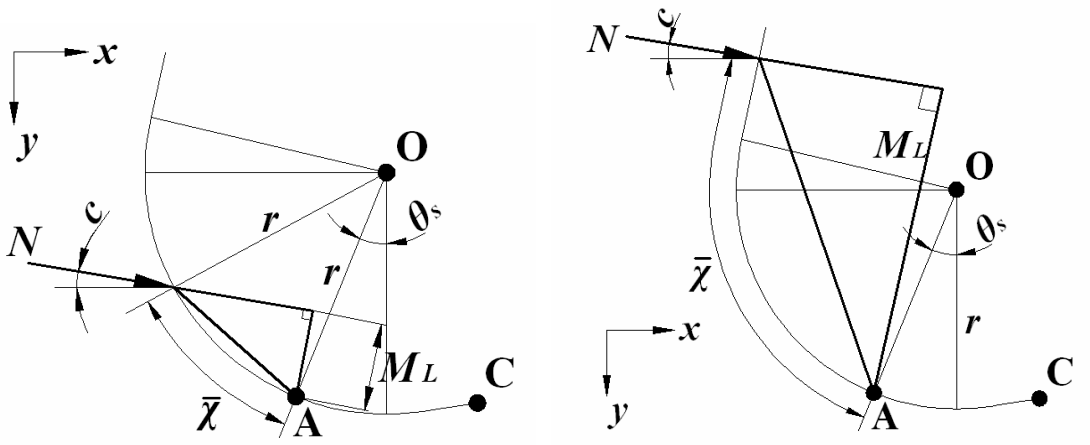

(a) (b)

Figure 4.11: The moment arm when the location of the total normal force is (a) on the hone (Region 2 or 3) and (b) on the Region 1.

Consequently the moment due to the normal force acting on the equivalent rake face can be calculated from equations (4.49), (4.53), and (4.54) as follows:

$$M_{AB'} = NM_L \tag{4.57}$$

It should be mentioned again that equation (4.57) includes total contact length ℓ_c. Therefore equating equations (4.52) and (4.57), an expression for ℓ_c can be obtained implicitly. Also from equations (4.6) and (4.7) the sticking contact length ℓ_p can be calculated as follows:

$$\ell_p = \ell_c \left(-\left(\frac{\tau_1}{P_0 \mu} \right)^{1/\zeta} + 1 \right) \tag{4.58}$$

4.6. Friction Coefficients

As shown in Figure 4.4 the rake contact includes two friction regions, sticking and sliding. Therefore, two different friction coefficients are defined in order to represent this behavior as done in Chapter 2. The apparent friction coefficient μ_a is the result of the total normal and friction forces on the rake face where the sliding friction coefficient μ is due to the normal and friction forces acting on the sliding friction region.

The total friction force on the rake face can be calculated as:

$$F = \sqrt{\left(F_{Fy1} + F_{Fy2} + F_{Fy3}\right)^2 + \left(F_{Fx1} + F_{Fx2} + F_{Fx3}\right)^2} \tag{4.59}$$

Therefore, the apparent friction coefficient can be calculated from equations (4.49) and (4.59) as follows:

$$\mu_a = \frac{F}{N} \tag{4.60}$$

For the sliding friction coefficient, the proposed method in Chapter 2.1.3 is directly used in this model. The calibrated sliding friction coefficients from orthogonal tube cutting tests are used.

4.7. Calculation of Shear Angle and Cutting Forces

Similar to the orthogonal cutting model proposed in Chapter 2. The shear angle ϕ is calculated by minimization of the cutting energy. It is determined by running a simulation program based on the proposed model for a given range of shear angles, and the one that corresponds to the minimum cutting power is selected as the shear angle. Although the primary, secondary and third deformation zones are modeled separately, they are coupled through the shear angle.

As for the cutting forces, once the orientation of the equivalent rake face is calculated, see equation (4.47), the cutting forces can be obtained by the force equilibrium on the chip as follows:

$$\begin{aligned} F_c &= \tau_1 \frac{wh_1}{\sin\phi} \frac{\cos(\lambda_a - c)}{\cos(\phi + \lambda_a - c)} \\ F_f &= \tau_1 \frac{wh_1}{\sin\phi} \frac{\sin(\lambda_a - c)}{\cos(\phi + \lambda_a - c)} \end{aligned} \tag{4.61}$$

where F_f is the feed and F_c is the tangential cutting forces. Note that the cutting forces in equation (4.61) don't include the forces acting on region 4 (equations (4.38-4.41)). Therefore these forces should also be added in order to obtain the total cutting forces.

4.8. Analysis on Region 5

The region 5 is responsible for the workpiece material which doesn't contribute to the chip flow but has a contact with region 4. It is also experimentally observed that the contact between the workpiece material and region 5 continues along this region, which creates a new contact region, which is called the flank contact. The flank contact is due to the elastic recovery of the material which is deformed in front of region 4. As discussed earlier the proposed model doesn't take the deformation areas in the material but assumes the pressure and shear stress distributions at the contact. Therefore, without any further information, the proposed model cannot predict the contact length at the clearance face and thus the cutting forces properly. However, the investigation of adding the effect of this region is still under development. As an initial approach a modified material model which also includes the elastic deformation history of the material will be used. Also the effect of this region on the cutting forces will be evaluated by the help of the experimental results which are discussed in Section 4.10.

4.9. Solution Procedure

In this section the solution procedure for the proposed model is presented. For a given value of shear angle ϕ, and apparent friction coefficient μ_a the shear stress at the exit of the primary shear zone can be calculated by equation (2.2). An iterative procedure is needed in order to calculate the total contact length ℓ_c. As an initial contact length value calculation equation (2.19) is used. With the selected ℓ_c value the location of the equivalent total normal force on the equivalent rake face $\overline{\chi}$ is calculated by the equation (4.44).

Now the normal forces acting on the regions 1,2, and 3 can be calculated by using equations (4.9), (4.10), (4.19), (4.21), (4.29), and (4.30). Then, by using equations (4.45)-(4.47), the orientation of the equivalent rake face *c*, is calculated. Once *c* is obtained P_0 can be calculated by using equation (4.51). By using equations (4.53) or (4.54) depending on the $\overline{\chi}$ value the moment arms are calculated and the condition (4.57) is checked. If the difference between the moment values are in the desired tolerances than the iteration for the total length of cut is stop.

At this point we have the correct c and ℓ_c for the selected values of ϕ, μ_a at the beginning. Therefore we can calculate the chip velocity by:

$$V_{chip} = V \frac{\sin \phi}{\cos(\phi - c)}$$

where V is the cutting speed. Once the chip velocity is obtained, the sliding friction coefficient for the workpiece material can be calculated by the calibrated values in Table 3.5, and the sticking contact length ℓ_p is calculated by equation (4.58). With the calculated value of ℓ_p now we have the knowledge of the friction conditions of the regions 1, 2, and 3. That is, we know which region has sticking or sliding or both friction conditions. Therefore, we can calculate the friction forces at the regions as described in sections 4.3.1-4.3.3. Now we have the total normal and friction forces acting on the rake face (regions 1, 2 and 3). Therefore, the apparent friction coefficient μ_a can be calculated using equation (2.23). If the selected and calculated μ_a values are close to each other within the given tolerances the iteration for μ_a is stopped. This procedure is run for different values of shear angle and the shear angle corresponding to the minimum cutting energy is selected. The cutting forces are calculated by the equation (4.61). Finally, the cutting forces acting on region 4 as described in Chapter 4.3.4 is calculated and added to the total cutting forces.

4.10. The Experimental Verification

Orthogonal tube cutting tests are conducted in order to verify the proposed model. The workpiece material is selected as AISI 1050 steel. P20 Grade TPGN type uncoated carbide tools having 5º rake angle, different hone radii and clearance angle are custom manufactured by a tool company. The hone radius values are 30, and 60 μm and the clearance angles were 3º, 7º, and 11º, which makes a total of 6 different tools. As the process parameters in the cutting experiments constant cutting speed value of 250 m/min is selected, the depth of cut was 2 mm, and the experiments are conducted for different feed rate values of 0.05, 0.1, 0.15, and 0.2 mm/rev. The total cutting forces in the tangential and feed directions are measured by a dynamometer during the experiments.

The simulations are done by the proposed model. The material model parameters that are calibrated before (see Chapter 3.1) are used for AISI 1050 steel. Similarly, the sliding friction coefficient that is calibrated before by the orthogonal tube cutting tests is used (see Chapter 3.1).

The simulation results along with the experimental results can be found in Figures 4.12, 4.13, and 4.14.

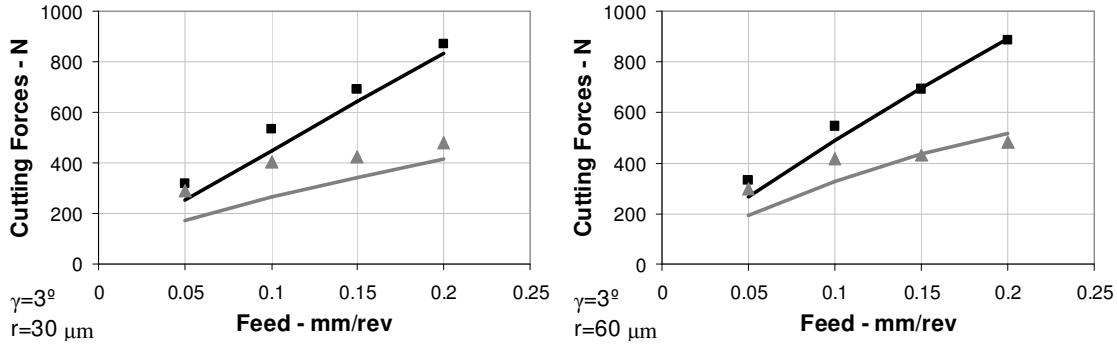

(a) (b)

Figure 4.12: Comparison of the feed (grey) and tangential (black) cutting forces obtained by the proposed model (lines) and measured from the experiments (markers) for insert having 3º clearance angle and hone radii of (a) 30 μm, and (b) 60 μm.

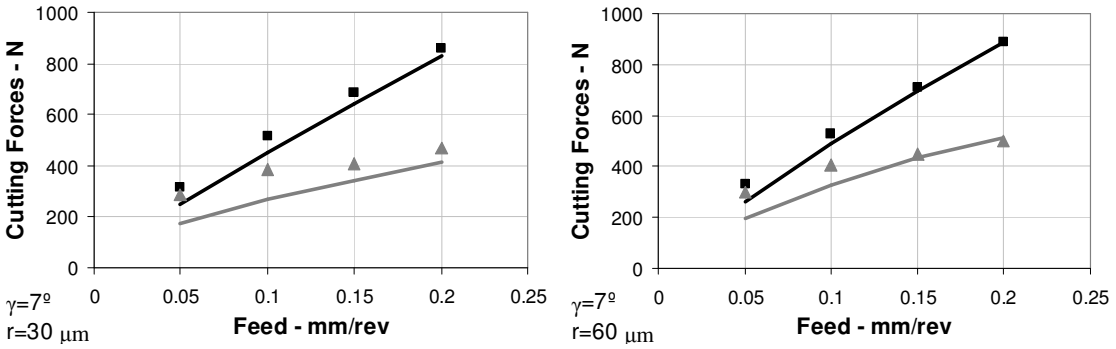

(a) (b)

Figure 4.13: Comparison of the feed (grey) and tangential (black) cutting forces obtained by the proposed model (lines) and measured from the experiments (markers) for insert having 7º clearance angle and hone radii of (a) 30 μm, and (b) 60 μm.

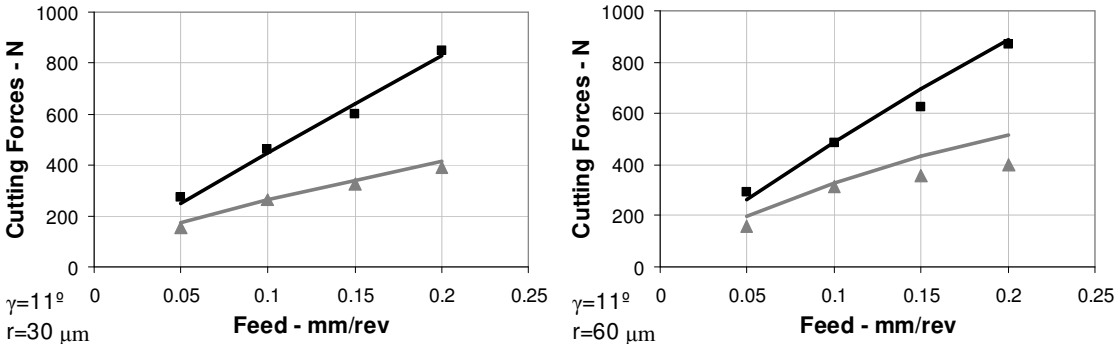

(a) (b)

Figure 4.14: Comparison of the feed (grey) and tangential (black) cutting forces obtained by the proposed model (lines) and measured from the experiments (markers) for insert having 11º clearance angle and hone radii of (a) 30 μm, and (b) 60 μm.

Firstly, it should be mentioned here again that region 5, the flank contact, is not taken into account in the predictions. Thus, some discrepancy between the predicted and measured values is expected. At the first glance in the results (Figures 4.12-4.14) it can be noticed that the error between the predicted and measured values of feed force is higher than the tangential force. This behavior is also experimentally observed in our previous tests. That is, the feed edge forces are always higher than the tangential edge forces. This high error for the feed forces also supports this observation.

Another conclusion from the results is on the correlation between the errors and the clearance angle. As can be observed from (Figures 4.12-4.14), as the clearance angle increases, the error between the predictions and experimental measurements decreases. This behavior is also expected; due to the increase in clearance angle the contact length

at the flank face (region 5) is expected to decrease yielding also a decrease in the forces acting on this region.

As can be deduced from the results as another interesting observation, increase in hone radius doesn't affect the cutting forces very much. For instance, for the tests conducted with the tool having 11º clearance angle, although the hone radius is increased from 30 μm to 60 μm (%100 increase), the feed force increases from 180 N to 200 N (%11 increase) and tangential force from 275 N to 290 N (% 5 increase). It is a well known behavior that the increase in hone radius results in higher forces in cutting due to the higher ploughing. However it is analytically and experimentally shown here that the fraction of increase in the hone radius doesn't directly reflect to the increase in the cutting forces.

5. APPLICATION OF THE PROPOSED MODELS IN COMMON MACHINING OPERATIONS

The proposed process model in Chapter 2 is applied for the two common machining operations: turning and 5 axis milling. The detailed mathematical derivation for the turning process model is presented in Chapter 5.1. The application of the proposed model to 5 axis milling operations is presented in Chapter 5.2.

5.1. Turning Operations

Turning is one of the oldest machining operations. The unwanted material is removed from a rotating workpiece by a cutting tool which is usually called insert. For each revolution of the workpiece (pass) the tool moves along the axis of the workpiece by a given feed with a selected depth of cut (Figure 5.1).

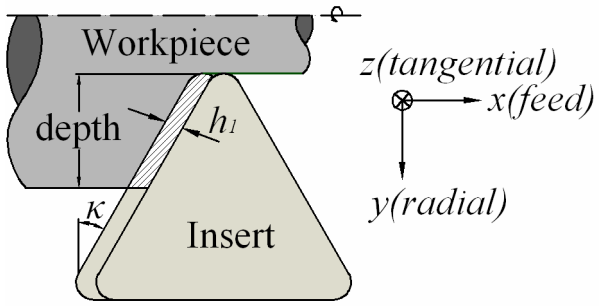

Figure 5.1: Schematic representation of turning.

Basically, there are three main cutting angles on the insert, Figure 5.2. The rake angle α, side edge cutting or approach angle κ, and the inclination angle i which are both measured on the rake face.

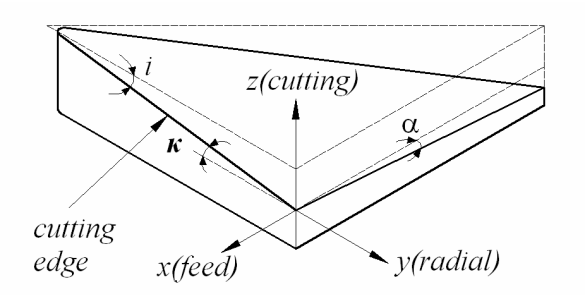

Figure 5.2: The global cutting angles on the insert.

In turning operations existence of the nose radius makes it harder to model than the oblique cutting operations. The nose radius brings two complexities. The first one is that the cutting edge is changing along the nose radius which makes the uncut chip area more complex. Secondly, there exist local cutting angles which are different than the global ones on each point on the nose radius which will be discussed in detail.

5.1.1. Modeling of the Chip Thickness

One of the most important parameter that makes modeling of turning operations harder is the geometry of the uncut chip area. In general, as can be seen in Figure 5.3 the uncut chip area involves two regions where the first region is a parallelogram and the second one is an area which is enclosed by two arcs and a line. However, if the depth of cut w_c is lower than the height of the nose of the insert w_n, then the chip area would only involve the second region.

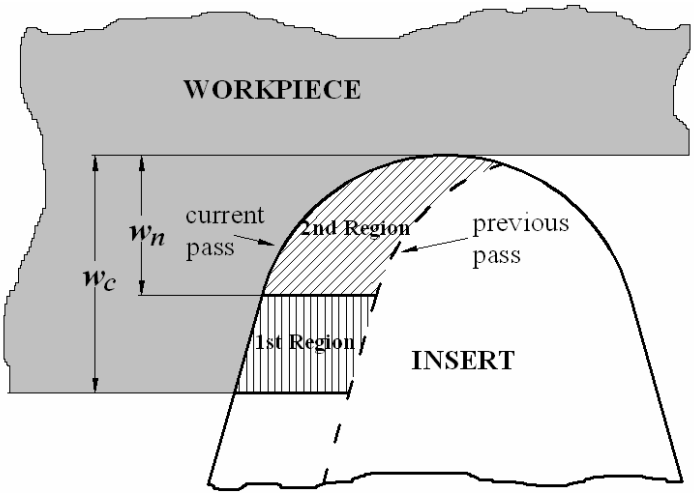

Figure 5.3: The uncut chip area in turning.

In this study we propose to divide the 2nd Region (Figure 5.3), into many parallelogram elements and keep 1st Region as one element as can be seen in Figure 5.4.

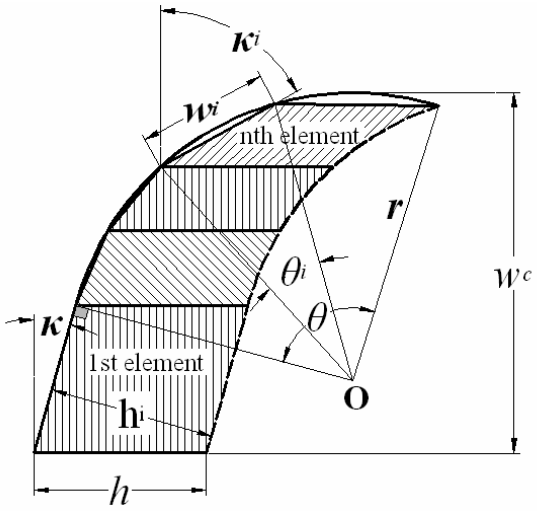

Figure 5.4: The uncut chip area when $w_c > w_n$.

When the depth of cut is higher then the height of the nose radius (Figure 5.4) following are needed in order to define each element:

$$w_n = r - r\sin(\kappa) \tag{5.1}$$

$$\theta = \pi - \kappa - \cos^{-1}(h/2r) \tag{5.2}$$

$$\theta_j = \theta/(n_e - 1) \tag{5.3}$$

$$\kappa_j = \begin{cases} \kappa & j = 1 \\ \kappa_{j-1} + \theta_j/2 & j = 2 \\ \kappa_{j-1} + \theta_j & j > 2 \end{cases} \tag{5.4}$$

$$w_j = \begin{cases} (w_c - w_n)/\cos\kappa & j = 1 \\ 2r\sin(\theta_j/2) & j > 1 \end{cases} \tag{5.5}$$

$$h_j = h\cos(\kappa_j) \tag{5.6}$$

where, r is the insert nose radius, κ and κ_j are the side edge cutting angles for the insert and the j^{th} element, respectively, θ_j is the j^{th} element's angle with the origin of the insert nose, w_j is the length of each element, and h and h_j are the global and each element's uncut chip thickness, respectively.

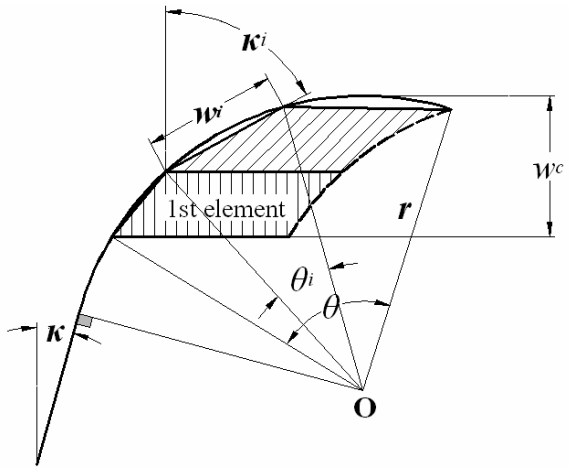

Figure 5.5: The uncut chip area when $w_c<w_n$.

When the depth of cut is smaller than the nose height, i.e. only 2nd Region exists (Figure 5.5), some of the defined angles should be updated as follows:

$$\theta = \pi - \cos^{-1}(h/2r) - \sin^{-1}(\sin(\kappa) + (w_n - w_c)/r) \tag{5.7}$$

$$\theta_j = \theta / n_e \tag{5.8}$$

$$\kappa_j = \sin^{-1}(\sin(\kappa) + (w_n - w_c)/r) + (j - 0.5)\theta_j \tag{5.9}$$

$$w_j = 2r\sin(\theta_j / 2) \tag{5.10}$$

5.1.2. Local Cutting Angles

As briefly discussed above, the existence of the nose radius changes the local cutting angles along the nose radius. Even there exists no inclination angle on the tool, if there is a rake angle, it results in local inclination angles on the nose radius, see Figure 5.6.

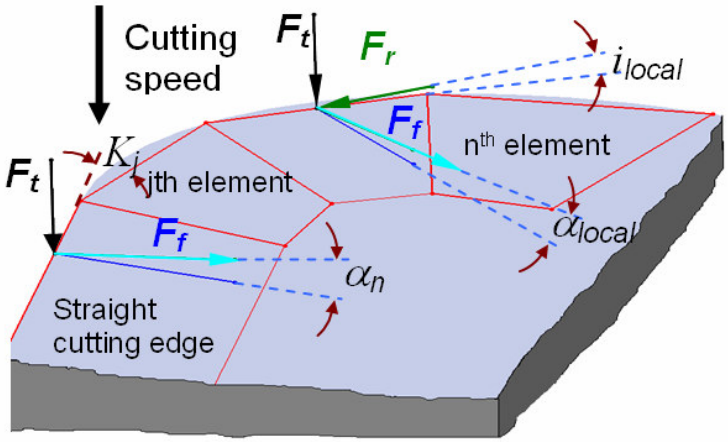

Figure 5.6: 3D representation of the local cutting angles on the insert.

The local normal rake and inclination angle relationships can be derived from the 3D geometrical relationships as follows:

$$\alpha_n^j = 2\sin^{-1}\left(\cos\left(\kappa_j - \kappa\right)\sin\left(\alpha_n / 2\right)\right) + 2\sin^{-1}\left(\sin\left(\kappa_j - \kappa\right)\sin\left(i/2\right)\right) \quad (5.11)$$

$$i^j = 2\sin^{-1}\left(\sin\left(\kappa_j - \kappa\right)\sin\left(\alpha_n / 2\right)\right) - 2\sin^{-1}\left(\cos\left(\kappa_j - \kappa\right)\sin\left(i/2\right)\right) \quad (5.12)$$

where, α_n^j is the local normal rake and i^j is the local inclination angle for the j^{th} element, κ, α_n, and i are the global side edge cutting, normal rake and inclination angles, respectively. It should be noted that for the cases where $w_c > w_n$, the first elements i.e. the straight cutting edge, cutting angles are equal to the global ones:

$$\begin{aligned} \alpha_n^1 &= \alpha_n \\ i^1 &= i \end{aligned} \qquad \text{for } w_c > w_n \quad (5.13)$$

5.1.3. Primary and Secondary Deformation Zone Calculations for the Elements

The proposed oblique cutting model in Chapter 2.2 is applied to the modeling of each element's primary and secondary shear zones. First of all, it is assumed that all the element's shear bands have the same normal shear angle ϕ_n in order to satisfy the continuity of the shear plane. Secondly, the shear stress at the exit of the shear band of each element can be calculated by the modified version of equation (2.36) as follows:

$$\tau_1^j = \rho\left(V\sin\phi_n\cos i^j\right)^2\gamma_1^j + \tau_0^j \quad (5.14)$$

Again with the similar approach we assume that the material exiting from the primary shear zone has a contact with the rake face and a high normal pressure is exerted on the chip so that the friction conditions closer to the tool tip is in sticking conditions. Due to the pressure drop, the friction conditions turn to the sliding along the rake contact. As derived in detail at Chapter 2.2 following can be calculated for each element:

$$P_o^j = \tau_1^j \frac{h_j\left(\zeta+1\right)}{\ell_c^j} \frac{\cos\eta_s\cos\beta_n^j}{\sin\phi_n\cos\eta_c^j\cos\left(\phi_n + \beta_n^j - \alpha_n^j\right)} \quad (5.15)$$

$$\ell_c^j = \frac{h_j\left(\zeta+2\right)}{2} \frac{\sin\left(\phi_n + \beta_n^j - \alpha_n^j\right)}{\sin\phi_n\cos\beta_n^j\cos\eta_c^j} \quad (5.16)$$

$$\ell_p^j = \ell_c^j - \ell_c^j\left(\frac{\tau_1^j}{P_0^j\mu}\right)^{1/\zeta} \quad (5.17)$$

where ℓ_c^j and ℓ_p^j are the total and sticking contact lengths of the j^{th} element, respectively, η_c^j is the chip flow angle (see the chapter 5.1.4 for detailed information), μ

is the sliding friction coefficient, and β_n^j is the normal friction angle which is defined as follows:

$$\beta_n^j = \tan\beta\cos\left(\eta_c^j\right) \tag{5.18}$$

where β is the friction angle which is defined by the relation $\beta = tan^{-1}\mu_a$.

In turning, the relationship between the apparent and the sliding friction coefficient should be calculated differently from the proposed oblique model. Because at each point on the nose radius, due to the varying feed rate, the contact lengths differ which yields to varying normal and friction forces. The apparent friction coefficient is defined as the ration between the total normal and friction forces on the rake face (see equation (2.53)). The total normal force can be written in terms of shear stress at the exit of the shear band for each element, similar to the equation 2.38 as:

$$N = \sum_{j=1}^{n} \tau_1^j \frac{w_j h_j}{\sin\phi_n \cos i^j} \frac{\cos\eta_s \cos\beta_n^j}{\cos\left(\phi_n + \beta_n^j - \alpha_n^j\right)} \tag{5.19}$$

Also, the friction total friction force exerted on the rake face can be written similar to equation (2.52) as:

$$F = \sum_{j=1}^{n} \tau_1^j w_j \left(\ell_p^j + \frac{\ell_c^j - \ell_p^j}{\zeta + 1} \right) \tag{5.20}$$

Therefore, the apparent friction coefficient can be calculated as follows:

$$\mu_a = \frac{\sum_{j=1}^{n_e} \tau_1^j \left(\ell_p^j + \frac{\ell_c^j - \ell_p^j}{\zeta + 1} \right)}{\sum_{j=1}^{n_e} \tau_1^j \frac{h_j}{\sin\phi_n \cos i_j} \frac{\cos\eta_s^j \cos\beta_n^j}{\cos\left(\phi_n + \beta_n^j - \alpha_n^j\right)}} \tag{5.21}$$

5.1.4. Chip Flow Angle, Shear Flow Angle, and the Chip Velocity

Although the orientation and local cutting angles of each element are different, experimentally it is observed that the chip flows in one direction globally, see Figure 5.7. However, since each element has its own coordinate systems (x_j, y_j) defined, there exists a local chip flow angle direction for each element which can be calculated as follows:

$$\eta_c^j = \begin{cases} \eta_c & j = 1 \\ \dfrac{\pi}{2} + \eta_c - \kappa_j - \kappa & j > 1 \end{cases} \tag{5.22}$$

where η_c is the global and η_c are the local chip flow angles.

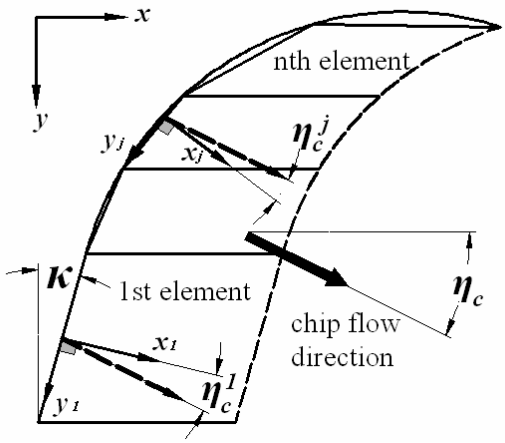

Figure 5.7: Schematic representation of the global and local chip flow angles.

In this study we propose to calculate the global chip flow angle by the energy equilibrium on the chip. The cutting energy E_c, exerted on the chip due to the cutting force can be written as follows:

$$E_c = F_t V \tag{5.23}$$

where F_t is the tangential cutting force, V is the cutting speed. Also, the energy spent at the shear plane and at the rake face can be written as:

$$E_s = F_s V_s + F V_c \tag{5.24}$$

where F_s is the shear force at the shear plane, F is the total friction force at the rake face and can be calculated form equation (5.19), V_s is the shear velocity and V_c is the chip velocity.

From the force equilibrium on the chip, the total shear force can be calculated as:

$$F_s = \sum_{j=1}^{n} \frac{\tau_1^j w_j h_j}{\sin\phi_n \cos i^j} \tag{5.25}$$

Also from the velocity equilibrium we get the shear and chip velocities as follows [32]:

$$V_c = \frac{V \sin\phi_n \cos i'}{\cos(\phi_n - \alpha_n')\cos\eta_c} \tag{5.26}$$

$$V_s = \frac{V \cos i' \cos\alpha_n'}{\cos(\phi_n - \alpha_n')\cos\eta_s} \tag{5.27}$$

One should notice the terms i' and α_n' in equations (5.25) and (5.26). Mentioning once again, each element has its own local rake and inclination angles. However, we

need an equivalent rake α_n', and equivalent inclination i' angles in order to calculate the shear and chip velocities properly. For a given global chip flow angle we can calculate the equivalent angles similar to the equations (5.11) and (5.12) as follows:

$$\alpha_n' = 2\sin^{-1}\left(\cos(\eta_c - \kappa)\sin(\alpha_n / 2)\right) + 2\sin^{-1}\left(\sin(\eta_c - \kappa)\sin(i/2)\right) \tag{5.28}$$

$$i' = 2\sin^{-1}\left(\sin(\eta_c - \kappa)\sin(\alpha_n / 2)\right) - 2\sin^{-1}\left(\cos(\eta_c - \kappa)\sin(i/2)\right) \tag{5.29}$$

Turning back to chip flow angle calculation, it is proposed that there exists one chip flow angle that satisfies E_c=E_s. The chip flow angle that satisfies this equilibrium is selected to be the global chip flow angle.

As for the shear flow angle, since all the material on the shear plane should flow in one direction, we take the same shear flow angle value for each element which can be calculated from equation (2.51) using the equivalent rake and inclination angles as follows:

$$\tan\eta_s = \left(\tan i' \cos(\phi_n - \alpha_n') - \tan\eta_c \sin\phi_n\right)/\cos\alpha_n' \tag{5.30}$$

5.1.5. Normal Shear Angle and Cutting Forces

As discussed earlier the normal shear angle is assumed to be the same for all the elements. It is again proposed here to calculate the shear angle from the minimum energy principle. The solution is run for different values of normal shear angles and the one which corresponds to the minimum cutting energy is selected.

The total cutting forces, on the other hand, can be calculated by the force equilibrium on the chip very similar to the equation (2.56) as follows:

$$\begin{aligned}
F_t &= \sum_{j=1}^{n} \frac{\tau_1^j w_j h_j \left(\cos\left(\beta_n^j - \alpha_n^j\right) + \tan i^j \tan\eta_c^j \sin\beta_n^j\right)}{\sin\phi_n \sqrt{\cos^2\left(\phi_n + \beta_n^j - \alpha_n^j\right) + \tan^2\eta_c^j \sin^2\beta_n^j}} \\
F_f &= \sum_{j=1}^{n} \frac{\tau_1^j w_j h_j \sin\left(\beta_n^j - \alpha_n^j\right)}{\cos i^j \sin\phi_n \sqrt{\cos^2\left(\phi_n + \beta_n^j - \alpha_n^j\right) + \tan^2\eta_c^j \sin^2\beta_n^j}} \\
F_r &= \sum_{j=1}^{n} \frac{\tau_1^j w_j h_j \left(\cos\left(\beta_n^j - \alpha_n^j\right)\tan i^j - \tan\eta_c^j \sin\beta_n^j\right)}{\sin\phi_n \sqrt{\cos^2\left(\phi_n + \beta_n^j - \alpha_n^j\right) + \tan^2\eta_c^j \sin^2\beta_n^j}}
\end{aligned} \tag{5.31}$$

where, F_t is the tangential, F_f is the feed and F_r is the radial cutting forces. As the directions of the total forces, F_t is parallel to the cutting velocity direction, F_f is perpendicular to the plane formed by the cutting velocity or F_t and the cutting edge, and F_r is perpendicular to the other two forces.

5.1.6. Proposed Solution Method

In this section the solution method for the simulation of the turning processes with the proposed model is presented. The solution begins with creating the elements by using equations (5.1)-(5.10). For an initially given value of ϕ_n and η_c the equivalent rake and inclination angles can be calculated by equations (5.28) and (5.29). Then the chip velocity, shear velocity, and the shear flow angle can be calculated by the equations (5.26), (5.27), and (5.30), respectively, also the sliding friction coefficient can be calculated by the calibrated values listed in Table 3.5. An iterative procedure is proposed for the apparent friction coefficient calculation. For an initial value of μ_a, β can be calculated. Now the calculations on each element begin. For each element η_c^j, β_n^j, ℓ_c, ℓ_p, and τ_1^j is calculated by the equations (5.22), (5.18), (5.16), (5.17), and (5.14) respectively, and the total cutting forces can be calculated by the equation (5.31). The apparent friction coefficient can be calculated by the equation (5.21). If the selected and the calculated μ_a is close to each other within the desired tolerance value the iteration stops. Now the energy equilibrium is checked by using equations (5.23) and (5.24). If equation (5.23) is close enough to equation (5.24) the estimated chip flow angle is selected, else the chip flow angle value is changed to run the analysis once again. This whole procedure is run for different values of normal shear angles. The shear angle corresponding to the minimum cutting energy is selected.

5.1.7. Turning Model Verification Experiments

As an initial verification, turning experiments are conducted by using AISI 4340 steel and uncoated carbide tool. The P20 grade TPGN type inserts having 5º rake angle with 0.4 mm nose radius were used. There was no side edge cutting on the insert holder. The tests were conducted at 150 m/min cutting speed, 0.1, 0.15, and 0.2 mm/rev feed rates and 0.2, 0.4, 0.8, and 1.2 mm depth of cuts. The forces in three directions are measured by a dynamometer.

In the simulation the edge forces are also taken into account. The edge force cutting force coefficients for AISI 4340 steel and TPGN type P20 Grade uncoated carbide tool which were obtained from previous tests were used:

$$K_{te} = 80MPa$$
$$K_{fe} = 118MPa \qquad (5.32)$$
$$K_{re} = 22MPa$$

where K_{te}, K_{fe}, and K_{re} are the edge cutting force coefficients in the tangential, feed and radial directions, respectively. The aim of these simulations is to verify the proposed nose radius model. In this respect, the cutting force coefficients are used which are obtained from the proposed model in Chapter 2.

The model predictions along with the experimental results are shown in Figure 5.3, for different verification tests. The depth of cuts in the verification tests are selected so that in one case (see Figure 5.3.a) the depth is smaller than the height of the nose radius. In the second case (see Figure 5.3.b), the depth of cut is equal to the nose radius height. And for the last two cases (see Figure 5.3.c and Figure 5.3.d) the depths of cut were higher than the insert nose radius height. As can be observed from the results, the predicted and measured values are in good agreement.

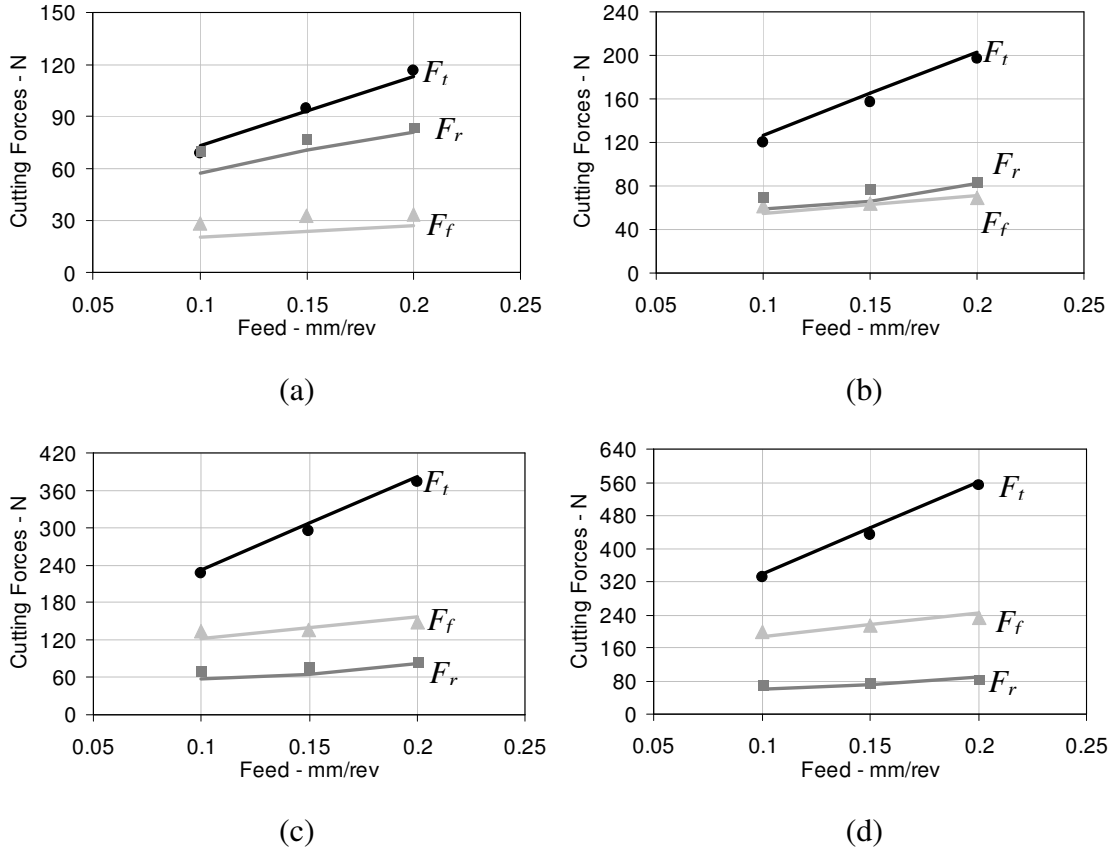

Figure 5.8: The predictions (markers) along with the experimental results (lines) for the depth of cuts of (a) 0.2 mm, (b)0.4 mm, (c) 0.8 mm, and (d) 1.2 mm.

5.2. 5 Axis Milling Operations

In this section the application of the proposed model for the simulation of the cutting forces in 5 axis ball end milling operations is presented. The geometry and kinematics of the 5 axis milling processes are studied before by Ozturk et al. [94]. The model proposed in that study is used here in order to simulate the cutting forces in 5 axis milling. The proposed orthogonal cutting model in Chapter 2, on the other hand, is used to determine cutting force coefficients for the selected tool workpiece couples. The 5 axis milling geometry and force modeling will also be reviewed in the next sections very briefly.

5.2.1.5 Axis Ball End Milling Geometry

There are two complexities in the modeling of 5 axis ball end milling: the geometry of the ball end mill and the additional two degrees of freedom in 5 axis milling.

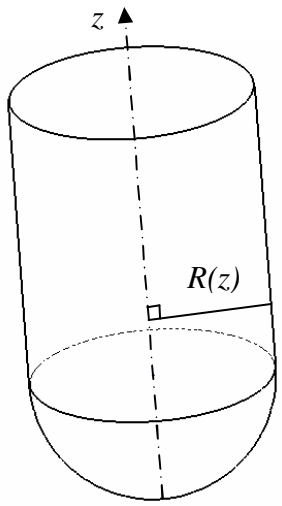

Figure 5.9: 3D representation of a ball end mill.

The 3D geometry of a ball end mill can be seen in Figure 5.9. As can be seen from the geometry the local radius *R(z)* is changing along the ball part of the tool. Due to this situation, the uncut chip thickness and the cutting speed on the ball end region is changing along the *z* axis, which brings the complexity in the modeling.

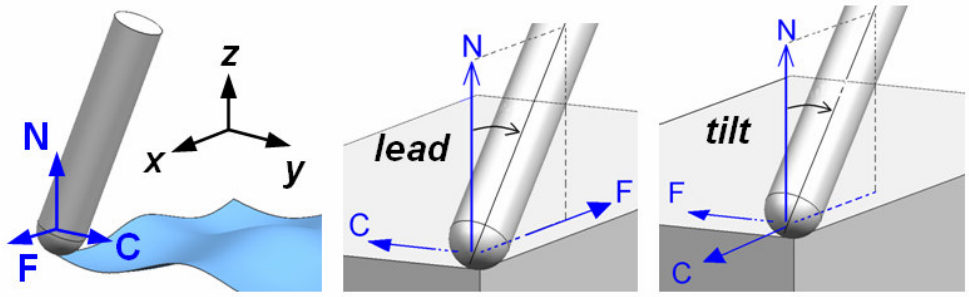

(a) (b) (c)

Figure 5.10: Geometry of 5 axis milling; (a) the tool (F:feed, N:normal, C:cross-feed) and machine (x, y, and z) coordinate systems, and (b) lead, and (c) tilt angles.

The additional angles in 5 axis milling processes, i.e. lead and tilt, can be seen in Figure 5.10. The existence of these angles both makes the uncut chip thickness more complex and changes the engagement of the tool with the workpiece.

5.2.2. Engagement and Force Modeling in 5 Axis Milling

Due to the complexities discussed in the previous section Ozturk et al. [94] proposed to divide the ball-end mill is into differential disc elements having height of dz along tool axis starting from the tool tip. Then, they check the conditions for a disc element geometrically while rotating the tool to see whether it is in cut at that radial and axial position. Once the engagement is found, the uncut chip area dA, and edge length dS corresponding to that element are calculated for the force simulations.

The differential cutting forces for the tooth j in the local cutting coordinates i.e. axial, radial and, tangential, can be written in terms of cutting force coefficients ad follows [94]:

$$\begin{aligned} dF_{rj} &= K_{re}dS + K_{rc}dA \\ dF_{tj} &= K_{te}dS + K_{tc}dA \\ dF_{tj} &= K_{ae}dS + K_{ac}dA \end{aligned} \tag{5.33}$$

where dF_{rj}, dF_{tj}, and dF_{aj} are the differential forces for tooth j in the radial, tangential, and axial directions, respectively, K_{rc}, K_{tc}, and K_{ac} are the cutting force coefficients and K_{re}, K_{te}, and K_{ae} are the edge cutting force coefficients in the radial, tangential, and axial directions, respectively.

The total cutting forces on the tool at the machine coordinates are calculated by integrating the differential forces acting on the oblique elements engaged with the workpiece for each immersion angle, and summing up the contribution of each cutting flute as follows:

$$F_x = \sum_{j=1}^{n} \int dF_{xj}$$

$$F_y = \sum_{j=1}^{n} \int dF_{yj} \tag{5.34}$$

$$F_z = \sum_{j=1}^{n} \int dF_{zj}$$

where n is the total number of tooth on the tool.

It should be noted here that, the proposed model above by Ozturk et al. [94] is verified by several cutting experiments. The cutting force coefficients in equation (5.33) were determined form orthogonal cutting tests. In this study we propose to use the model derived in Chapter 2 in order to calculate those cutting force coefficients.

5.2.3. Verification Experiments

In order to verify the proposed approach above we compare three cases from Ozturk et al.'s [94] study. The material used during the 5 axis milling tests was Ti6Al4V alloy. A 12 mm diameter ball-end mill clamped by a shrink fit tool holder was used in the tests. A dynamometer was used to measure the cutting forces. The process parameters used during verification cases are listed in Table 5.1.

Table 5.1: Cutting parameters for the verification experiments for 5 axis milling.

Case No	Lead (°)	Tilt (°)	Feed (mm/tooth)	Step over (mm)	Cutting type	Depth (mm)	Spindle speed (rpm)
1	10	-15	0.1	-	Slot	1.5	3000
2	15	15		7	Following cut	3	1000
3	0	0		-	Slot	3	500

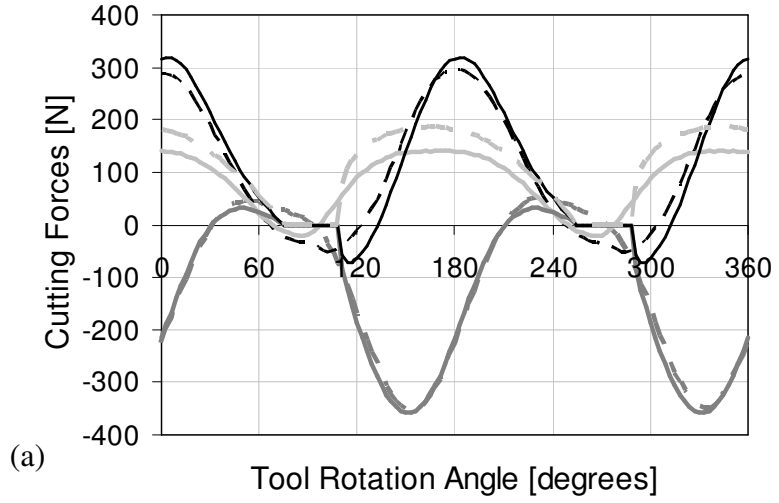

(a)

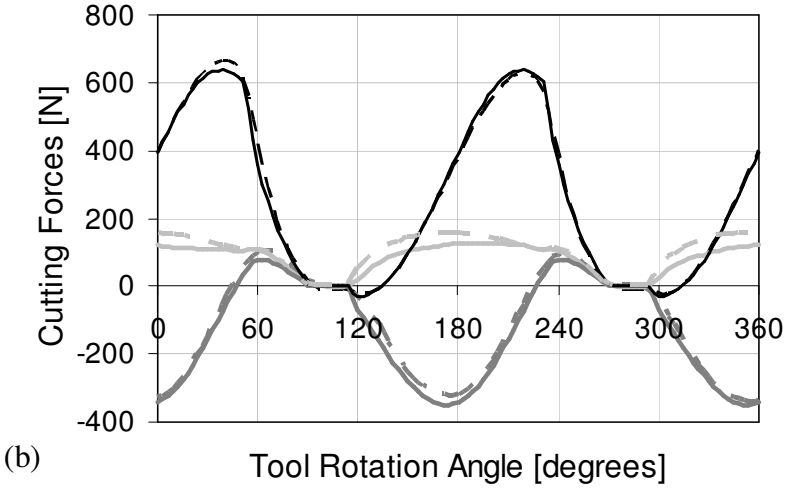

(b)

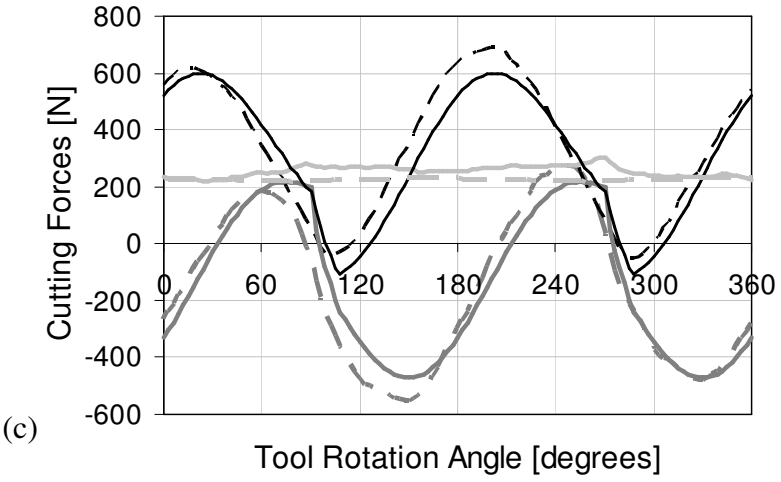

(c)

Figure 5.11: Comparison between the model and the experimental results for the cases listed in Table 5.1, (a) case 1, (b) case 2, and (c) case 3.

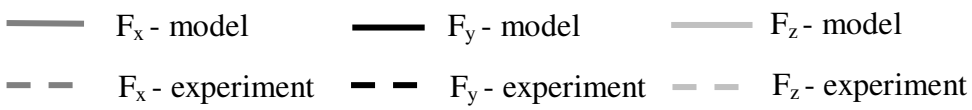

For the simulations by using the proposed model in Chapter 2, the orthogonal database used in order to calculate the cutting force coefficients in equation (5.33) are identified as follows:

$$\beta = 18.13 + 0.0212\alpha + 0.0354V$$
$$\phi = 36.97 + 0.541\alpha - 0.06532V \qquad (5.35)$$
$$\tau = 534.05 - 0.0171V^2 + 1.3821V$$

where ϕ, α and β is are the shear, rake and friction angles, respectively, in degrees, τ is the shear stress in MPa, and V is the cutting speed in m/min. It should be mentioned here that the edge cutting forces are taken from the previously made orthogonal cutting tests.

The simulated and experimental total cutting forces in the machine coordinate system for the cases listed in Table 5.1 can be seen in Figure 5.11. As can be seen there is a good agreement with the predicted and measured results.

6. ANALYTICAL MODELING OF CHATTER STABILITY IN TURNING AND BORING OPERATIONS

The models proposed in the foregoing sections were only considering the mechanics of the cutting processes. Although these models provide much insight about the cutting process, they do not have the ability to predict the dynamic behavior during the cutting process. However, as will be discussed in detail, in the modeling of stability of cutting operations the cutting force coefficients must be known. That is the relationship between the forces and the uncut chip thickness (feed). Therefore, the proposed models in the previous sections can be used to determine the cutting force coefficients as an important input for the stability model.

The stability model presented in this section serves as a base for turning and boring operations. In order to study the stability of these processes, first the dynamic chip thickness and cutting forces are modeled. Then, the multi-dimensional dynamic equations are solved as an eigenvalue problem to obtain the stability limits. This procedure is applied to the turning process with an insert without nose radius in this section. Also, it is used for the boring process in a very similar way in Section 6.5 with the nose radius model proposed in Section 6.3. The basic parameters that identify the turning process are the chip thickness, h, the depth of cut b, and cutting angles which are shown in Figure 6.1, where α is the normal rake angle, and i and κ are the inclination and side edge cutting angles respectively, both measured on the rake face.

6.1. Dynamic Chip Thickness and Forces

In order to formulate a relationship between the dynamic turning forces and the dynamic chip thickness, all components of the dynamic problem are transformed into the global coordinate system (lathe axes; x, y, and z) which can be seen in Figure 6.1.b. From Figure 6.1.a and Figure 6.1.b one can deduce that the dynamic displacements at

the cutting direction (z) do not affect the dynamic chip thickness. By this observation, the dynamic problem is reduced to a 2D model. Therefore, the modulated chip thickness resulting from vibrations of the tool and the workpiece can be expressed as follows:

$$h_m(t) = f\cos\kappa + \left(x_c(t) - x_w(t) - x_c(t-\tau) + x_w(t-\tau)\right)\cos\kappa + \left(-y_c(t) + y_w(t) + y_c(t-\tau) - y_w(t-\tau)\right)\sin\kappa \quad (6.1)$$

where f represents the feed per revolution, $x_c(t)$,$x_w(t)$ and $y_c(t)$, $y_w(t)$ are the cutter and workpiece dynamic displacements for the current pass respectively, and $x_c(t-\tau)$,$x_w(t-\tau)$ and $y_c(t-\tau)$, $y_w(t-\tau)$ are the cutter and workpiece dynamic displacements for the previous pass in x and y directions respectively, and τ is the delay term which is equal to the one spindle revolution period in seconds. The feed term in equation (6.1) represents the static part of the chip thickness. Since the static chip thickness does not contribute to regeneration mechanism, it can be ignored for the purpose of stability analysis. Therefore, the dynamic chip thickness in turning can be defined as follows:

$$h(t) = \Delta x\cos\kappa - \Delta y\sin\kappa \quad (6.2)$$

where:

$$\begin{aligned}\Delta x &= x_c(t) - x_w(t) - x_c(t-\tau) + x_w(t-\tau)\\ \Delta y &= y_c(t) - y_w(t) - y_c(t-\tau) + y_w(t-\tau)\end{aligned} \quad (6.3)$$

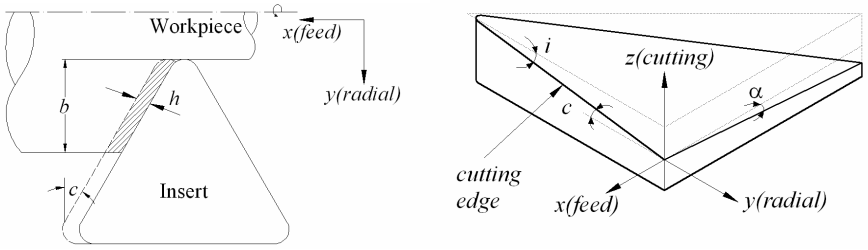

(a) (b)

Figure 6.1: (a) Chip thickness in turning, b) 3D view of the three cutting angles on the insert

Although the dynamic problem can be considered as 2D, the cutting process is 3D in nature, due to the existence of the inclination angle. Then, the forces at the cutting edge need to be modeled by an oblique cutting model [10].The total cutting force acting on the cutting edge is divided into three components: one parallel to the cutting velocity direction F_t, one perpendicular to the plane formed by the cutting velocity or F_t and the cutting edge F_f, and the last one perpendicular to the other two F_r (Figure 6.2).The dynamic cutting forces on the tool can be expressed using equation (6.2) as follows:

$$\begin{Bmatrix} F_f \\ F_r \end{Bmatrix} = \frac{b}{\cos\kappa}\begin{bmatrix} K_f \\ K_r \end{bmatrix}\begin{bmatrix} \cos\kappa & -\sin\kappa \end{bmatrix}\begin{Bmatrix} \Delta x \\ \Delta y \end{Bmatrix} \tag{6.4}$$

where, K_f, and K_r are the corresponding cutting force coefficients. Note that F_t is not included in the formulation as it does not take part in the regeneration mechanism. However, it is affected by the regeneration, and if needed it can be determined using the value of the dynamic chip thickness and the force coefficient in the cutting speed direction K_t. These coefficients can be directly obtained from calibration tests, or by using the method proposed by Armarego et al. [32] and Budak et al. [9]. In the latter approach, the cutting data obtained in orthogonal tests are used to determine the force coefficients using an oblique transformation, and thus include the effects of inclination and rake angles.

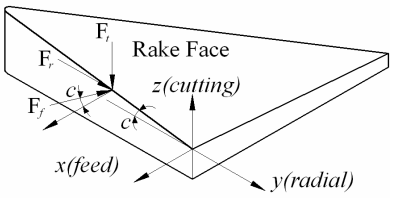

Figure 6.2: Three components of the total cutting force acting on the insert.

By coordinate transformation the cutting forces can be written in the lathe coordinates as follows:

$$\begin{Bmatrix} F_x \\ F_y \end{Bmatrix} = \begin{bmatrix} \cos\kappa & \sin\kappa \\ -\sin\kappa & \cos\kappa \end{bmatrix}\begin{Bmatrix} -F_f \\ F_r \end{Bmatrix} \tag{6.5}$$

where F_x and F_y are the cutting force components in x and y directions, respectively. Substituting equation (6.5) into equation (6.4), the following relationship is obtained:

$$\{F\} = b[A]\{\Delta d\} \tag{6.6}$$

where $\{F\}$is the dynamic force vector and $\{\Delta d\}$ is the dynamic displacement vector both defined in the lathe coordinates. The directional coefficients matrix [A], can be expressed as:

$$[A] = \begin{bmatrix} -\cos\kappa & \sin\kappa \\ \sin\kappa & \cos\kappa \end{bmatrix}\begin{bmatrix} K_f \\ K_r \end{bmatrix}\begin{bmatrix} 1 & -\tan\kappa \end{bmatrix} \tag{6.7}$$

The relationship between the dynamic cutting forces and dynamic chip thickness are now defined by equation (6.6).

6.2. Chatter Stability Limit

For the stability analysis of the dynamic turning process, a procedure is followed that is similar to the one used by Budak and Altintas [67, 73, 97] for the milling stability. The response of the cutter and the workpiece at the chatter frequency, ω_c can be expressed as follows:

$$\{d_j(i\omega_c)\} = [G_j(i\omega_c)]\{F\}e^{i\omega_c t} \qquad j = c, w \qquad d = x, y \tag{6.8}$$

where the transfer function matrix is given as:

$$[G_j] = \begin{bmatrix} G_{j_{xx}} & G_{j_{xy}} \\ G_{j_{yx}} & G_{j_{yy}} \end{bmatrix} \qquad j = c, w \tag{6.9}$$

where G_{jxx} and G_{jyy} are the transfer functions in x and y directions respectively, and G_{jxy} and G_{jyx} are the cross transfer functions. The dynamic displacements in the previous pass at the same location, at time $(t-\tau)$, can be defined as follows:

$$\{d_j^0\} = e^{-i\omega_c\tau}\{d(i\omega_c)\} \qquad j = c, w \qquad d = x, y \tag{6.10}$$

By substituting equation (6.8) into equation (6.6), we obtain:

$$\{F\}e^{i\omega_c t} = b\left(1 - e^{-i\omega_c\tau}\right)[A][G(i\omega_c)]\{F\}e^{i\omega_c t} \tag{6.11}$$

The geometry of tool and workpiece in most of the turning operations are symmetrical and beam-like structures, thus for many cases the cross transfer functions are negligible. Then, the transfer matrix can be further simplified as follows:

$$G(i\omega_c) = G_c(i\omega_c) + G_w(i\omega_c) = \begin{bmatrix} G_{xx} & 0 \\ 0 & G_{yy} \end{bmatrix} \tag{6.12}$$

where G_{xx} and G_{yy} are the systems total transfer functions in x and y directions. Equation (6.11) has a non-trivial solution if and only if its determinant is zero, yielding:

$$\det[[I] + \Lambda[G_0(i\omega_c)]] = 0 \tag{6.13}$$

where $[G_0(i\omega_c)] = [A][G(i\omega_c)]$, and the eigenvalue Λ is given as:

$$\Lambda = b\left(e^{-i\omega_c\tau} - 1\right) \tag{6.14}$$

Now the stability model is reduced to an eigenvalue problem. The solution of equation (6.13) results in the following:

$$\Lambda = 1/\left[G_{yy}\left(K_f \sin^2\kappa\cos\kappa + K_r \sin\kappa\cos^2\kappa\right) + G_{xx}\left(K_f \cos^3\kappa - K_r \cos^2\kappa\right)\right] \quad (6.15)$$

From equation (6.14), on the other hand, the stability limit, b_{lim}, at a certain chatter frequency can be obtained as follows:

$$b_{\text{lim}} = \frac{\Lambda_R + i\Lambda_I}{\cos\omega_c\tau - i\sin\omega_c\tau - 1} \quad (6.16)$$

Since b is a real number, the imaginary part of equation (6.16) has to vanish yielding:

$$b_{\text{lim}} = -\frac{1}{2}\Lambda_R\left(1+\lambda^2\right) \quad (6.17)$$

where:

$$\lambda = \frac{\Lambda_I}{\Lambda_R} = \frac{\sin\omega_c\tau}{1-\cos\omega_c\tau} \quad (6.18)$$

Equation (6.18) can be used to obtain a relation between the chatter frequency and the spindle speed [10, 67, 73]:

$$\varepsilon = \pi - 2\psi\,,\ \psi = \tan^{-1}\lambda \quad (6.19)$$

$$\omega_c\tau = \varepsilon + 2k\pi\,,\ n = 60/\tau \quad (6.20)$$

where ε is the phase difference between the inner and outer modulations, k is an integer corresponding to the number of waves in a period, and n is the spindle speed in rpm.

The stable depth of cut of the system can be obtained from by equation (6.17) for different chatter frequencies. These frequencies can be searched around the natural frequency of the most flexible structural mode of the system. Then, the corresponding spindle speeds can be determined from equation (6.20) for different lobes, i.e. for *k=1,2,3*…etc. Thus, the stability diagram of the dynamic system can be obtained by plotting the stable depth of cut vs. the corresponding spindle speeds for different lobes [67].

If the cross-transfer functions are significant and must be included in the analysis, the original transfer function matrix given in equation (6.9) can be used in the stability formulation. In such a case, the eigenvalue would include the cross transfer function terms in addition to ones given in equation (6.15).

6.3. Insert Nose Radius Model

In the foregoing analysis, the chip thickness and the forces on the straight cutting edge are considered only. In practice, however, most turning processes are conducted using cutting inserts with nose radii varying from 0.1 mm to as large as 7-8 mm for better finished surface and cutting performance. For stability analysis, when the (stable depth of cut /nose radius) ratio increases, the importance of including nose radius in the model increases as well.

In this study, the chip area at the nose of the tool is divided into many elements in modeling of the dynamic chip thickness. The chip area in the nose region is divided into *n* trapezoids as shown in Figure 6.3.a and Figure 6.3.b. The parameters below are used to describe the chip thickness for each element up to element *n*.

$$b_e = b_{nose}/n, \quad b_{nose} = r - r\sin\kappa \qquad i=1,...,n \tag{6.21}$$

$$b_{di} = b_e/\cos\theta_i \qquad i=1,...,n \tag{6.22}$$

$$\theta_i = \frac{\pi}{2} - \tan^{-1}\left(\frac{r - r\sin\kappa}{ns_i}\right) \qquad i=1,...,n \tag{6.23}$$

$$s_i = \sqrt{r^2 - \left(r - \frac{i}{n}(r - r\sin\kappa)\right)^2} - \sum_{j=1}^{i-1} s_j \tag{6.24}$$

where b_e is the element height or elemental depth of cut, b_{di} is the edge length of the trapezoid, r is the nose radius and θ_i is the angle that defines the orientation of an element edge.

In modeling the chip thickness at the straight cutting edge, two approaches are proposed. In the first approach, the straight edge is also meshed by the trapezoidal elements as can be seen in Figure 6.3.a. This approach is used in the modeling of the turning stability as equal element height makes the mathematical coupling of element dynamics possible. It should be noted that the second approach couldn't be used in modeling the general stability case where all the cutting angles and dynamics are present since the dynamic forces acting on each element couldn't be merged into a single matrix (see equation 6.30). In this model, $(n+1)^{st}$ element and the following elements up to element *m* are located at the straight cutting edge of the insert; therefore equation (6.21) and (6.22) is also valid for these elements. But, as it can be seen from Figure 6.3.a, their angular orientations are equal to the side edge cutting angle:

$$\theta_i = \kappa \qquad i=n+1,n+2,\ldots,m \tag{6.25}$$

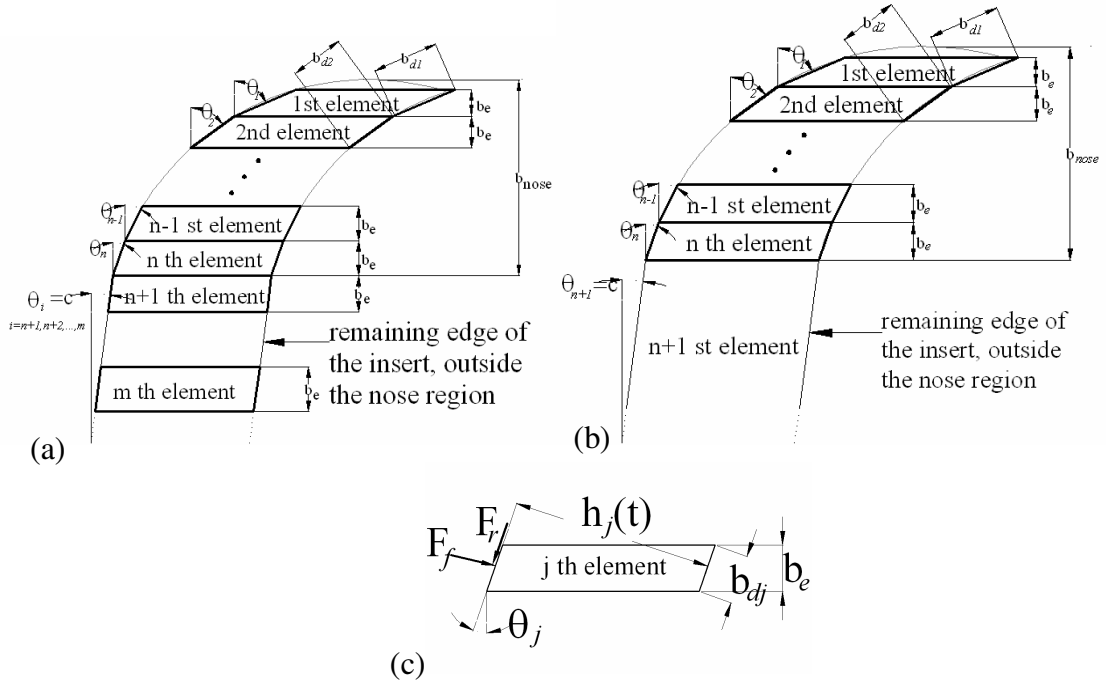

Figure 6.3: Division of chip thickness by trapezoidal elements (a) straight edge is also meshed, (b) straight edge is only defined by one element, and (c) the cutting forces acting on an element.

In the second approach, on the other hand, the straight edge is presented by only one element whose height is an unknown. Although the first approach could also be used in the boring stability model, this second approach is implemented as it reduces the stability solution into a 1D equation, and the eigenvalue of the system can be calculated easily even when the straight edge is taken as one element. In this model, $(n+1)^{st}$ element represents the straight cutting edge of the insert. As it can be seen from Figure 6.3.b, its angular orientation is equal to the side edge cutting angle, i.e. $\theta_{n+1}=\kappa$. As a conclusion, by using angular orientation angle θ, the dynamic chip thickness for the j^{th} element can be defined as follows:

$$h_j(t) = \Delta x \cos\theta_j - \Delta y \sin\theta_j \tag{6.26}$$

6.4. Stability of Turning Processes Including Insert Nose Radius Effects

In this section the stability model for turning operations that includes the nose radius model is presented. This model is called the "matrix solution" throughout the study. The nose radius alters the dynamic effects of tool and workpiece on the stability

limit by changing the contributions of the tool and workpiece transfer functions on the process dynamics, similar to the effect of side cutting edge angle. Therefore, the dynamic displacements and dynamic forces acting on all elements must be considered in the solution. Assuming m number of elements is in the cut, elemental dynamic forces acting on each element that is in cut can be written from equation (6.6) as follows:

$$\begin{Bmatrix} F_{jx} \\ F_{jy} \end{Bmatrix} = b_e \left[A_j\right] \begin{Bmatrix} \Delta x \\ \Delta y \end{Bmatrix} \qquad j=1,2,\ldots,m \tag{6.27}$$

where $[A_j]$'s are the directional coefficients that are defined by equation (6.7) and (6.23). Note that in equation (6.27) the dynamic displacements Δx and Δy represent the total dynamic displacement of the insert in cut, and can be defined as follows:

$$\begin{Bmatrix} \Delta x \\ \Delta y \end{Bmatrix} = \left(1 - e^{-i\omega_c \tau}\right)\left[G(i\omega_c)\right] \sum_{p=1}^{m} \begin{Bmatrix} F_{px} \\ F_{py} \end{Bmatrix} \tag{6.28}$$

Thus, the dynamic elemental forces can be written by substituting equation (6.28) into (6.27) as follows:

$$\begin{Bmatrix} F_{jx} \\ F_{jy} \end{Bmatrix} e^{i\omega_c t} = b_e \left(1 - e^{-i\omega_c \tau}\right)\left[A_j\right]\left[G(i\omega_c)\right] \sum_{p=1}^{m} \begin{Bmatrix} F_{px} \\ F_{py} \end{Bmatrix} e^{i\omega_c t} \qquad j=1,2,\ldots m \tag{6.29}$$

Finally, the total depth of cut of the insert can be calculated as $b=mb_e$. Since the dynamic system has now m number of degrees of freedom, it can only be solved accurately by a simultaneous solution. Therefore, as Budak et al. [67] applied it for milling stability, it is proposed to merge the dynamic equations into a matrix form which will then be reduced to an eigenvalue problem:

$$\begin{Bmatrix} \begin{bmatrix} F_{1x} \\ F_{1y} \end{bmatrix} \\ \vdots \\ \begin{bmatrix} F_{mx} \\ F_{my} \end{bmatrix} \end{Bmatrix} e^{i\omega_c t} = b_e \left(1 - e^{-i\omega_c \tau}\right)\left[G_0\right] \begin{Bmatrix} \begin{bmatrix} F_{1x} \\ F_{1y} \end{bmatrix} \\ \vdots \\ \begin{bmatrix} F_{mx} \\ F_{my} \end{bmatrix} \end{Bmatrix} e^{i\omega_c t} \tag{6.30}$$

$[G_0]$ in equation (6.30) can be considered as the elemental oriented transfer function and defined as follows:

$$\left[G_0\right] = \underbrace{\begin{bmatrix} [A_1] & [A_1] & \cdots & [A_1] \\ \vdots & & & \vdots \\ [A_m] & [A_m] & \cdots & [A_m] \end{bmatrix}}_{(2m \times 2m)} \underbrace{\begin{bmatrix} [G] & 0 & 0 \\ 0 & \ddots & 0 \\ 0 & 0 & [G] \end{bmatrix}}_{(2m \times 2m)}$$

and the solution is possible if and only if the determinant of equation (6.30) is equal to zero. The eigenvalue Λ is defined in equation (6.30) as follows.

$$\Lambda = b_e\left(1 - e^{-i\omega_c\tau}\right) \tag{6.31}$$

As a result of equations (6.31) and (6.30), the dynamic problem is reduced to the same eigenvalue problem discussed in Chapter 6.2. Thus, the eigenvalue can be calculated from equation (6.13), and in order to solve the chatter stability limit the same procedure can be followed.

One can notice from equation (6.30) that this solution provides the elemental stability limit, b_{elim}, which is the stability limit for only one element. Therefore the stability of the system b_{lim} is calculated by multiplying b_{elim} with the elements that are in cut, that is $b_{\text{lim}}=mb_{\text{elim}}$. However, the number of elements that are in cut is another unknown. Hence, a search-based solution procedure is proposed as follows. The first step of the procedure is to guess the number of elements that meshes the nose radius n in the beginning which is then used to calculate b_e, i.e. $b_e= b_{\text{nose}}/n$. Also the total number of meshing elements m, has to be selected in the beginning. It should be noted here that 10 elements are found to be enough for precise predictions. Then, the stability solution is followed step by step for each element. At each step it should be checked whether b_{lim} is smaller than b. If b_{lim} is found to be greater than b, then the iteration continues by adding the next element into solution. It should be noted here that, selecting bigger m values or smaller b_e values increases the precision of the solution.

The main difference of this procedure from the method given in Chapter 6.2 is the way the eigenvalue problem is solved. In a one element solution the eigenvalue can be calculated analytically. However, for the multi-element model when the dynamics of both tool and workpiece is included, as the number of elements increases, so does the dimension of the directional coefficient matrix. Therefore, a numerical solution is needed for the eigenvalue of the dynamic system.

6.5. Stability of Boring Processes

The stability model for boring operations is similar to the turning operations except in a few points. Firstly, since the stable depth of cuts in boring are comparable to the insert nose radius, the effect of insert nose radius becomes critical. Secondly, the boring process coordinates are different which results in a modification of the dynamic chip

thickness relationship (Figure 6.4). Thus, in order to formulate the stability in boring operations, an insert nose model is proposed. Then, a similar procedure is followed in order to obtain the dynamic system equations. It is also shown that the stability model in boring operations reduces to a 1D equation even including the insert nose radius effect.

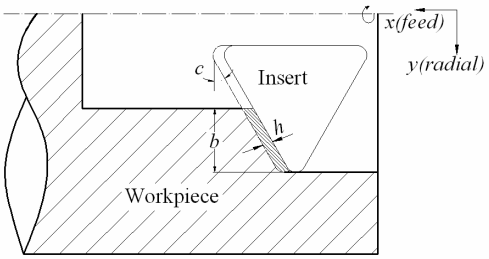

Figure 6.4: Schematic description of chip thickness and lathe coordinates in boring.

It should be noted here that the stability problem in boring can still be solved using the matrix solution model presented in Chapter 6.4. However, a 1D model is proposed for boring operations which provides the same prediction accuracy with a faster solution time. This model is called "1D solution" throughout the study.

6.5.1. Stability Limit Solution for Stable Depth of Cuts Higher Than the Nose Radius

In order to model the dynamic system's stability, the relationship between the dynamic boring forces and the dynamic chip thickness is defined. Then, the problem is reduced to a 1D eigenvalue problem by the help of a reduced transfer function matrix, and solved analytically.

Similar to the turning stability model, the relationship between the dynamic forces and the chip thickness in lathe coordinates can be written as follows:

$$\begin{Bmatrix} F_{jx} \\ F_{jy} \end{Bmatrix} = b_j \left[A_j\right] \begin{Bmatrix} \Delta x \\ \Delta y \end{Bmatrix} \qquad j=1,2,\ldots,n+1 \tag{6.32}$$

where,

$b_j=b_e$ $\qquad j=1,2,\ldots,n$

$b_j=b_m$ $\qquad j=n+1$

and $[A_j]$'s are the directional coefficient matrices which are defined for each element as follows:

$$\left[A_j\right]=\begin{bmatrix} A_{j11} & A_{j12} \\ A_{j21} & A_{j22} \end{bmatrix}=\begin{bmatrix} \cos\theta_j & \sin\theta_j \\ -\sin\theta_j & \cos\theta_j \end{bmatrix}\begin{bmatrix} K_f \\ K_r \end{bmatrix}\begin{bmatrix} 1 & \tan\theta_j \end{bmatrix} \tag{6.33}$$

Note that in equation (6.32) the dynamic displacements Δx and Δy are the total dynamic displacements of the insert in cut, and can be defined as follows:

$$\begin{Bmatrix} \Delta x \\ \Delta y \end{Bmatrix}=\left(1-e^{-i\omega_c\tau}\right)\left[G(i\omega_c)\right]\left[\begin{Bmatrix} F_{1x} \\ F_{1y} \end{Bmatrix}+\begin{Bmatrix} F_{2x} \\ F_{2y} \end{Bmatrix}+\ldots\begin{Bmatrix} F_{n+1x} \\ F_{n+1y} \end{Bmatrix}\right] \tag{6.34}$$

where the transfer function matrix $[G(i\omega_c)]$ is assumed to include only the transfer function in *y*-direction, because in almost all of the boring operations the tool and the workpiece are much more rigid in the *x*-direction and can be neglected. Therefore, the transfer function matrix is given as:

$$\left[G(i\omega_c)\right]=\begin{bmatrix} 0 & 0 \\ 0 & \phi_{yy} \end{bmatrix} \tag{6.35}$$

Substituting equation (6.34) into equation (6.32) the dynamic elemental force for the j^{th} element can be obtained as follows:

$$\left[F_j\right]e^{i\omega_c t}=b_j\left(1-e^{-i\omega_c\tau}\right)\left[A_j\right]\left[G(i\omega_c)\right]\sum_{p=1}^{n+1}\left[F_p\right]e^{i\omega_c t} \tag{6.36}$$

As it can be seen from the above equation, there are now $(n+1)$ equations to solve. The first (n) equations that model the nose radius have the same depth of cut b_e, which is known. However, the last equation that models the straight edge, has the depth of cut b_m which is to be solved for stability. Adding up all the equations the following is obtained:

$$\sum_{p=1}^{n+1}\left[F_p\right]e^{i\omega_c t}=\left(1-e^{-i\omega_c\tau}\right)\left\{b_m\left[A_m\right]+b_e\sum_{p=1}^{n}\left[A_p\right]\right\}\left[G(i\omega_c)\right]\sum_{p=1}^{n+1}\left[F_p\right]e^{i\omega_c t} \tag{6.37}$$

Define $[C]$ as follows:

$$\left[C\right]=\begin{bmatrix} C_{11} & C_{12} \\ C_{21} & C_{22} \end{bmatrix}=\left(e^{-i\omega_c\tau}-1\right)\left[B\right] \tag{6.38}$$

where:

$$\left[B\right]=\begin{bmatrix} B_{11} & B_{12} \\ B_{21} & B_{22} \end{bmatrix}=b_m\left[A_m\right]+b_e\sum_{p=1}^{n}\left[A_p\right] \tag{6.39}$$

The solution of equation (6.37) is possible if and only if its determinant is equal to 0, which yields:

$$\det[[I]+[C][G(i\omega_c)]]=0 \tag{6.40}$$

The solution of equation (6.40) results in the following:

$$C_{22}=-1/\phi_{yy} \tag{6.41}$$

Letting C_{22} be Λ and rewriting equation (6.37) the below is obtained:

$$\sum_{p=1}^{n+1}F_{py}e^{i\omega_c t}=\Lambda\phi_{yy}\sum_{p=1}^{n+1}F_{py}e^{i\omega_c t} \tag{6.42}$$

Now the problem reduces to a 1D eigenvalue problem, and equation (6.38) reduces to the following:

$$\Lambda=\left(e^{-i\omega_c\tau}-1\right)B_{22} \tag{6.43}$$

A_{j22} can also be calculated from equation (6.33) as follows:

$$A_{j22}=\left(-\sin\theta_j+\cos\theta_j K_r\right)\tan\theta_j \tag{6.44}$$

Further, B_{22} is equal to the stability limit $B_{22\text{lim}}$ at a chatter frequency. Since $B_{22\text{lim}}$ should be a real number, the imaginary part has to vanish, yielding:

$$B_{22\text{lim}}=-\frac{1}{2}\Lambda_R\left(1+\lambda^2\right) \tag{6.45}$$

where λ is defined in equation (6.18) which then results in equations (6.19) and (6.20) in order to obtain a relationship between the chatter frequency and the spindle speed. Substituting equation (6.45) into equation (6.39), the following is obtained:

$$b_{m,\text{lim}}=\left[-\frac{1}{2}\Lambda_R\left(1+\lambda^2\right)-b_e\sum_{p=1}^{n}A_{p22}\right]/A_{m22} \tag{6.46}$$

Note that $b_{m,\text{lim}}$ is the limiting stable depth of cut for only the straight edge. Thus, the stable depth of cut of the dynamic system b_{lim} can be obtained by adding up the rest of the insert in cut as follows:

$$b_{\text{lim}}=b_{m,\text{lim}}+nb_e \tag{6.47}$$

Once the stability limit is obtained, the stability lobes can be derived using the method described in Chapter 6.2.

It should be noted here that the stability model derived for turning operations can be reduced to a 1D expression as derived for boring stability, in some cases. Theses cases should satisfy the condition that only one components' dynamics contributes to the dynamic system i.e. when one of the tool or workpiece dynamics can be neglected due its rigidity.

6.5.2. Stability Limit Solution for Stable Depth of Cuts Smaller Than the Nose Radius

The solution method presented in Chapter 6.5.1 is also applicable for the case where the stable depth of cut of the dynamic system is inside the nose section of the insert. However, a step by step search is needed, i.e. the method presented above should be applied for each element incrementally until instability is obtained. For instance, for the j^{th} element equation (6.46) takes the following form:

$$b_{j,\lim} = \left[-\frac{1}{2}\lambda_R\left(1+\kappa^2\right) - b_e \sum_{p=1}^{j-1} A_{p22} \right] / A_{j22} \tag{6.48}$$

If the elemental stable depth of cut $b_{i,\lim}$ is smaller than b_e, the solution is obtained, otherwise the solution is continued with the $(i+1)^{st}$ element. Again, once the stability limit is obtained, the stability diagram can be generated using the method presented in Chapter 6.2.

6.6. Simulation Results

The stability models presented in the previous sections have been programmed in order to perform simulations, and to illustrate the effects of different parameters on the stability limits. It should be noted here that the stability lobes of turning and boring processes are relatively narrow compared to milling lobes due to the spindle speed limitations and the single cutting tooth. Thus, the main objective of the stability analysis and the simulations is to determine and discuss on the absolute stability limit.

6.6.1. Selection of Number of Meshing Elements

The number of elements that meshes the chip thickness is another parameter in the model. It affects the accuracy of the solution as well as the solution time, which is demonstrated in this and the next section with simulations. The number of elements vs. stability limit comparison is given for two different cases in turning operations. In the first case the workpiece is more flexible whereas in the second case the tool has a higher

flexibility compared to the workpiece. It should be noted here that the number of elements that meshes only the nose radius is considered here. The parameters used are listed in Table 6.1.

Table 6.1: Parameters used in the number of meshing elements simulations.

Side edge cutting angle	30°
Rake angle	5°
Inclination angle	5°
Structural damping coefficients of cutter and workpiece	%0.6
Natural frequencies of cutter and workpiece	1200 Hz
Stiffness of the tool (flexible tool, flexible workpiece)	$4x10^4$,$40x10^4$ N/mm
Stiffness of the workpiece (flexible tool, flexible workpiece)	$40x10^4$, $4x10^4$ N/mm
Shear Stress in the shear plane	600 MPa
Friction angle	28°
Shear angle	30°

The results can be seen in Figure 6.5.a for the flexible workpiece case and Figure 6.5.b for the flexible tool case. Observing the figures, it can be concluded that, a very low number of elements, i.e. fewer than five, may result in inaccurate results. However, the stability limit converges to a value, after 20 elements for both cases. But it should also be noted here that the variation of stability limit after 10 elements is negligible. Therefore, it can be concluded that reasonable results may be attained with around 10 elements.

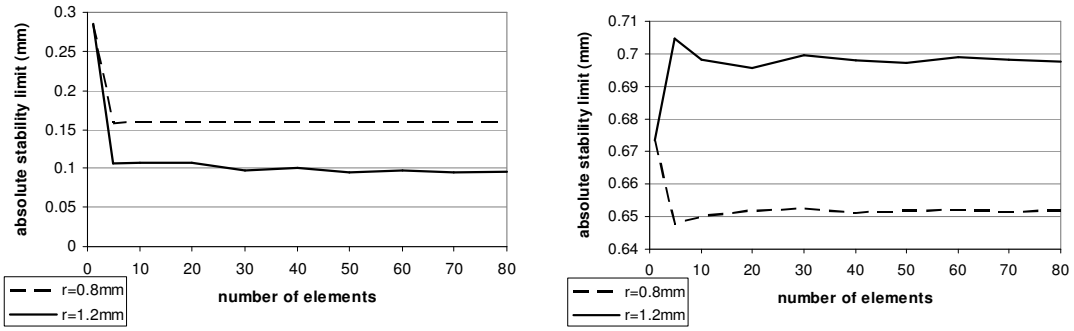

(a) (b)

Figure 6.5: Number of elements vs absolute stability limit for (a) flexible workpiece, and (b) flexible tool cases.

6.6.2. Comparison of Models for Boring Stability

As presented in Chapter 6.5, the stability in boring can be modeled by both matrix and 1D solution methods. In this section, these methods are compared. The values used in the comparison analysis are listed in Table 6.2.

Table 6.2: Parameters used in comparison of models for boring process stability.

Side edge cutting angle	10°
Rake angle	0°
Inclination angle	0°
Structural damping coefficients of the tool	%1
Natural frequency of the tool	1000 Hz
Stiffness of the tool	$3x10^4$ N/mm
Cutting force coefficient, K_t	1000 MPa
Nose radius	0.8 mm
Number of elements	30

The results of the comparison can be found in Figure 6.6. As expected, the results of both solutions are very close.

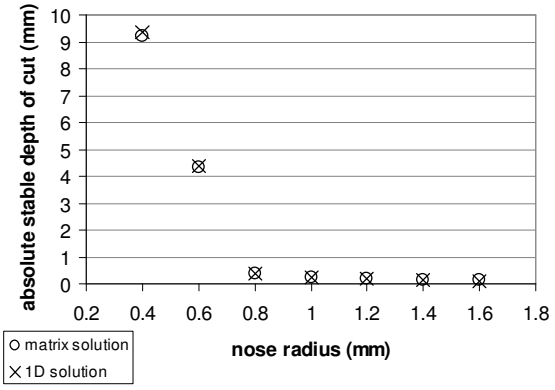

Figure 6.6: Comparison of matrix and 1D solution method for absolute stability limit in boring operations.

Another simulation is carried out to compare the solution time between matrix and 1D solution methods where the nose radius of the tool is 0.7 mm and other parameters used are listed in Table 6.2. The solution times are compared for calculation of one stability lobe and the results can be found in Figure 6.7. Two cases are considered to give a better idea about the simulation times. In, Figure 6.7.a, the first case where the

stability limit is relatively very high is shown. In this case, solution time drastically increases with the matrix solution method where bigger matrices are constructed for eigenvalue solution. However the computational time for 1D solution is very low, since only a 1D equation is solved. In the second case shown in Figure 6.7.b where the stability limit is smaller, although the solution times still differ as much as 80%, the solution times are very small for both methods.

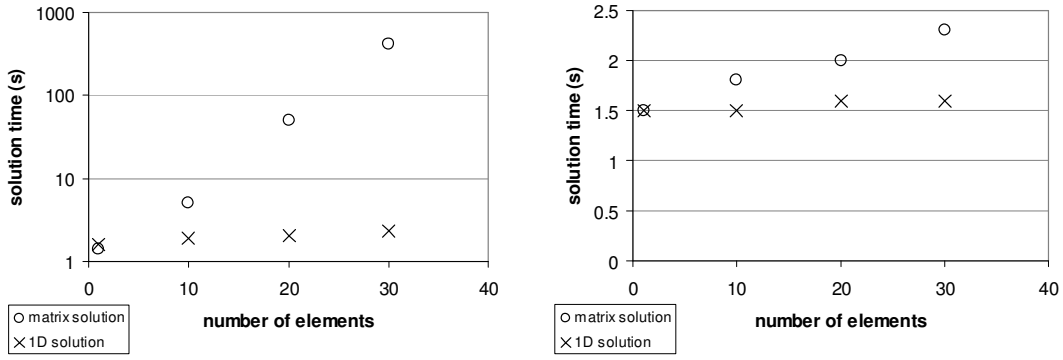

(a) (b)

Figure 6.7: Comparison of matrix and 1D solution method for the solution time for (a)higher, and (b) smaller absolute stable depths of cut.

6.6.3. Effect of the Nose Radius and Flexibility of the Components on the Stability Limit

In order to analyze the effect of insert nose radius on the absolute stable depth of cut, simulations are carried out with three different nose radii, r=0.4, 0.8 and 1.2 mm and without nose radius for different tool and workpiece stiffness values, which are listed in Table 6.3. The side edge cutting angle used in these simulations is 0° and other parameters used are listed in Table 6.1.

Table 6.3: The stiffness value trend used in simulations.

k_ratio	k_w (N/mm)	k_t (N/mm)
0.1	$5x10^4$	$50x10^4$
1	$5x10^4$	$5x10^4$
10	$50x10^4$	$5x10^4$

Increase in insert nose radius increases the effects of the dynamics in the y direction on the system (see Figure 6.1.a). Noting also that the simulations are conducted with 0º side edge cutting angle, the stability without insert nose radius is only affected by the dynamics of the tool. Therefore, as it can be observed from the left hand side of Figure 6.8, simulation without the insert nose radius has the highest stability limit since it is only affected by the tool's dynamics which is more rigid. However, as the insert nose radius increases, the effect of workpiece dynamics contributes to the system dynamics more making it more flexible reducing the stability limit. Similarly, on the right hand side of Figure 6.8, where the tool is more flexible, increase in insert nose radius reduces the contribution of the tool dynamics increasing the stability limit.

It should also be observed from Figure 6.8 that the effect of the insert nose radius on the stability limit is more when the workpiece is more flexible. This is because of the fact that the dynamics of the system is mainly controlled by the tool, and when the contribution of the workpiece dynamics is added, it adds flexibility to the system which drastically reduces the stability limit. However, when the tool is more flexible, the added rigidity of the workpiece does not affect the stability of the system as much.

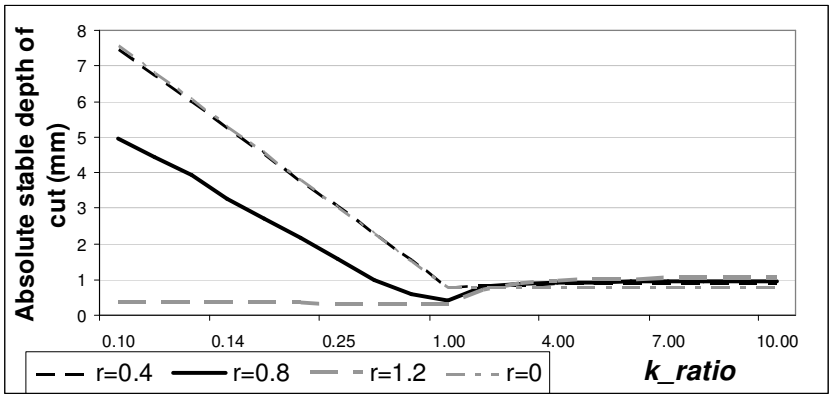

Figure 6.8: Variation of absolute stability limit with tool and workpiece stiffness for different r values.

7. VERIFICATION OF THE PROPOSED STABILITY MODEL AND COMPARISON WITH THE ONE DIMENSIONAL ORIENTED TRANSFER FUNCTION STABILITY MODEL

In this section, chatter experiments conducted for the verification of the stability models proposed in Chapter 6 are presented. Also, the comparison between the widely used one dimensional oriented transfer function stability model and the proposed multi-dimensional stability model is presented and discussed in detail.

7.1. Experimental Setup and Procedure

Chatter tests were conducted in order to obtain the absolute stability limit of the dynamic system experimentally in both turning and boring operations. The stability lobes in turning and boring operations are very narrow compared to milling stability lobes due to the lower spindle speeds and the single cutting tooth. Thus, the experiments aim to verify the predicted absolute stability limits. In the chatter tests, the depths of cut were selected to verify the stable and unstable cutting zones, thus the absolute stability limit. In order to confirm the absolute stability limit prediction, a fine variation of the depths is used. Also, the effect of the nose radius on the absolute stability limit is considered in the experiments by using inserts with different radii.

A conventional manual lathe is used during the experiments, which allows for specific spindle speeds, i.e. 700, 1000, 1400, 2000 rpm. A modal test setup is used to measure the transfer functions of the workpiece and the tool (Figure 7.1.a and Figure 7.1.b). The modal test setup consists of an impact hammer, an accelerometer and a data acquisition system. The data is collected and analyzed by CutPro® [97]. In addition, a sound frequency measurement setup was prepared in order to measure and verify the chatter frequency (Figure 7.1.c and Figure 7.1.d). The setup consists of a microphone and a data acquisition setup. The data is collected and analyzed by LabView® [98]. As

a second check the finished surface is observed by the naked eye for chatter marks in order to verify the unstable cutting operation.

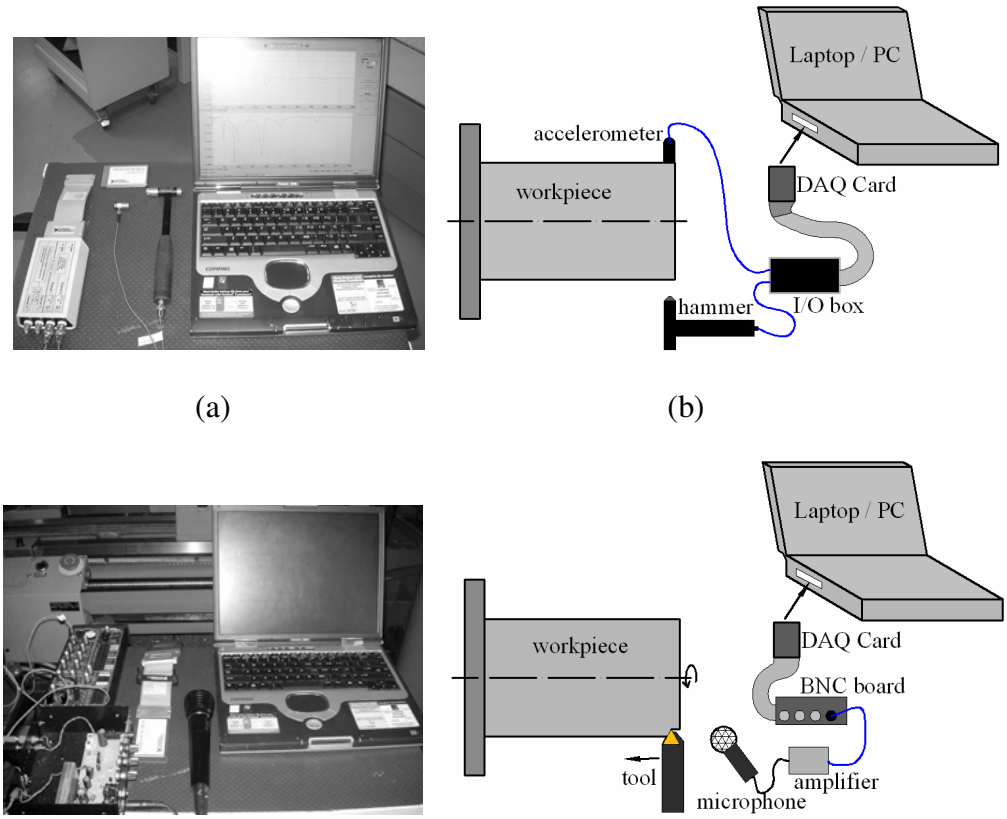

Figure 7.1: (a), (b) Modal test setup, (c), (d) Frequency measurement setup.

In experiments, coated carbide triangular inserts with 0^{o} rake angle are used. There are three inserts having different nose radii, i.e. 0.4, 0.8, and 1.2 mm as can be seen in Figure 7.2.a, Figure 7.2.b, and Figure 7.2.c, respectively. A round insert (Figure 7.2.d) is also used in order to verify the nose radius model. Also A feed rate of 0.08 mm/rev was used for all tests.

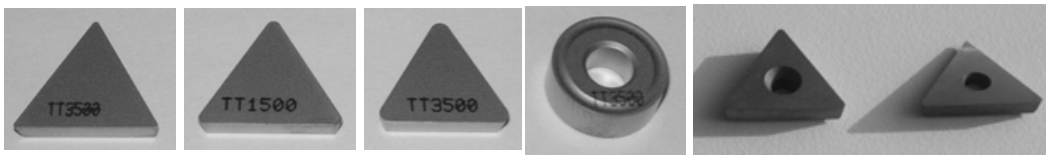

(a) (b) (c) (d) (e) (f)

Figure 7.2: Triangular inserts used during tests with radii (a)0.4 mm, (b)0.8 mm, (c)1.2 mm, and (d) the round insert with a 12.6 mm diameter. (e) Regular insert seat, and, (f) Ground insert seat for desired rake and inclination.

In order to avoid eccentricity and to cover a wider range of angles in a practical manner, insert seats with different angles were ground and used under the inserts during the cutting tests (Figure 7.2.e and Figure 7.2.f). The side edge cutting angle in the turning experiments is set by rotating the tool holder from its clamped end. The workpiece material used during the tests is a medium carbon steel (AISI 1040), and an existing orthogonal database was used for the cutting force coefficients. The orthogonal database was generated by using orthogonal tube cutting tests. The cutting forces and the cut chip thickness were measured during the tests which were conducted at different cutting speeds and feed rates in order to identify the shear angle, the shear stress and the friction angle [74-76] using the orthogonal cutting model.

7.2. Chatter Verification Experiments Case 1: Flexible Turning Tool and Rigid Workpiece

In the first experiment case, the turning chatter experiments are conducted in which the tool is more flexible than the workpiece. Inserts with different nose radii and round insert tests are used in order to compare the predicted results. In the verification of the nose radius model in the second set, the aim is to verify the effect of the nose radius on the stability limit. In the final set the round nose inserts are used in chatter experiments, in order to verify the model for the inserts without straight edges.

7.2.1. Turning with Flexible Tool: Verification of Stability Limit

The first set of experiments is carried out in order to verify the proposed stability model given in Chapter 6. The parameters that are used in the experiments and stability analysis are listed in Table 7.1. The other parameters can be found in Chapter 7.1. The comparison of the workpiece and tool transfer functions is shown in Figure 7.3.a.

The analytically calculated stability lobes along with the experimental results and an example of a surface finish after a stable and unstable operation for 2000 rpm can be seen in Figure 7.3.c. Also, the chatter frequency measurements at 2000 rpm tests are shown in Figure 7.3.b. The experimental and the analytical results are in close agreement.

Table 7.1: Parameters used in the verification of flexible tool turning chatter experiments.

Side edge cutting angle	10°
Rake angle	5°
Inclination angle	5°
Insert nose radius	0.4mm
Cutting force coefficients, K_f	800 MPa
Cutting force coefficients, K_r	128 MPa
Natural frequency of the tool	1100Hz
Stiffness of the tool	$1.2x10^7$N/m
Damping ratio	0.015

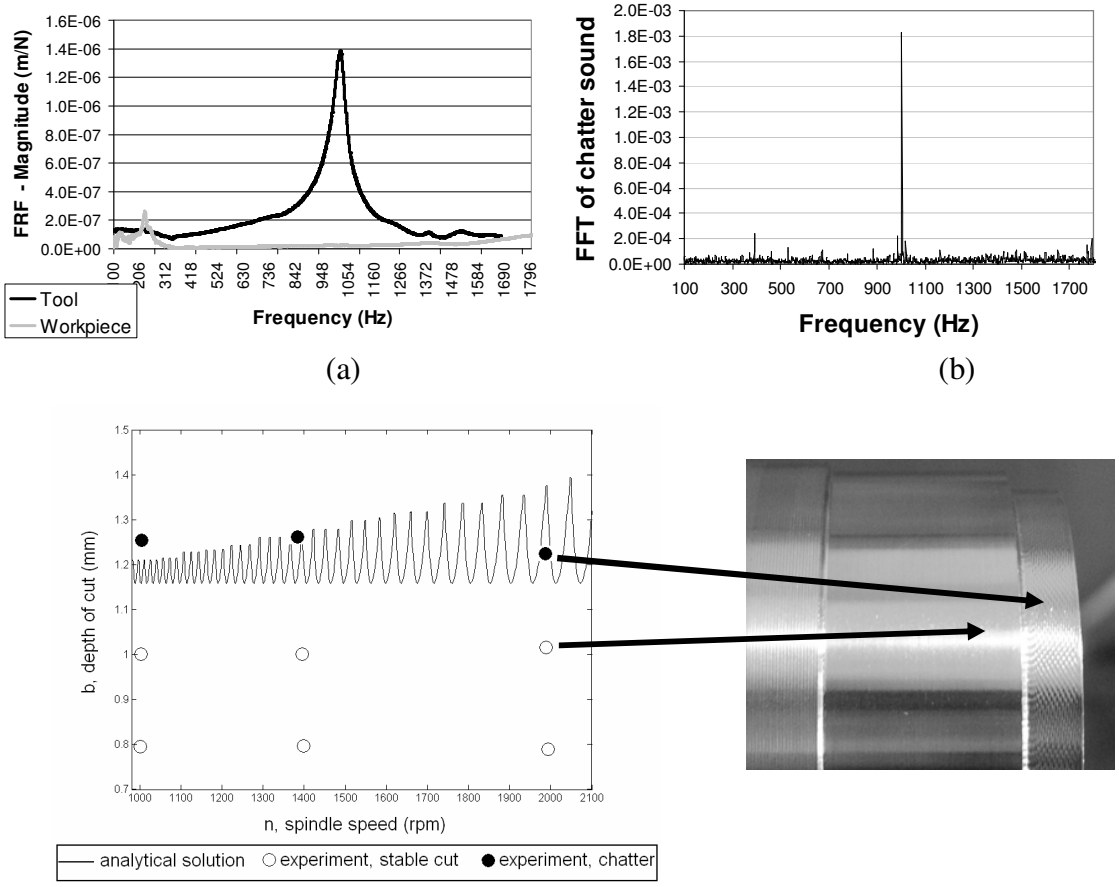

Figure 7.3: (a)Transfer functions of the tool and the workpiece (b) Chatter frequency measurement result at 2000 rpm experiments, and (c) chatter test results for model verification and the surface finish of a stable vs. unstable cut.

7.2.2. Turning with Flexible Tool: Demonstration and Verification of Nose Radius Effects

In the second set of experiments of this case, the effect of the insert nose radius on the stability limit is demonstrated and verified for a case where the tool is more flexible than the workpiece. The cutting conditions and angles that are used during chatter tests and stability analysis are listed in Table 7.2. The other parameters can be found in Chapter 7.1.

Table 7.2: Parameters used in the verification tests with inserts having nose radius.

Side edge cutting angle	10°
Rake angle	5°
Inclination angle	5°
Spindle Speed	1000 rpm
Cutting force coefficients, K_f	800 MPa
Cutting force coefficients, K_r	128 MPa
Natural frequency of the tool	1100Hz
Stiffness of the tool	$1.2x10^7$N/m
Damping ratio	0.015

The predictions along with the experimental results can be seen in Figure 7.4. The insert nose radius contributes to the dynamic system similar to the effect of the side edge cutting angle. Therefore, as the insert nose radius increases the effect of the dynamics in the depth of cut direction increases as well. So, the increase in the insert nose radius increases the effect of the workpiece dynamics on the cutting system. Since the tool is more flexible than the workpiece, this makes the system more rigid increasing the stability limit. This behavior is also observed in the experimental results, and a high level of agreement with the analytical predictions is obtained.

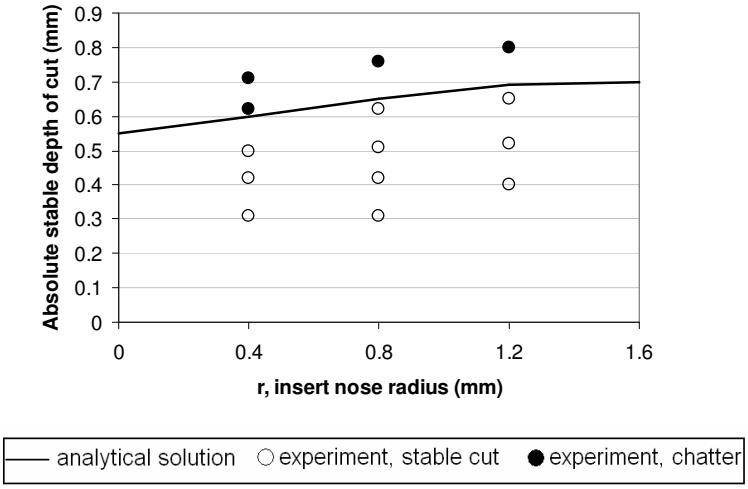

Figure 7.4: Chatter test results for nose radius effect demonstration and verification.

7.2.3. Turning with Flexible Tool: Round Insert Experiments

In this first case of the last set of experiments, the insert nose radius model is verified by a round insert where the tool is more flexible than the workpiece. The cutting conditions and angles that are used during chatter tests and stability predictions are listed in Table 7.3. The other parameters can be found in Chapter 7.1.

Table 7.3: Parameters used in the verification of round insert for flexible tool turning experiments.

Rake angle	5°
Inclination angle	-5°
Cutting force coefficients, K_f	800 MPa
Cutting force coefficients, K_r	128 MPa
Natural frequency of the tool	1162 Hz
Stiffness of the tool	$9x10^6$N/m
Damping ratio	0.011

The comparison of experimental and analytical results can be seen in Figure 7.5. Reasonable agreement is found between the analytical and experimental results.

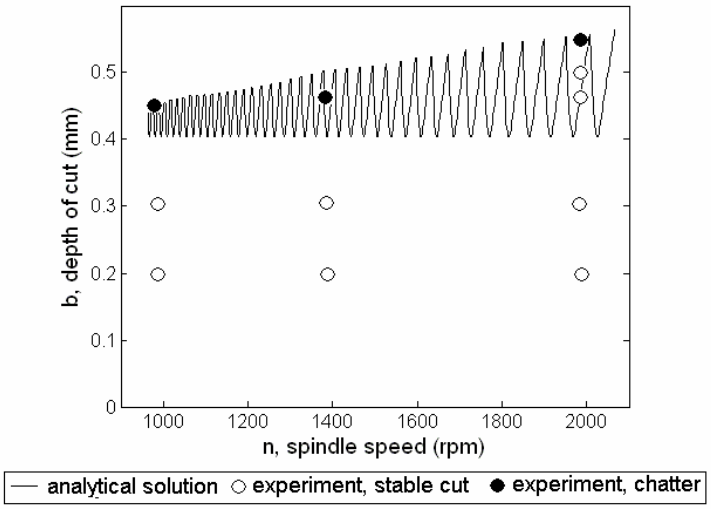

Figure 7.5: Chatter test results for round nose insert.

7.3. Chatter Verification Experiments Case 2: Flexible Workpiece and Rigid Turning Tool

In the second case, the turning chatter experiments are conducted where the workpiece is clamped in such a way that it is more flexible than the tool. The nose radius is varied in the tests in order to compare with the predicted results.

7.3.1. Turning of a Flexible Workpiece: Verification of Stability Limit

This first set of experiments is conducted in order to verify the proposed stability model for the case where the workpiece is more flexible than the tool. The parameters that are used specifically for the verification of flexible workpiece turning chatter experiments and stability predictions are listed in Table 7.4. The other parameters can be found in Chapter 7.1. The workpiece diameter and the length were 39 mm and 75 mm, respectively. Moreover, the comparison between the tool and workpiece transfer functions is shown in Figure 7.6.a.

The predicted stability lobes and experimental results are given in Figure 7.6.c where a sample finished surface after a stable and unstable operation can be seen. Also, the measured chatter sound for 1400 rpm is given in Figure 7.6.b. The difference in 700 and 1000 rpm tests are caused by the process damping due to the low cutting speed used [99, 100]. Reasonable agreement is observed between the experimental and analytical results.

Table 7.4: Parameters used in flexible workpiece turning chatter experiments.

Side edge cutting angle	30°
Rake angle	5°
Inclination angle	5°
Insert nose radius	0.4mm
Cutting force coefficients, K_f	632 MPa
Cutting force coefficients, K_r	44 MPa
Natural frequency of the workpiece	770 Hz
Stiffness of the workpiece	$6.6x10^6$N/m
Damping ratio	0.025

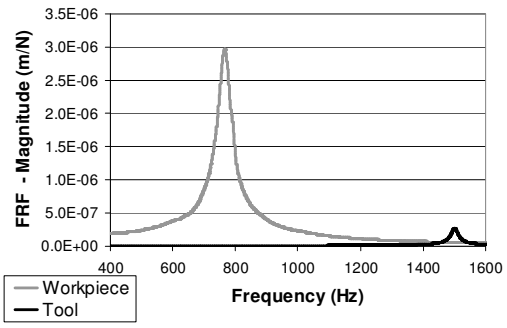

(a)

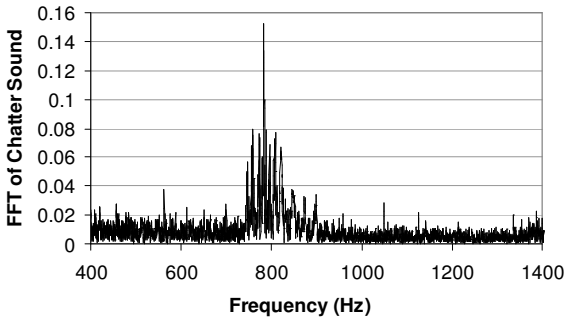

(b)

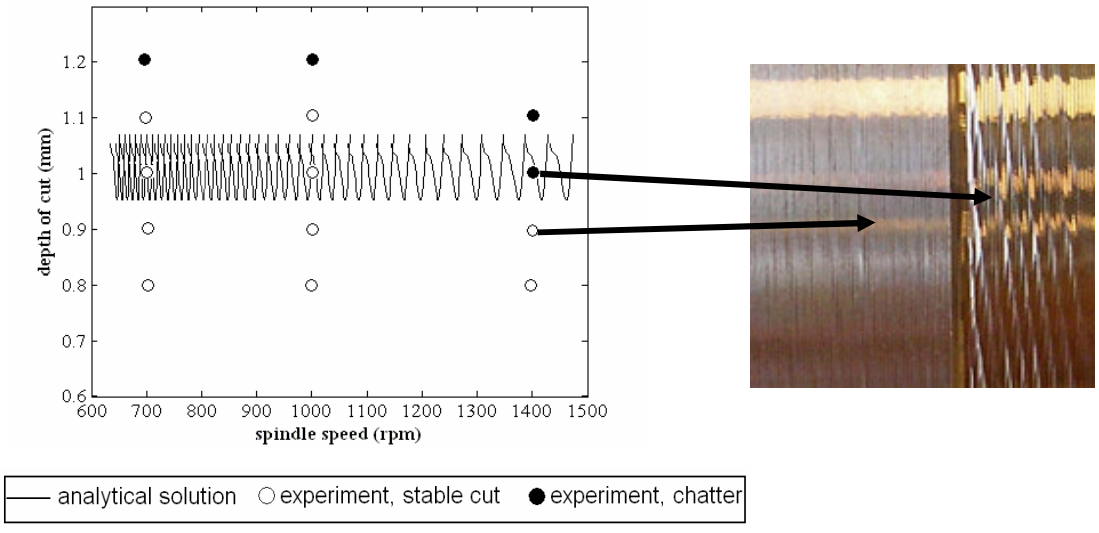

(c)

Figure 7.6:(a) Transfer functions of the tool and the workpiece, (b) chatter sound measurement results for 1400 rpm tests, and (c)chatter test results for model verification and the surface finish of a stable vs. unstable cut.

7.3.2. Turning of a Flexible Workpiece: Demonstration and Verification of Nose Radius Effects

In the second set of experiments of this case, the effect of the insert nose radius on the stability limit is demonstrated, and verified with an experiment where the workpiece is more flexible than the tool. The cutting conditions and angles used during the chatter tests and the stability predictions are listed in Table 7.5. The spindle speed used during experiments is 1400 rpm. The other parameters can be found in Chapter 7.1. As in the previous tests, the workpiece diameter was 39 mm and the length was 75 mm.

Table 7.5: Parameters used in the verification of chatter tests with inserts having nose radius.

Side edge cutting angle	25°
Rake angle	5°
Inclination angle	5°
Spindle Speed	1400 rpm
Cutting force coefficients, K_f	632 MPa
Cutting force coefficients, K_r	44 MPa
Natural frequency of the workpiece	707 Hz
Stiffness of the workpiece	6.5×10^6 N/m
Damping ratio	0.023

The analytically predicted stability diagram along with the experimental results is given in Figure 7.7. As the insert nose radius increases, the effect of workpiece dynamics (which is more flexible) on the chip thickness also increases. Therefore, the dynamic system becomes more flexible resulting in a decrease in the absolute stability limit. Another conclusion, which was also shown in Chapter 6 by the simulations, is that the effect of the insert nose radius on the stability is more pronounced in flexible workpiece case than in flexible tool case (see Figure 7.4 and Figure 7.7). In order to explain this situation, firstly it should be noted that when the side edge cutting angle and insert nose radius are zero, the system dynamics are only controlled by the transfer function of the tool in the feed direction. The workpiece dynamics can only affect the dynamics of the cutting system if there is a side edge cutting angle, or the insert has a nose radius. In that case, if the workpiece is more flexible than the tool, the flexibility introduced to the dynamic system reduces the stability limit drastically. On the other

hand, if the workpiece is more rigid than the tool, the dynamic rigidity of the system may increase, and the level of increase depends on the relative rigidities of the tool and the workpiece as well as values of the side cutting edge angle or nose radius. Comparing the experimental results and the analytical predictions presented in this section, a close agreement can be concluded.

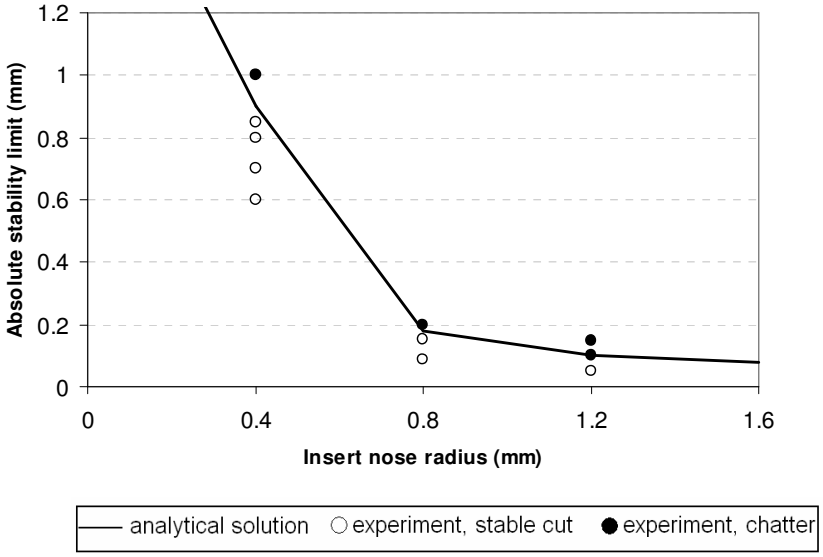

Figure 7.7: Chatter test results for the flexible workpiece case with inserts having different nose radii.

7.4. Chatter Verification Experiment Case 3: Boring Experiments

In this last case, boring chatter experiments were conducted where the tool was clamped in such a way that it was much more flexible than the workpiece representing the common problem in practical boring applications. The nose radius is varied in order to verify the predicted results. The cutting conditions and angles used in the chatter tests and stability analysis are listed in Table 7.6. The other parameters can be found in section 7.1.

The analytically predicted absolute stability limits and the experimental results for inserts with 0.4, 0.8 and 1.2 mm nose radius are shown in Figure 7.8. The analytical stability limit for the insert with 0.4 mm nose radius is around 8 mm. However, during the tests a maximum depth of cut of 1 mm was imposed in order to avoid high cutting forces, and consequently high deformation that the slender boring bar will encounter. The results are also shown for the other two inserts with 0.8 and 1.2 mm nose radii. It

should also be noted here that the observed trend of the absolute stability limit with the varying insert nose radius is expected. In case of boring, an increase in the nose radius increases the effect of the tool's flexibility on the dynamic cutting system which reduces the absolute stability limit. The drastic change in the absolute stability limit is due to the sudden increase of the flexible tool's effect on the rigid dynamic system, which was also observed in Chapter 7.3.2 for the flexible workpiece tests.

Table 7.6: Parameters used in the verification of boring chatter experiments.

Side edge cutting angle	0°
Rake angle	0°
Inclination angle	0°
Spindle speed	1400 rpm
Cutting force coefficients, K_f	700 MPa
Natural frequency of the tool	3690 Hz
Stiffness of the tool	$2.3x10^7$N/m
Damping ratio	0.012

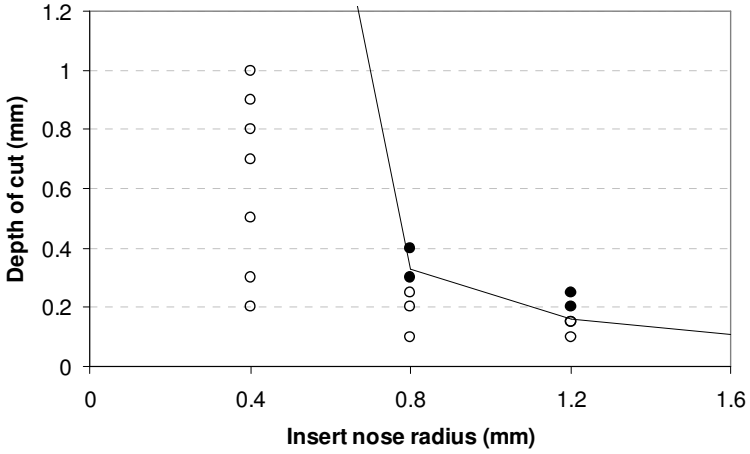

Figure 7.8: Chatter test results for boring model verification and the surface finish of a stable vs. unstable cut.

7.5. Comparison of Conventional One Dimensional Oriented Transfer Function and Proposed Stability Model

The main objective of this section is to compare the stability predictions of this multi dimensional model with the commonly used one dimensional oriented transfer function model in order to demonstrate the effects of multi dimensional dynamics and to show cases where one dimensional approach results in large errors. The results presented in the study can provide a better understanding on the multi dimensional turning dynamics, and can be used to identify cases where the multi dimensional approach must be used for accurate predictions.

Several simulations are conducted in order to compare the stability models for different cases. Since the stability lobes in turning operations are very narrow due to smaller cutting speeds and only one cutting tooth, only the absolute stability limit is considered for comparisons. In the first case, the models are compared for different inclination angles, where in the second case the nose radius effect is taken into account. For the last case a round insert is simulated as it presents different stability behavior then regular straight edge inserts. It should be noted here that, since multi dimensional stability model is verified using several chatter experiments with different cutting angles and nose radii, it is selected as the base for the comparisons.

7.5.1. One Dimensional Oriented Transfer Function Stability Model

In this section, stability limit predictions with one dimensional oriented transfer function (1DOTF) stability model will be considered briefly and the limitations of the model will be discussed. The base approach of the 1DOTF stability model is to orient the transfer functions of the dynamic system to the resultant force direction [64]. Since the oriented transfer function approach is applied to the dynamic components on the same plane, out of plane (third dimension) components are not considered. Therefore the effect of the inclination angle in a turning operation is not taken into account in the formulation. Because of this, only the effect of the side edge cutting angle and rake angle could be considered. The resultant force, $F_f(t)$, in a 2D turning operation , i.e. with side edge cutting angle and without inclination angle, can be written in terms of oriented transfer function as follows (see Figure 7.9):

$$F(t) = K_f b \frac{h(t)}{\cos\kappa} = \frac{K_f}{\cos\kappa} b F(t) G_o(i\omega_c) \tag{7.1}$$

where the oriented transfer function G_o(iωc) is defined as follows [64]:

$$G_o(i\omega_c) = \cos^2(\kappa) G_t(i\omega_c) + \cos^2(1.5\pi + \kappa) G_w(i\omega_c) \tag{7.2}$$

where $G_t(i\omega_c)$ represents the transfer function of the tool and $G_w(i\omega_c)$ represents the transfer function of the workpiece.

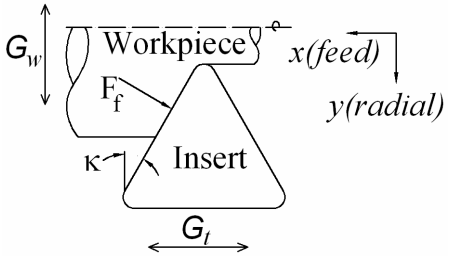

Figure 7.9: The transfer functions of the dynamic system and the resultant force.

Substituting equation (7.2) into equation (7.1) and considering the delay term τ, following is obtained, for the chatter limit and at the chatter frequency ω_c:

$$F(t)e^{-i\omega_c t} = \frac{K_f}{\cos\kappa} b_{\lim} \left(1 - e^{-i\omega_c \tau}\right) G_o(i\omega_c) F(t) e^{-i\omega_c t} \tag{7.3}$$

The stability problem reduces to an eigenvalue problem, where the eigenvalue Λ is defined as follows:

$$\Lambda = K_f b_{\lim} \left(1 - e^{-i\omega_c \tau}\right) \tag{7.4}$$

And the stability limit can be obtained analytically as follows [64]:

$$b_{\lim} = \frac{-\cos\kappa}{2K_f \,\mathrm{Re}[G_o]} \tag{7.5}$$

Equation (7.5) can be used to find the stability limit of the dynamic system. The absolute stability limit of the system can also be obtained by replacing Re[G_0] with the minimum magnitude of the real part of the oriented transfer function Re[G_0]$_{min}$ in equation (7.5).

7.5.2. Effects of the Inclination and Side Edge Cutting Angles

1DOTF model does not consider the effect of the inclination angle on the stability limit whereas the effect of side edge cutting angle can be modeled with 1DOTF stability

model. Therefore, it is important to represent the effect of both the inclination and the side edge cutting angles on the stability limit, and to compare with the multi dimensional stability model.

Table 7.7: Parameters used in the comparison simulations for the effect of inclination and side edge cutting angle.

Rake angle	0°
Insert nose radius	0 mm
Shear Stress	350 MPa
Shear Angle	32º
Friction Angle	29º
Natural frequency of the workpiece and tool	1000 Hz
Stiffness of the workpiece and tool – flexible	$3x10^7$N/m
Stiffness of the workpiece and tool – rigid	$30x10^7$N/m
Damping ratio	0.01

The parameters used in the comparison simulations are listed in Table 7.7. The cutting force coefficients K_f and K_r are calculated from the orthogonal data i.e. the shear angle, the friction angle and the shear stress by oblique transformation for each inclination angle [10]. The work material has been selected as AISI 1040 steel, and the corresponding database for the coefficients has been used. The transfer functions of the components are calculated from the modal parameters, i.e. natural frequency, damping coefficient, and the stiffness of the component, where representative values have been used in the simulations based on the measurements on these systems. Two different cases are considered in the following. In the first case the workpiece is more flexible than the tool whereas in the second case the tool is more flexible. The insert has straight edge, i.e. there is no insert nose radius in order to observe the effect of the cutting angles only. The absolute stability limit error defined in equation (7.6) is used to quantify the difference between the models:

$$\%error = \frac{\left| b_{abs-1DOTF} - b_{abs-MULTI} \right|}{b_{abs-MULTI}} \times 100 \qquad (7.6)$$

The results for different inclination and side edge cutting angles can be seen in Figure 7.10.a and Figure 7.10.b.

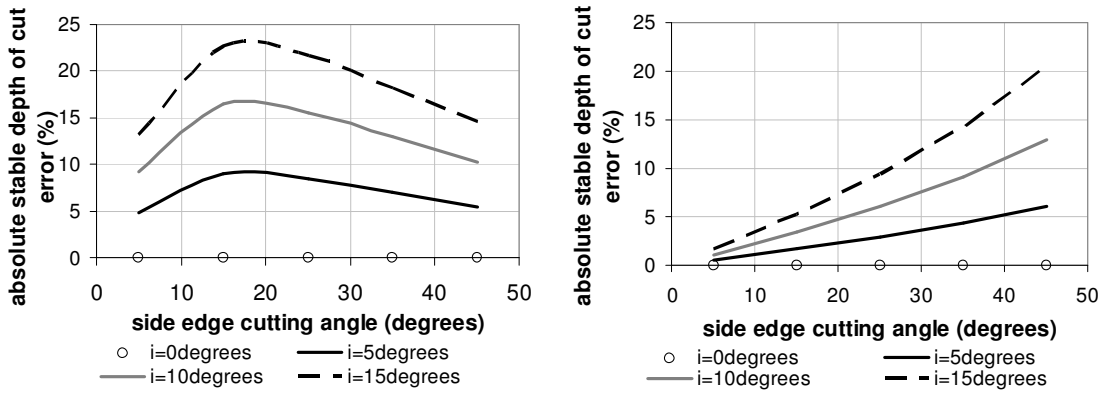

(a) (b)

Figure 7.10: Variation of absolute stability limit error between 1DOTF and MD stability models for (a) flexible workpiece and (b) flexible tool cases.

As can be seen from Figure 7.10.a and Figure 7.10.b, 1DOTF and Multi Dimensional stability models predict the same absolute stability values for different side edge cutting angles when there is no inclination angle. This is an interesting result since the 1DOTF stability model orients the total frequency response function into a one direction reducing the multi dimensional dynamics to one. This can be verified mathematically as follows:

For the 1DOTF model, the real part of the oriented transfer function can be written from Equation (7.2) as follows:

$$\mathrm{Re}[G_o(i\omega_c)] = \mathrm{Re}[G_t(i\omega_c)]\cos^2(\kappa) + \mathrm{Re}[G_w(i\omega_c)]\cos^2(1.5\pi + \kappa) \tag{7.7}$$

Since:

$$\cos^2(1.5\pi + \kappa) = \sin^2(\kappa) \tag{7.8}$$

Substituting Equations (7.7) and (7.8) into Equation (7.5) following is obtained for the stable depth of cut:

$$b_{\lim} = \frac{-\cos\kappa}{2K_f\left(\mathrm{Re}[G_t(i\omega_c)]\cos^2(\kappa) + \mathrm{Re}[G_w(i\omega_c)]\cos^2(1.5\pi + \kappa)\right)} \tag{7.9}$$

For the Multi Dimensional stability model, at orthogonal cutting conditions K_r becomes 0. Therefore equation (6.11) reduces to the following:

$$\begin{Bmatrix} F_x \\ F_y \end{Bmatrix} e^{i\omega_c t} = \Lambda \begin{bmatrix} -\cos\kappa & \sin\kappa \\ \sin\kappa & \cos\kappa \end{bmatrix} \begin{bmatrix} K_f \\ 0 \end{bmatrix} \begin{bmatrix} 1 & -\tan\kappa \end{bmatrix} \begin{bmatrix} G_t & 0 \\ 0 & G_w \end{bmatrix} \begin{Bmatrix} F_x \\ F_y \end{Bmatrix} e^{i\omega_c t} \tag{7.10}$$

The eigenvalue Λ can be calculated as follows (since the determinant of equation (7.10) must vanish in order to have a solution):

$$\Lambda = 1/\left[G_w\left(K_f \sin^2\kappa\cos\kappa\right) + G_t\left(K_f \cos^3\kappa\right)\right] \tag{7.11}$$

Also, the real and imaginary parts of the eigenvalue can be expressed as follows;

$$\begin{aligned} \mathrm{Re}[\Lambda] &= \frac{\cos\kappa}{Kf} \frac{\mathrm{Re}[G_w]\sin^2\kappa + \mathrm{Re}[G_t]\cos^2\kappa}{\left(\mathrm{Re}[G_w]\sin^2\kappa + \mathrm{Re}[G_t]\cos^2\kappa\right)^2 + \left(\mathrm{Im}[G_w]\sin^2\kappa + \mathrm{Im}[G_t]\cos^2\kappa\right)^2} \\ \mathrm{Im}[\Lambda] &= -\frac{\cos\kappa}{Kf} \frac{\mathrm{Im}[G_w]\sin^2\kappa + \mathrm{Im}[G_t]\cos^2\kappa}{\left(\mathrm{Re}[G_w]\sin^2\kappa + \mathrm{Re}[G_t]\cos^2\kappa\right)^2 + \left(\mathrm{Im}[G_w]\sin^2\kappa + \mathrm{Im}[G_t]\cos^2\kappa\right)^2} \end{aligned} \tag{7.12}$$

The ratio of the imaginary and the real parts, λ, can be obtained as follows:

$$\lambda = \frac{\mathrm{Im}[\Lambda]}{\mathrm{Re}[\Lambda]} = -\frac{\mathrm{Im}[G_w]\sin^2\kappa + \mathrm{Im}[G_t]\cos^2\kappa}{\mathrm{Re}[G_w]\sin^2\kappa + \mathrm{Re}[G_t]\cos^2\kappa} \tag{7.13}$$

Substituting equations (7.12) and (7.13) into equation (6.17), the stable depth of cut is obtained as follows:

$$b_{\lim} = -\frac{\cos\kappa}{2Kf} \frac{1}{\mathrm{Re}[G_w]\sin^2\kappa + \mathrm{Re}[G_t]\cos^2\kappa} \tag{7.14}$$

Comparing equations (7.9) and (7.14) it can be deduced that both of the stability models give the same result under the orthogonal cutting conditions with a side edge cutting angle, but without a nose radius.

This situation can also be explained by considering the physics of the process. Since the process is an orthogonal one due to the absence of inclination angle, the cutting force normal to the cutting edge is the only force that will affect the process dynamics. Therefore, the total force in the *x*-*y* plane (see Figure 7.9) is composed of the force in the chip direction, F_f, only. The multi-dimensional stability model handles this force by resolving it into *x* and *y* components, and obtains the dynamic displacement by multiplying with the FRF's in those directions. The 1DOTF stability model, on the other hand, orients the transfer functions in the uncut chip thickness direction, and obtains the dynamic displacements by multiplying with F_f. In orthogonal cases they both yield the same results. On the other hand, as the inclination angle increases, the difference between two models increases up to almost 25%. This is due to an additional force component; radial force F_r resulting from the inclination angle. Thus, 1DOTF stability

model cannot include the effect of the inclination angle yielding inaccurate stability predictions.

7.5.3. Effect of the Nose Radius

In this section, the effect of the insert nose radius on the stability limit predictions is presented. The comparison is done again using the absolute stability limit percentage error as described in equation 7.6, and the parameters that are used in the simulations are listed in Table 7.8. Two cases are considered where in the first case the workpiece is the most flexible component. 1DOTF stability model calculations for the nose radius can be done by using two possible approaches. First, the insert nose radius is completely neglected in order to see its overall effect on the stability in this section. Second, an approximation for the nose radius which is suitable for 1DOTF stability model is used for the round inserts and presented in the next section.

Table 7.8: Parameters used in the comparison simulations for the effect of the nose radius.

Rake angle	5°
Side edge cutting angle	30º
Shear Stress	350 MPa
Shear Angle	32º
Friction Angle	29º
Natural frequency of the workpiece and tool	1000 Hz
Stiffness of the workpiece and tool – flexible	$3x10^7$N/m
Stiffness of the workpiece and tool – rigid	$30x10^7$N/m
Damping ratio	0.01

The results of the simulations can be seen in Figure 7.11.a. and Figure 7.11.b. The error in the flexible workpiece case goes up to 95% for 1.8 mm insert nose radius whereas in the flexible tool case it becomes close to 40 %. This error is expected since the 1DOTF stability model does not include the insert nose radius effect in the formulation. In fact, the effect of the insert nose radius on the process dynamics is same as the side edge angle. In a dynamic turning process without an insert nose radius, or

side edge cutting angle, the dynamics of the system are only controlled by the dynamics in the uncut chip thickness direction which is *x* axis (see Figure 7.9). The effect of the dynamics in the *y* direction contributes to the dynamic system if there is a side edge cutting angle or an insert nose radius. An increase in insert nose radius or side edge cutting angle increases the effect of the dynamics in the *y* direction on the system stability. Since the 1DOTF stability model cannot handle this effect, unlike the multi dimensional stability model, as the insert nose radius increases the error between two methods increases, as well. It can also be deduced from Figure 7.11.a. that the effect of inclination angle on the error is very low compared to the effect of the insert nose radius.

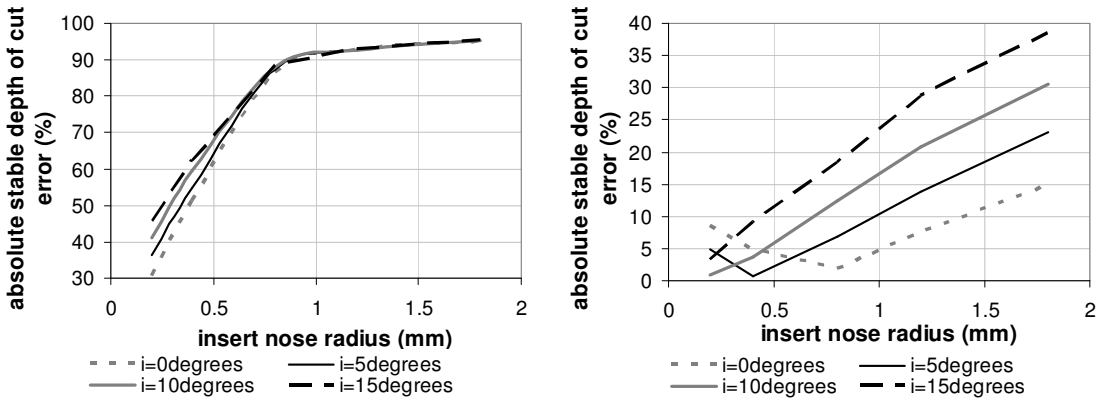

(a) (b)

Figure 7.11: Variation of absolute stability limit error between 1DOTF and MD stability models for (a) flexible workpiece and (b) flexible tool cases.

7.5.4. Round Insert Case

Although round inserts, especially made of ceramics, are commonly used in turning operations, they have not been considered in the chatter stability analyses up to now. Actually, a round insert is an extreme case of an insert with a nose radius which was discussed in the previous section. The 1DOTF stability model, which cannot model the stability of an insert nose radius accurately as it was shown in the previous section, cannot be used for round inserts, either. In this section, in order to demonstrate this with an extreme example, a round nose insert with 12 mm radius is used. However, a modification is done on the 1DOTF stability model in order to handle the nose radius and the round insert geometry in a more accurate manner. The curved edge is

represented by a line in the cutting zone which can also be used for the inserts with nose radius discussed in the previous section. This requires and iterative solution procedure as the stable depth, thus the in-cut part of the insert is not known in the beginning. The solution is initialized by dividing the nose region into equally heights and for each height a corresponding side edge cutting angle is determined (see Figure 7.12).

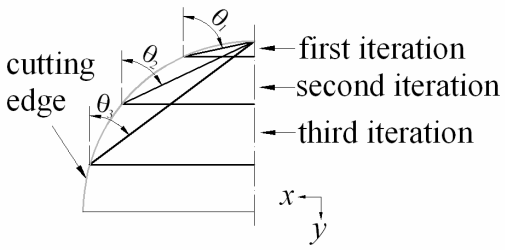

Figure 7.12: Schematic description of iteration based solution method for 1DOTF stability model.

It should be noted here that for each segment the stability limit is calculated by the method described in Chapter 7.5.1. The iteration starts with the first segment. If the calculated stability limit is found to be greater than the height of this segment, the iteration is continued with the next element. The final result is obtained when the calculated stability limit is smaller than the instantaneous segment's height. The simulation parameters used in the example case are listed in Table 7.9, and different stiffness values used for the tool and the workpiece are given in

Table 7.10. The comparisons are again done with respect to the absolute stability limit.

Table 7.9: Parameters used in the comparison simulations for the round insert case.

Rake angle	0°
Inclination angle	0º
Insert nose radius	12 mm
Shear Stress	350 MPa
Shear Angle	32º
Friction Angle	29º
Natural frequency of the workpiece and tool	1000 Hz
Damping ratio	0.01

Table 7.10: The stiffness value trend used in simulations.

$k_{tool}/k_{workpiece}$	k_t (N/mm)	k_w (N/mm)
20	$60x10^4$	$3x10^4$
10	$30x10^4$	$3x10^4$
0.3	$10x10^4$	$30x10^4$
0.16	$10x10^4$	$60x10^4$

The simulation results can be seen in Figure 7.13. On the left hand side of Figure 7.13, the workpiece is more flexible and on the right hand side the tool is more flexible. As it can be seen from the figure, the error between two models may be as large as 200% on the left hand side and 600% at the right hand side. Therefore, the improved version of the 1DOTF model which represents the insert nose radius by a line cannot predict these effects accurately, either.

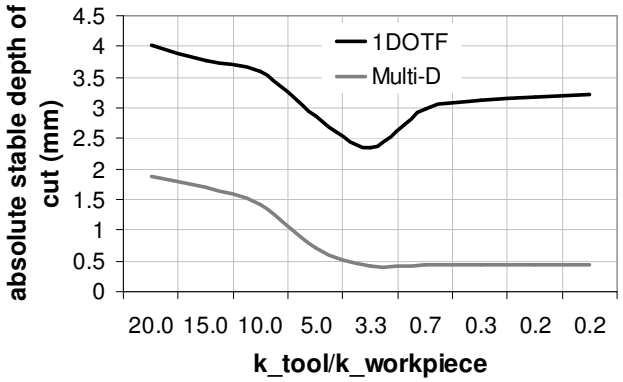

Figure 7.13: Comparison of absolute stable depth of cut predicted by the two analytical models for round nose inserts.

8. SUGGESTIONS FOR FURTHER RESEARCH

Following are the recommended studies for extending the capabilities of the models proposed in this study.

• In modeling of the edge forces in orthogonal cutting operations, the effect of the elastic behavior of the workpiece material is needed in modeling the flank contact length. The initial approach could be to modify the constitutive relationship in order to add the elastic deformation history to the equation.

• The proposed edge force model could be applied to the oblique cutting and turning operations.

• The proposed oblique cutting model could be applied to the milling operations for analytical simulations.

• A previously developed or newly proposed temperature model can be applied to all the proposed models in this thesis since all the necessary inputs for temperature distribution is already available.

• The proposed multi-dimensional stability model can be improved in order to simulate the dynamical behavior of the cutting process over the stability limit which can be useful for some milling application where there is no way of avoiding chatter vibrations.

• The friction behavior in oblique cutting can be investigated further.

• The effects of the process parameters on chatter stability limit can be investigated by using the proposed models.

9. DISCUSSIONS AND CONCLUSIONS

In this thesis, analytical models that truly represent the mechanical and dynamical behavior of cutting processes are proposed. The proposed models are original, and experimentally verified. Also fast and accurate way of identification of constitutive relationship parameters and sliding friction between the tool and the workpiece material is proposed. In addition, by the proposed analytical models, the material flow and friction behaviors during cutting is quantified and further investigated. Moreover, it is demonstrated that the analytical models can be used to simulate the industrial machining operations with fast solution times, and accurate predictions. Following is a list of the specific contributions:

• In this study a thermomechanical model of orthogonal cutting has been developed which accounts for the process of chip formation in the primary shear zone and includes the two-zone model of Zorev [3] to describe the contact at the tool-chip interface. This contact model comprises of a sticking zone near the tool tip. In this region the shear stress is identical to the shear flow stress of the work material. Further away of the tool tip, the chip is sliding along the rake face and the contact is governed by a Coulomb friction law.

• The thermo-viscoplastic response of the work material has been described by using a Johnson-Cook law whose parameters are directly identified from orthogonal tube cutting data. The parameters of the cutting model being identified and the predictive capabilities of the proposed approach have been tested by comparing the theoretical predictions of the cutting forces and of the shear angle with experimental data. Overall good agreement is observed

• The cutting model provides a theoretical relationship between the local friction coefficient μ of the Coulomb law and the global (or apparent) friction coefficient. This relationship depends on the thermomechanical characteristics of the work-material and on the cutting conditions. It is used to determine μ in terms of the apparent friction coefficient, which can be obtained from orthogonal cutting force measurements. By varying the cutting velocity, the dependence of μ with respect to the chip velocity was obtained.

• The total contact length and the sticking length predicted from the model were also compared with direct measurements using a microscope. All the predictions were found to be in good agreement with experiments for various cutting conditions.

• The proposed cutting model is believed to provide a significant improvement with respect to previous cutting models which neglected either the sliding contact (e.g. the Oxley [15] model) or the sticking contact (e.g. Molinari and Dudzinski [21]). It should be noted that the analytical nature of the model makes the computation very fast. In addition, the model calibration needs very limited number of tests compared to the mechanistic models commonly used in machining process modeling.

• The calibration ability of the model with a few tests makes it very practical and fast. Therefore, this approach is believed to provide a fast and accurate method of process simulation not only for research, but also for industrial applications.

• In this study, an investigation of the friction behavior in metal cutting operations is performed. It is demonstrated that the accurate cutting force predictions can only be obtained by considering the true nature of the contact on the rake face, i.e. by including both sticking and sliding zones in the analysis. It is shown analytically an experimentally that the total contact length increases by the feed rate and decreases by the cutting speed. The apparent friction coefficient strongly depends on the relative lengths of the sticking and sliding zones, and the sliding friction coefficient. It is shown that the apparent friction coefficient is always smaller than the sliding friction coefficient. The sticking contact length is strongly affected by the cutting speed. For some material-tool couples, it is observed that the contact is almost completely sliding

at high cutting speeds. For slow and moderate cutting speeds the contact involves both sticking and sliding zones. For most practical cutting conditions the sticking contact length is less than 15% of the total contact. Although the observations presented here were known, by the proposed models, these behaviors can now be quantified which enables further investigations. For instance, based on the cases considered in this study, it can be concluded that the total and sticking contact lengths are approximately 3-5 and 0-1.5 times the feed rate, respectively, both decreasing with the cutting speed.

• The sliding friction coefficients for various material-tool couples are identified which can be used for further studies. The main parameter that affects the sliding friction coefficient is observed to be the friction speed. However, in some cases the sliding friction coefficient is observed to have a slight dependency on the feed rate which affects the average pressure on the rake face.

• It is analytically and experimentally shown that the true representation of the friction behavior on the rake face should include the sliding and sticking friction regions. In addition, it is demonstrated that the friction model affects the accuracy of the feed force predictions more than the cutting force predictions.

• An analytical "initial approach" is proposed for modeling the third deformation zone. The hone radius effect on the primary and secondary shear zones is also taken into account in the proposed model. Comparing the model predictions with the experimental measurements, it can be stated that promising results are obtained.

• A process simulation model for turning processes is proposed. The proposed model handles the uncut chip thickness by diving it into many elements. However, the global behaviors such as global chip flow angle, chip velocity etc. are satisfied by energy equilibrium equations. The predictions and the verification experiments are found to be in good agreement.

• The proposed model is also applied to the 5 axis milling operations. The 5 axis milling tests are also conducted for the verification purposes, and over all good agreement is observed.

•A multi-dimensional analytical stability model for turning operations considering tool and workpiece dynamics is formulated. The proposed analytical model includes the important parameters in the turning geometry, i.e. the practical tool angles and nose radius. A matrix solution procedure is developed for stability limit with the proposed elemental model for the insert nose.

• The basic stability model is applied to the boring operations in order to model its stability. Another solution method is proposed for the boring operations which results in a 1D formulation with the same accuracy of predictions, but with a reduction of the computational time and the complexity of the solution procedure.

• Three cases of chatter experiments are conducted in order to verify the proposed analytical stability models. In general, the agreement between the analytical predictions and the experimental results are found to be satisfactory.

• It is demonstrated that the effect of insert nose radius on the stability limit is critical when the absolute stability limit of the system is comparable with the nose radius and this should be taken into account during predictions. Moreover, the effect of the insert nose radius on the stability limit for turning with a flexible tool, turning of a flexible workpiece and boring operations are different which is verified, and the observed behavior is as expected from the analytical predictions. It is found that using inserts with a bigger insert nose radius drastically reduces the stability limit in the turning of flexible workpiece and in boring operations whereas the opposite is true for the turning applications with a flexible tool.

• The 1DOTF and multi dimensional stability models are compared by several simulations. Since the turning process is 3D in nature, a true stability model should include the effect of the three cutting angles, i.e. rake, inclination and side edge cutting angles, the insert nose radius and the dynamics of the components in the cutting system in all directions. First of all, as it can be clearly seen from the analytical formulations, the rake angle only affects the cutting force coefficients, and does not have any other effect on the dynamic cutting system. It is also shown that both of the models can accurately predict the effect of the side edge cutting angle on the dynamic forces and the stability. Therefore, the stability limit of the orthogonal turning processes can be

predicted by 1DOTF stability model accurately. It is demonstrated that, one of the problems in the 1DOTF stability model is the absence of inclination angle effect. This is shown to yield up to 20% error in the stability limit prediction. This is mainly due to the radial force, Fr, arising as a result of the inclination angle. 1DOTF function model cannot include its effects on the stability accurately, as the radial force changes the resultant force direction. However, it can also be concluded that for small inclination angles, i.e. around 5º, 1DOTF stability model may predict the stability limit with a reasonable accuracy.

• Another important parameter in turning is the insert nose radius, which affects the stability limit drastically. Since the nose radius is not included in the 1DOTF model, the error between the two methods may go up to 95% as the insert nose radius increases. In the case of the round insert, a modified version of the 1DOTF stability model is used in order to represent the curved cutting edges more accurately. Even then the error between two methods is shown to be as high as 600% for round inserts. The inaccurate predictions of 1DOTF stability model are also demonstrated by the chatter experiments with different insert nose radii whereas reasonably accurate predictions are obtained with the multi-dimensional stability model. Thus, for turning processes with higher inclination angle and insert nose radius, 1DOTF stability model r<<esults are unreliable. In these cases, the multi-dimensional stability model should be used for accurate predictions.

REFERENCES

[1] Merchant, E., 1945, Mechanics of the Metal Cutting Process I. Orthogonal Cutting and a Type 2 Chip, Journal of Applied Physics, 16/5:267-275.

[2] Cumming, J. D., Kobayashi, S., and Thomsen, E. G., 1965, "A New Analysis of the Forces in Orthogonal Metal Cutting," ASME J. Eng. Ind., 87:480–486.

[3] Zorev, N. N., 1963, Inter-relationship between shear processes occurring along tool face and shear plane in metal cutting, International Research in Production Engineering, ASME, New York, 42-49.

[4] E.H. Lee and B.W. Shaffer, 1951, The Theory of plasticity applied to a problem of machining, Trans. ASME, J. Appl. Mech., 18:405–413.

[5] M. C. Shaw, N.H. Cook, and I. Finnie, 1953, The Shear-Angle Relationship in Metal Cutting", Transaction ASME, 75:273-283.

[6] Palmer, W.B., Oxley, P.L.B., 1959, Mechanics of Orthogonal Machining, Proc. Instn. Mech. Engrs., 173/24:623-638.

[7] Childs, T., 1980, Elastic Effects in Metal Cutting, Int. J. Mech. Sci., 22:457-466.

[8] Armarego, E.J.A. and Whitfield, R.C. 1985, Computer based modeling of popular machining operations for force and power predictions. Annals of the CIRP, 34: 65-69.

[9] Budak, E., Altintas, Y. and Armarego, E.J.A., 1996, Prediction of milling force coefficients from orthogonal cutting data. Trans. ASME J. of Man. Sci. and Eng., 118:216-224.

[10] Altintas, Y., 2000, Manufacturing Automation, Cambridge University Press.

[11] Lin, Z.C., Pan, W.C., 1995, Lo, S.P., A study of orthogonal cutting with tool flank wear and sticking behavior on the chip-tool interface, J. Mat. Proc. Tech., 52, 524-538.

[12] Lo, S.P., Lin, Y., 2002, An investigation of sticking behavior on the chip-tool interface using thermo-elastic-plastic finite element method, J Mat. Proc. Tech., 121:285-292.

[13] Yen, Y., Jain, A., Altan, T, 2004, A finite element analysis of orthogonal machining using different tool edge geometries, J. Mat. Proc. Tech., 146:72-81.

[14] Umbrello, D., Saoubi, R., Outeiro, J.C., 2007, The influence of Johnson–Cook material constants on finite element simulation of machining of AISI 316L steel, Int. J. Machine Tools & Manufacture, 27:462-470.

[15] Oxley, P.L.B., 1989, Mechanics of Machining, an Analytical Approach to Assessing Machinability, Ellis Horwood Limited, England.

[16] Fang, N, 2003, Slip-line modeling of machining with a rounded-edge tool – Part 1: new model and theory, J. Mechanics and Physics of Solids, 51:715-742.

[17] Fang, N., Jawahir, I.S., 2001, A new methodology for determining the stress state of the plastic region in machining with restricted contact tools, Int. J. Mech. Sci., 43: 1747-1770.

[18] Maity, K.P., Das, N.S., A Class of slipline field solutions for metal machining with sticking-slipping zone including elastic contact, Mater Design, doi:10.1016/j.matdes.2006.07.014.

[19] Kudo, H., 1965, Some new slip-line solutions for two-dimensional steady-state machining, Int. J. Mech. Sci. 7:43-55.

[20] Yellowley, I., 1987 A Simple Predictive Model of Orthogonal Metal Cutting, Int. J. Mach. Tools & Manufacture, 27/3:357-365.

[21] Molinari, A., and Dudzinski, D., 1992, Stationary shear bands in high speed machining, Comptes Rendus Acad. Sciences, 315, Série II, 399-405.

[22] Dudzinski, D., and Molinari, A., 1997, A Modeling Of Cutting For Viscoplastic Materials, Int. J. Mech. Sci, 39/4:369-389.

[23] Moufki, A., Molinari, A., and Dudzinski, D., 1998, Modelling of Orthogonal Cutting with a Temperature Dependent Friction Law, J. Mech. Phys. Solids, Vol. 46/10:2103-2138.

[24] Karpat, Y., Ozel, T., 2006, Predictive Analytical and thermal Modeling of Orthogonal Cutting Process – Part 1: Predictions of Tool Forces, Stresses, and Temperature Distributions, J. Manuf. Sci Eng., 128:435-444.

[25] Bailey, J.A., 1975, Friction in metal machining-mechanical aspects, Wear, 31: 243-275.

[26] Philippon, S., Sutter, G., Molinari, A., 2004, An experimental study of friction at high sliding velocities, Wear, 257:777-784.

[27] Tao, Z., Lovell, M.R., Yang, J.C., 2004, Evaluation of interfacial friction in material removal processes: the role of workpiece properties and contact geometry, Wear, 256:664-670.

[28] Fang, N., 2005, Tool-chip friction in machining with a large negative rake angle tool, Wear, 258:890-897.

[29] Childs, T.H.C., 2006, Friction modeling in metal cutting, Wear, 260:310-318.

[30] Ozel, T., 2006, The influence of friction models on finite element simulations of machining, Int. J. Machine Tools & Manufacture, 46:518-530.

[31] Kilic, D.S., Raman, S., 2006, Observations of the tool-chip boundary conditions in turning of aluminum alloys, Wear, doi:10.1016/j.wear.2006.08.019.

[32] Armarego, E.J.A., Brown, R.H., 1969, "The Machining of Metals", Prentice-Hall.

[33] Becze, C.E., Elbestawi,M.A., 2002, A Chip Formation Based Analytical Force Model for Oblique Cutting, International Journal of Machine Tools & Manufacture, 42, 529-538.

[34] Moufki, A., Devillez A., Dudzinski D., Molinari A., Thermomechanical Modeling of oblique cutting and experimental validation, International Journal of Machine Tools & Manufacture, 44, 971-989, 2004.

[35] Yen.Y, Jain.A, Altan Y., 2004, A finite element analysis of orthogonal machining using different tool edge geometries, Journal of Material Processing Technology, 146, 72-81.

[36] Özel, T., 2003, Modeling of hard part machining: effect of insert edge preparation in CBN cutting tools, Journal of Material Processing Technology, 141, 284-293.

[37] Fang N., Fang G., Theoretical and experimental investigations of finish machining with a rounded edge tool, Journal of Material Processing Technology, 191, 331-334.

[38] Karpat Y. ,Özel T., 2008, Analytical and Thermal Modeling of High-Speed Machining with Chamfered Tools, ASME Journal of Manufacturing Science and Engineering, 130, doi:10.1115/1.2783282.

[39] Fang N., Jawahir I.S., 2001, A new methodology for determining the stress state of the plastic region in machining with restricted contact tools, International Journal of Mechanical Sciences, 43, 1747-1770.

[40] Fang N., 2003, Slip-line modeling of machining with a rounded-edge tool – Part 1: new model and theory, Journal of the Mechanics and Physics of Solids, 51, 715-742.

[41] Manjunathaiah J., Endres W.J., 2000, A New Model and Analysis of Orthogonal Machining with an Edge-Radiused Tool, 122, 384-390.

[42] Colwell L.V., 1954, Predicting the angle of chip flow for single-point cutting tools, Transactions of ASME, 76, 199-204.

[43] Molinari A., Moufki A., 2005, A new thermomechanical model of cutting applied to turning operations Part I: Theory, International Journal of Machine Tools&Manufacture, 45, 166-180.

[44] Shatla, M.; Altan, T. Analytical Modeling of Drilling and Ball-end Milling. Journal of Materials Processing Technology. 2000, 98, 125-133.

[45] Fontaine, M.; Devillez, A.; Moufki, A.; Dudzinski, D. Predictive Force Model for Ball-end Milling and Experimental Validation with a Wavelike Form Machining Test. International Journal of Machine Tools and Manufacture. 2006, 46, 367-380.

[46] Gradisek, J.; Kalveram, M.; Weinert, K. Mechanistic Identification of Specific Force Coefficients for a General End Mill. International Journal of Machine Tools and Manufacture. 2004, 44, 401-414.

[47] Lazoglu, I. Sculpture Surface Machining: A Generalized Model of Ball-end Milling Force System. International Journal of Machine Tools and Manufacture. 2003, 43, 453-462.

[48] Ozturk, B.; Lazoglu, I.; Erdim, H.; Machining of Free-Form Surfaces. Part II: Calibration and Forces. International Journal of Machine Tools and Manufacture. 2006, 46, 736-746.

[49] Lee, P.; Altintas, Y. Prediction of Ball-end Milling Forces from Orthogonal Cutting Data, International Journal of Machine Tools and Manufacture. 1996, 36, 1059-1072.

[50] Engin, S.; Altintas, Y. Mechanics and Dynamics of General Milling Cutters Part 1: Helical End Mills. International Journal of Machine Tools and Manufacture. 2001, 41, 917-924.

[51] Yang, M.; Park, H. The Prediction of Cutting Force in Ball-end Milling. International Journal of Machine Tools and Manufacture. 1991, 31 (1), 45-54.

[52] Sadeghi, M. H.; Haghighat, H.; Elbestawi, M. A. A Solid Modeler Based Ball-end Milling Process Simulation. International Journal of Advanced Manufacturing Technology. 2003, 22, 775-785.

[53] Tai, C.; Fuh, K. The Prediction of Cutting Forces in the Ball-end Milling Process. Journal of Materials Processing Technology. 1995, 54, 286-301.

[54] Yucesan, G.; Altintas, Y. Prediction of Ball-end Milling Forces. Journal of Engineering for Industry. 1996, 118, 95-103.

[55] Kato, S., Yamaguchi, K., and Yamada, M., 1972, Stress Distribution at the Interface Between Tool and Chip in Machining, Journal of Eng. for Industry, 683-689.

[56] Barrow, G., Graham, T., Kurimoto, T., and Leong, F., 1982, Determination of Rake Face Stress Distribution in Orthogonal Machining, Int. J. Mach. Tool. Des. Res., 22/1: 75-85.

[57] Bariania P.F, Dal Negrob T., Bruschia S., 2004, Testing and Modelling of Material Response to Deformation in Bulk Metal Forming, CIRP Annals - ManufacturingTechnology, 53:2, 573-595.

[58] Ozlu, E., 2003, Dynamical Behavior of Materials Under High Strain Rate, Master Thesis, Istanbul Technical University, Istanbul, Turkey.

[59] Redford, D.D., 2000, Mechanical and Constitutive Behavior of Zr-2.5 Nb Pressure Tube Material at High Rates of Tensile Strain, Carleton University, Canada.

[60] Lee, W., Lin, C., 1998. Plastic deformation and fracture behaviour of Ti-6Al-4V alloy loaded with high strain rate under various temperatures, Materials Science and Engineering, A241, 48-59.

[61] Lee,W., Lin,C., 1998, High-temperature deformation behaviour of Ti6Al4V alloy evaluated by high strain-rate compression tests, Journal of Materials Processing Technology, 75, 127-136.

[62] Lee, W., Yeh, G., 1997. The plastic deformation behaviour of AISI 4340 alloy steel subjected to high temperature and high strain rate loading conditions, Journal of Materials Processing Technology, 71, 224-234.

[63] Noble , J.P., et.al., 1999. The use of Hopkinson bar to validate constitutive relations at high rates of strain, Journal of the Mechanics and Physics of Solids, 47, 1187-1206.

[64] Tlusty, J., Polacek, M., 1963, "The Stability of Machine Tools Against Self Excited Vibrations in Machining", Int. Research in Production Engineering, ASME, pp. 465-474.

[65] Tobias, S.A. and Fishwick, W., 1958, "The Chatter of Lathe Tools Under Orthogonal Cutting Conditions, Transactions of ASME, 80, pp. 1079-1088.

[66] Minis, I., and Yanushevsky, T., 1993, "A New Theoretical Approach for the prediction of the Machine Tool Chatter in Milling", ASME J. Eng. Incl., 115, pp. 1-8.

[67] Budak, E., and Altintas, Y., 1998, "Analytical Prediction of Chatter Stability in Milling-Part I: General Formulation"; "Part II: Application to Common Milling Systems", ASME J. Dyn. Sys. Meas. Control, 120, pp. 22–36.

[68] Marui, E., Ems, S., Kato, S., 1983, "Chatter Vibration of Lathe Tools. Part 1: General Characteristics of Chatter Vibration", Transactions of ASME, 105, pp. 100-106.

[69] Marui, E., Ems, S., Kato, S., 1983, "Chatter Vibration of Lathe Tools. Part 2: On the Mehanisms of Energy Supply", Transactions of ASME, 105, pp. 100-106.

[70] Kaneko, T., Sato, H., Tani, Y., 1984, O-hori, M., "Self-Excited Chatter and its Marks in Turning", Transactions of ASME, 222, pp. 106-228.

[71] Minis, I. E., Magrab, E. B., Pandelidis, I. O., 1990, "Improved Methods for the Prediction of Chatter in Turning Part 3: A Generalized Linear Theory", Transactions of ASME, 112, February, pp. 12-20.

[72] Rao, C. B., Shin, Y. C., 1999, "A Comprehensive Dynamic Cutting Force Model for Chatter Prediction in Turning", Int. J. of Mach. Tools&Manufacture, 39, pp. 1631-1654.

[73] Budak, E., Altintas, Y, 1998, "Analytical Prediction of Chatter Satbility in Milling – Part I: General Formulation", Transactions of the ASME , 120, March , pp. 22-30.

[74] Clancy, B.E., Shin, Y.C., 2002,"A Comprehensive Chatter Prediction Model for Face Turning Operation Including Tool Wear Effect", Int. J. of Mach. Tools&Manufacture, 42, pp. 1035-1044.

[75] Atabey, F., Lazoglu, I., Altintas, Y., 2003, "Mechanics of Boring Processes – Part I", Int. J. of Mach. Tools&Manufacture, 43, pp. 463-476.

[76] Lazoglu, I., Atabey, F., Altintas, Y., 2002, "Dynamic of Boring Processes: Part III – Time Domain", Int. J. of Mach. Tools&Manufacture, 42, pp. 1567-1576.

[77] Ozdoganlar, O. B., and Endres, W. J., 2000, "An Analytical Representation of Chip Area for Corner-Radiused Tools Under Depth-of-Cut and Feed Variations," ASME J. Mfg. Sci and Eng., 122, pp. 660-665.

[78] Ozdoganlar, O. B., and Endres, W. J., 1998, "An Analytical Stability Solution for the Turning Process with Depth-Direction Dynamics and Corner-Radiused Tooling," in Proc., ASME IMECE'98, Symp. on Advances in Modeling, Monitoring, and Control of Machining Systems, 64, pp. 511-518.

[79] Ozdoganlar, O. B., and Endres, W. J., 1997, "A Structured Fully-Analytical Approach to Multi-Degree-of-Freedom Time-Invariant Stability Analysis for Machining," in Proc., Symp. on Pred. Modeling in Metal Cutting as Means of Bridging Gap Between Theory and Practice, ASME IMECE'97, 6-2, pp. 153-160.

[80] Reddy, R. G., Ozdoganlar, O. B., Kapoor, S. G., DeVor, R. E., and Liu, X., 2002, "A Stability Solution for the Axial Contour-Turning Process," ASME J. Mfg. Sci. and Engg., 124, pp. 581-587.

[81] Chandiramani, N.K., Pothala, 2006, T., "Dynamics of 2-dof regenerative chatter during turning", Journal of Sound and Vibration, 290, pp. 448-464.

[82] Filice, L., Micari, F., Rizutti, S., and Umbrello, D., 2007, A critical analysis on the friction modeling in orthogonal machining, Int. J. Mach. Tools & Manufacture, 47:709-714.

[83] Buryta, D., Sowerby, R., and Yellowley, I., 1994, Stress Distributions on the Rake Face During Orthogonal Machining, Int. J. Mach. Tools & Manufacture, 34/5:721-739.

[84] Arsecularatne, J. A., 1997, On Tool-Chip Interface Stress Distributions, Ploughing Force and Size Effect in Machining, Int. J. Mach. Tools & Manufacture, 37/7: 885-899.

[85] Rabinowicz, E., 1995, Friction and Wear of Materials: Second Edition, Wiley-Interscience, New York, 102.

[86] Olsson, M., Soderberg, S., Jacobson, S., Hogmark, S., 1989, Simulaton of cutting tool wear by a modified pin-on-disc test, Int. J. Mach. Tools & Manufacture, 29/3:377-390.

[87] Maclain, B., Batzer, S.A., and Maldonado, G. I., 2002, A numeric investigation of the rake face stress distribution in orthogonal machining, J. Materials Proc. Tech., 123: 114-119.

[88] Özel, Tuğrul and Karpat, Yiğit , 2007, Identification of Constitutive Material Model Parameters for High-Strain Rate Metal Cutting Conditions Using Evolutionary Computational Algorithms, Materials and Manufacturing Processes, 22/5: 659 – 667.

[89] Ozlu, E., Budak, E., Molinari, A., 2007, Thermomechanical Modeling of Orthogonal Cutting Including the Effect of Stick-Slide Regions on the Rake Face, 10th CIRP International Workshop on Modeling of Machining Operations, Calabria, Italy, August.

[90] Jaspers, S.P.F.C., Dautzenberg, J.H., 2002, Material Behaviour in conditions similar to metal cutting: flow stress in the primary shear zone, Journal of Materials Processing Technology, 122: 322-330.

[91] Meyers, M.A., 1994, Dynamic Behavior of Materials, John Wiley&Sons.

[92] Merchant, M.E, 1944, Basic Mechanics of the Metal Cutting Process, Trans. ASME J. App. Mech., A:168-175.

[93] Molinari, A., Moufki, A., 2008, The Merchant's model of orthogonal cutting revisited: A new insight into the modeling of chip formation, International Journal of Mechanical Sciences, 50: 124-131.

[94] Ozturk, E., Budak, E., 2007, Modeling of 5-Axis Milling Process,, Machining Science and Technology, 11/3: 287 – 311.

[95] Bouzakis, K. D., Aichouh, P., Efstathiou, K.,2003, Determination of the chip geometry, cutting force and roughness in free form surfaces finishing milling, with ball end tools, Int. J. Mach. Tools and Manuf , 43/ 5: 499-514.

[96] Altintas, Y, Weck, M., 2004, "Chatter Stability of Metal Cutting and Grinding", Annals of the CIRP, 53(2), pp. 619-642.

[97] Cutpro© website: http://www.malinc.com

[98] Labview© website: http://www.ni.com

[99] Tlusty, J., 1978, "Analysis of the State of Research in Cutting Dynamics", CIRP Annals, 27(2), pp. 583-589.

[100] Lee, B.Y., Tarng, Y.S., Ma, S.C., 1995, "Modeling of The Process Damping Force in Chatter Vibrations", Int. J. of Mach. Tools&Manufacture, 35(7), pp. 951-962.